Engineering Journal

American Institute of Steel Construction

First Quarter 2018 Volume 55, No. 1

Framing Strategies for Enhanced Robustness in Steel Buildings

GUSTAVO CORTES, RACHEL CHICCHI and JUDY LIU

ABSTRACT

This paper describes the use of stiff-story framing to increase robustness in steel buildings subjected to column loss. Two case study buildings were designed; building A features a perimeter moment frame structure, while building B utilizes chevron-braced frames. The lateral-force-resisting systems (LFRSs) and stiff stories of these two prototype buildings were then modified to create different configurations in order to study which configurations were more robust. A linear static alternate path analysis was performed for each of the configurations, and the effectiveness in resisting column loss was determined. Based on the results from the analyses, two indices that quantify vulnerability and framing efficiency were developed that can be used by designers to evaluate framing alternatives. Cost and aesthetic considerations were explored as well. Evaluation of alternative configurations shows that tying the stiff story into the LFRS and supporting all exterior columns with the stiff-story framing will increase system robustness.

Keywords: stiff story, disproportionate collapse, robustness, column loss, alternate path analysis.

INTRODUCTION

Typical beam-column connections and composite floor deck details in steel gravity frames may not have sufficient robustness to support design loads in the event of a column loss (Main and Sadek, 2012; Francisco, 2014; Johnson et al., 2015; Weigand and Berman, 2014). These gravity frame connections are exclusively designed to resist shear forces; however, in the event of a column loss, very large axial loads develop in these connections, potentially inducing failure. This problem has motivated researchers to investigate "best practices" for reducing risk of disproportionate collapse, including using fully restrained connections for all beam-column connections and sizing all connections to resist beam axial tension (Ellingwood et al., 2007). Other researchers have created enhanced connections (Weigand, 2014; Liu, 2010) capable of resisting the large axial loads. In addition to research on ways to improve robustness locally, by increasing capacity of beam-column connections or in floor slab details, some have suggested a more global approach by means of alternative framing solutions. The use of a strong floor or stiff story, intended to provide distributed

stiffness, has been suggested as an effective means to avoid limit states such as connection fracture and, subsequently, disproportionate collapse in a column loss scenario (Carter, 2011).

This paper studies the use of lateral framing at strategic locations combined with stiff stories to create alternate load paths in the case of column loss. A stiff story is a stiff and strong system, usually a full story high, capable of redistributing loads from a lost column below. Figure 1 shows a three-story, three-bay frame with a stiff story at the roof. The stiff story limits beam-column connection deformations and transforms the compressive force in the columns above the missing column to a tension, or hanger, force. Thus, the gravity load is redistributed through the stiff story to the adjacent columns, as shown by the arrows in Figure 1.

This paper presents an investigation of the feasibility of using stiff-story solutions integrated with typical lateral-force-resisting systems (LFRSs) to increase robustness in steel buildings. The use of stiff stories is not a novel concept because it has been used in industry in the past. For instance, Weidlinger Associates renovated an existing office building through use of hangers and ring beams at the roof to support columns below in the event of a column loss scenario (Naderi et al., 2015). However, this paper will explore various configurations and different measures for identifying effective framing strategies that can be utilized by the designer. The emphasis of the paper is exterior column loss, and therefore, stiff stories are not employed at interior gravity frames. The paper begins with a discussion of the case study buildings and the corresponding configurations derived from these buildings. A brief summary of the alternate path method used to analyze the buildings is then presented, followed by the analysis results. These results were used to develop

Gustavo Cortés, Senior Infrastructure Adviser, Medair, Ecublens, Switzerland. Email: gustavo.cortes@medair.org (corresponding)

Rachel Chicchi, Ph.D. candidate, Lyles School of Civil Engineering, Purdue University, West Lafayette, IN. Email: rachel.chicchi@uc.edu

Judy Liu, Professor, School of Civil and Construction Engineering, Oregon State University, Corvallis, OR. Email: judy.liu@oregonstate.edu

indices that quantify the vulnerability, robustness and efficiency of these configurations.

CASE STUDY BUILDINGS

Three categories of stiff-story systems in existing buildings were studied: cantilever/hanging perimeter, large central span, and cantilever truss, as shown schematically in Figure 2. These buildings rely on stiff stories above to distribute gravity loads due to fewer gravity columns at the first floor. This concept inspired the two stiff-story buildings designed for this case study, referred to as building A and building B, which incorporate both traditional and stiff-story framing.

The American Zinc building in St. Louis, Missouri, influenced the design of case study building A. American Zinc features an exterior Vierendeel truss system designed to transfer forces due to a large center span, similar to Figure 2b. For building A, this center span was eliminated to create a more traditionally framed steel building by incorporating additional columns at the ground level; however, the geometry and dimensions of the Vierendeel truss were replicated in building A to create stiff stories. The case study

structure is a four-story office building. All perimeter framing is moment connected. A typical floor plan and exterior elevations are shown in Figures 3, 4 and 5, with triangles representing moment connections.

The second building studied, known as building B, was inspired by the Lamar Construction Corporate Headquarters, located in Hudsonville, Michigan, which features a large cantilever and Pratt truss system similar to Figure 2c. Again, the large span was removed by adding columns at each column line; however, the stiff-story truss of the Lamar Construction Corporate Headquarters building was incorporated into the design of building B. This case study building is a four-story office building with perimeter chevron-braced frames. Refer to Figures 6, 7 and 8 for the building layout and member sizes.

Each building was designed to comply with ASCE 7-10 and the AISC *Specification,* based on the locations and loads of the building for which it was inspired (ASCE, 2010; AISC, 2010). The dead loads for buildings A and B are 61 and 75 psf, respectively. Building A was conservatively designed for 100-psf live load due to the open layout. For building B, an 80-psf live load was applied per the original
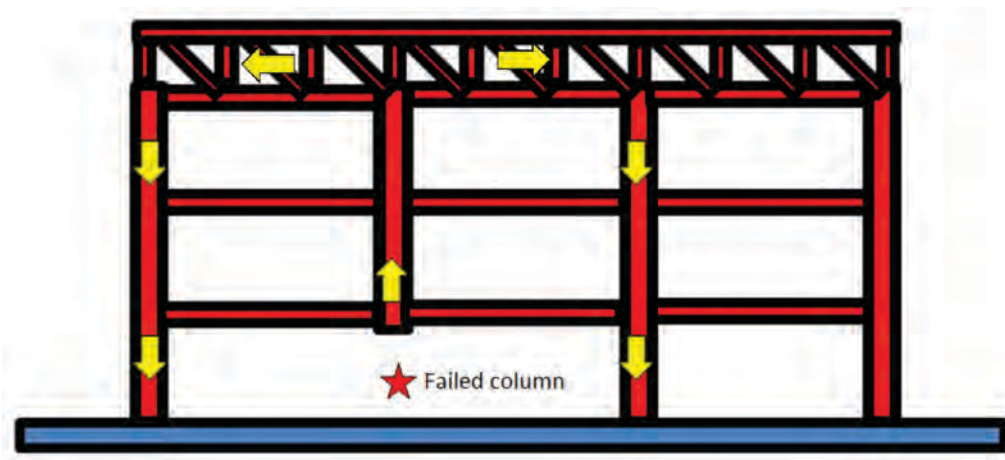
Fig. 1. Column loss in a building with a stiff story.
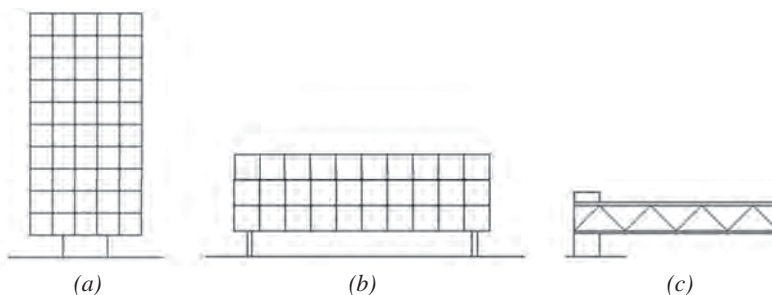
Fig. 2. Structural system: (a) cantilever/hanging perimeter; (b) large center span; (c) cantilever.
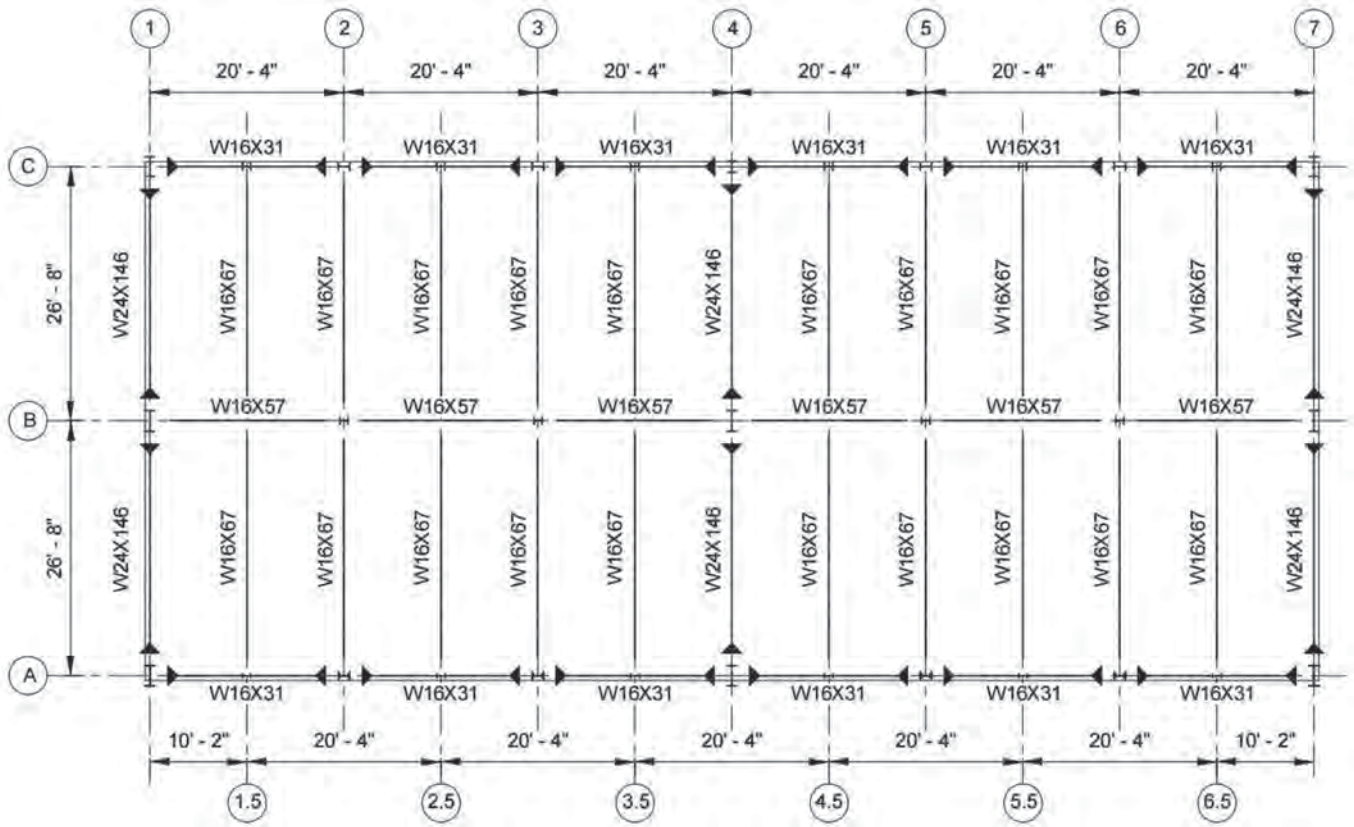
Fig. 3. Plan view (level 2) of building A.
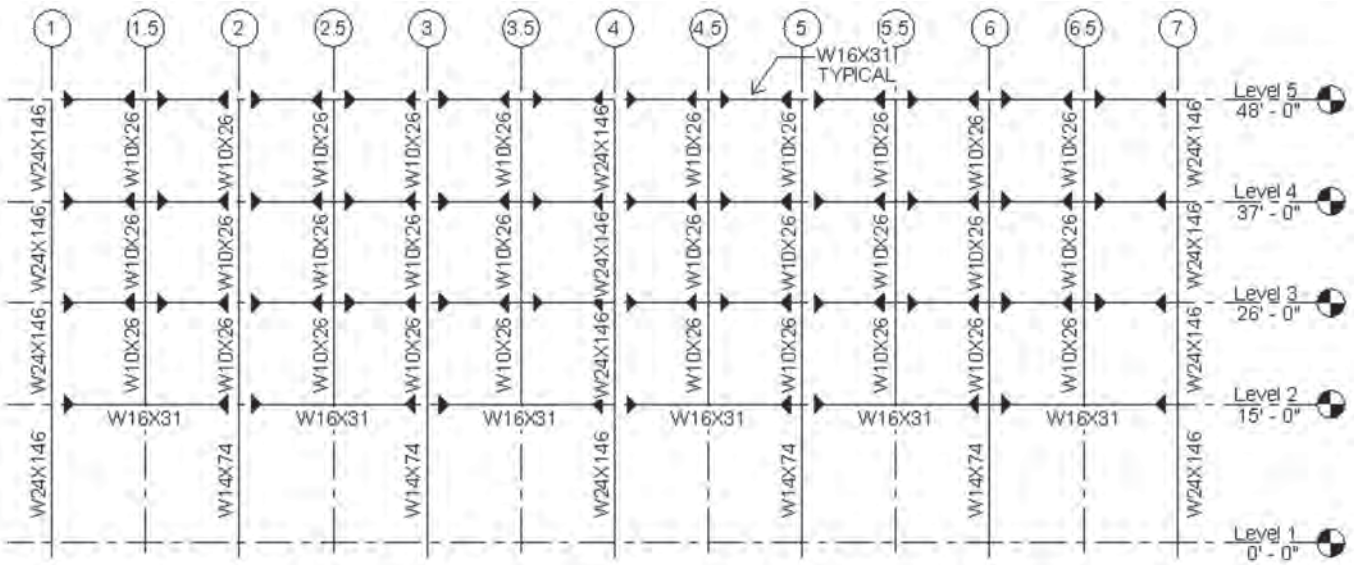
Fig 4. Elevation view (gridline A) of building A.
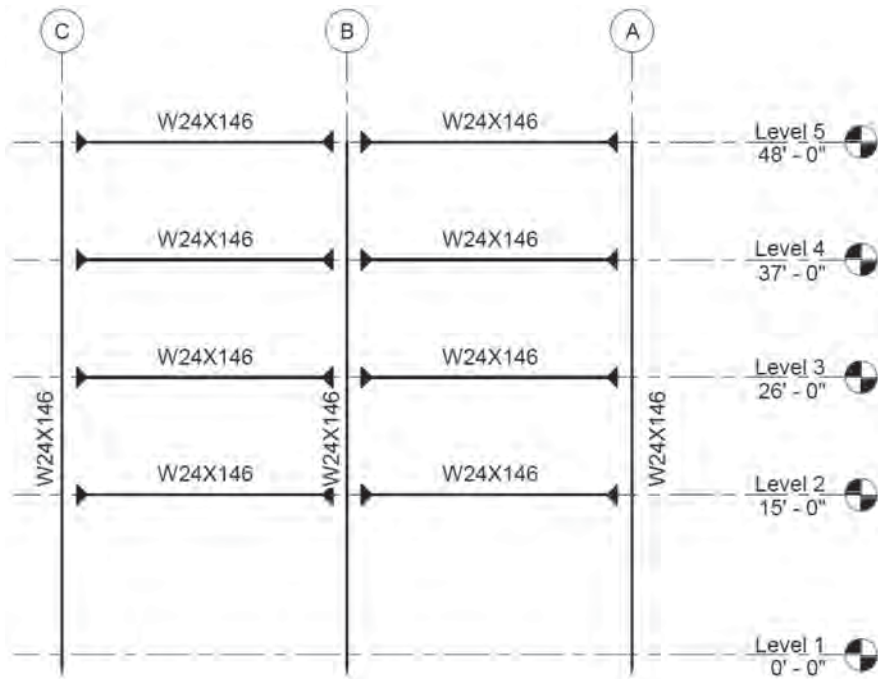
Fig. 5. Elevation view (gridline 1) of building A.
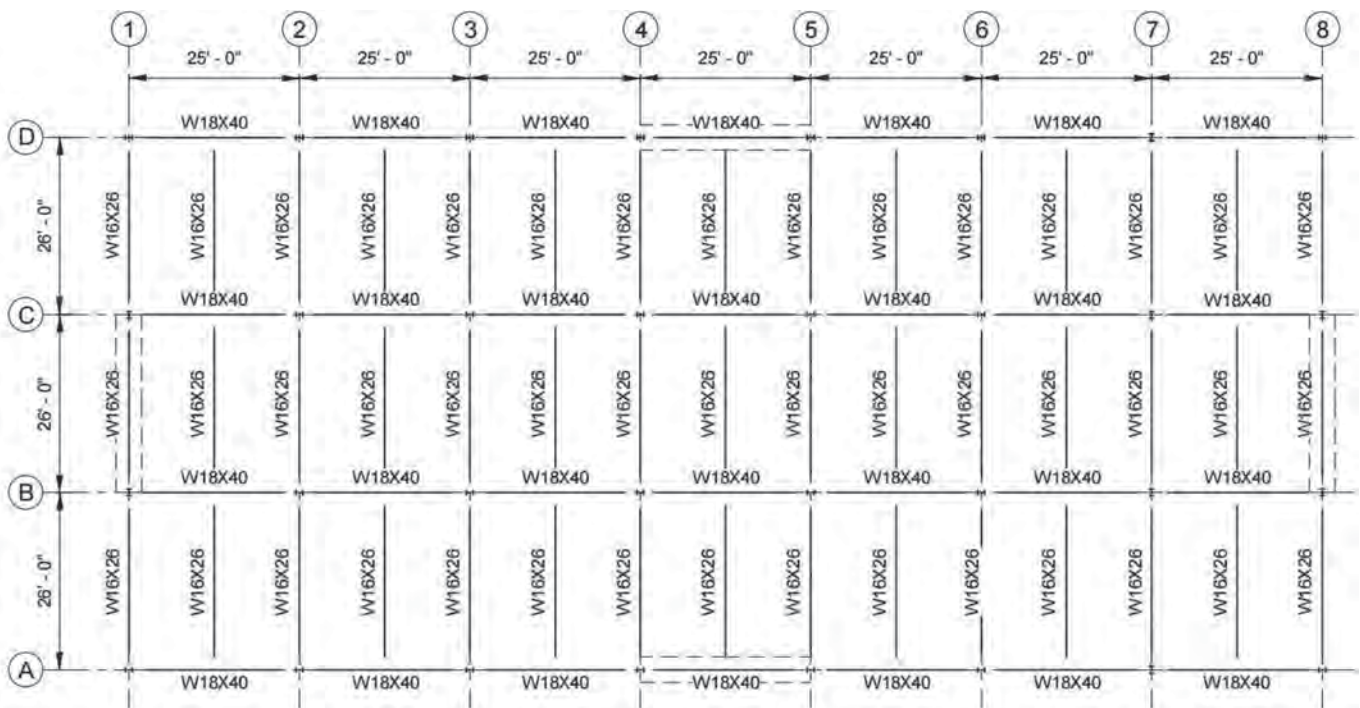
Fig. 6. Plan view (level 2) of building B (dotted lines indicate braced frames).
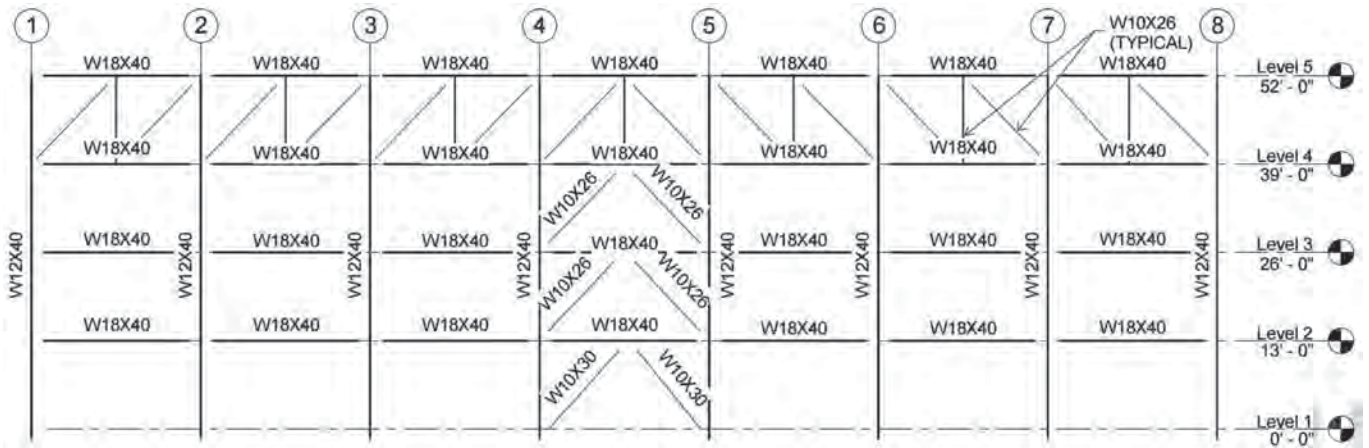
Fig. 7. Elevation view (gridline A) of building B.
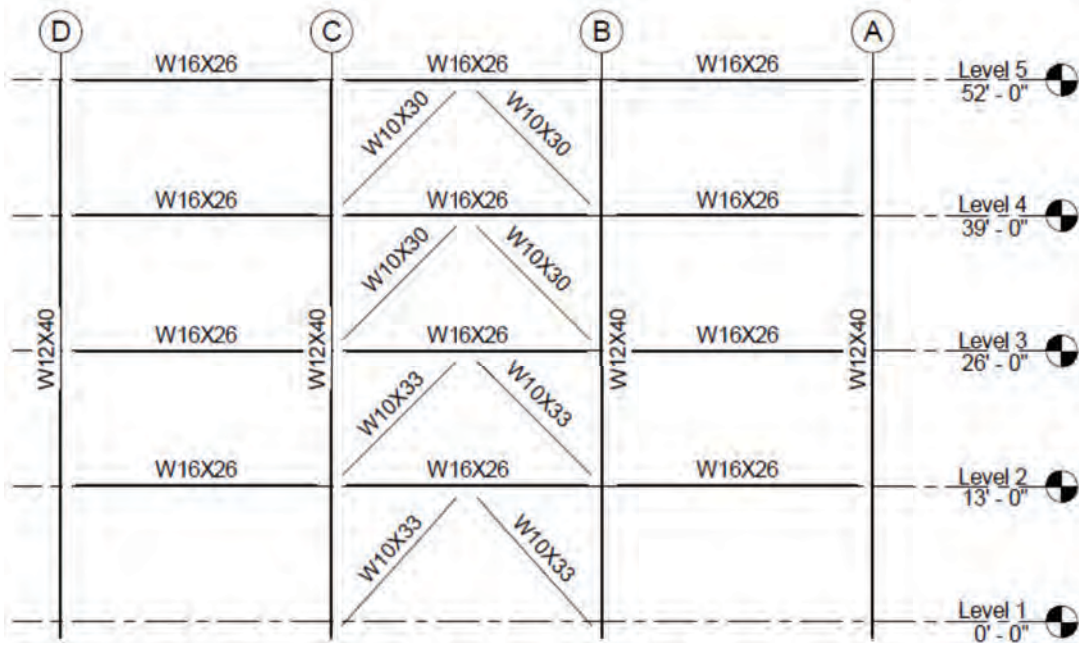
Fig. 8. Elevation view (gridline 1) of building B.

building design. Both buildings were designed as Seismic Design Category C structures. Building A was designed with ordinary steel moment frames, while building B incorporated an ordinary concentrically braced frame system. More details about each structure, as well as the existing buildings used for inspiration, can be found in the AISC report (Cortes and Liu, 2015).

Both buildings employ lateral-force-resisting systems along the perimeter of the buildings; hence, only exterior column loss scenarios were evaluated. For the purposes of this study, it was assumed that the threat to column loss exists at exterior columns only due to controlled public access and no underground parking. In the future, the proposed methodology can be applied to interior column loss scenarios as well.

BUILDING CONFIGURATIONS

Alternative building configurations for both case study buildings were developed in order to evaluate the effectiveness of different framing strategies on the robustness of a steel structure. The configurations for each building have the same overall geometry and differ only in the locations of LFRSs and the presence and locations of the stiff stories. Each configuration is code compliant for gravity and lateral loads but was not designed for the column-loss scenario.

While many different potential configurations could have been developed, the configurations used were chosen because they vary both LFRS locations and stiff-story locations, as well as the level of robustness. Additional framing configurations can be found in Cortes and Liu (2015) and Cortes et al. (2015).

Building A Configurations

Four additional configurations for building A were analyzed to explore the influence of stiff stories and integration of the LFRS on system robustness (Figure 9). In the development of the alternative configurations, some were developed using the stiff-story concept, while others were intentionally designed to rely on the LFRS for system robustness in the event of column loss. The intention was to consider the relative cost effectiveness of the different framing configurations. In Figure 9, thick lines designate moment frame components, and fire symbols represent locations where column removal was evaluated. Using the alternate path procedure, which will be explained in the next section, one column was removed at a time in order to analyze each of the configurations. Configuration A0 is the initial configuration with full Vierendeel trusses in the long direction of the building and moment frames in the short direction (column lines 1, 4 and 7 in Figure 9). A1 does not have a stiff-story element; however, each external column is part of a moment frame, with column 4 contributing to a moment frame in the transverse direction. For building A2, a braced frame was employed in the transverse direction (at gridlines 1 and 7) to provide another alternative should the engineer wish to avoid having corner columns at the upper story with moment connections in both orthogonal directions. Configurations A2 and A3 include stiff stories of varying length. Configuration A4 employs traditional moment frames, with some external gravity frames but no stiff story.

Building B Configurations

Six additional configurations were analyzed for building B, as shown in Figure 10. B0 is the original base configuration
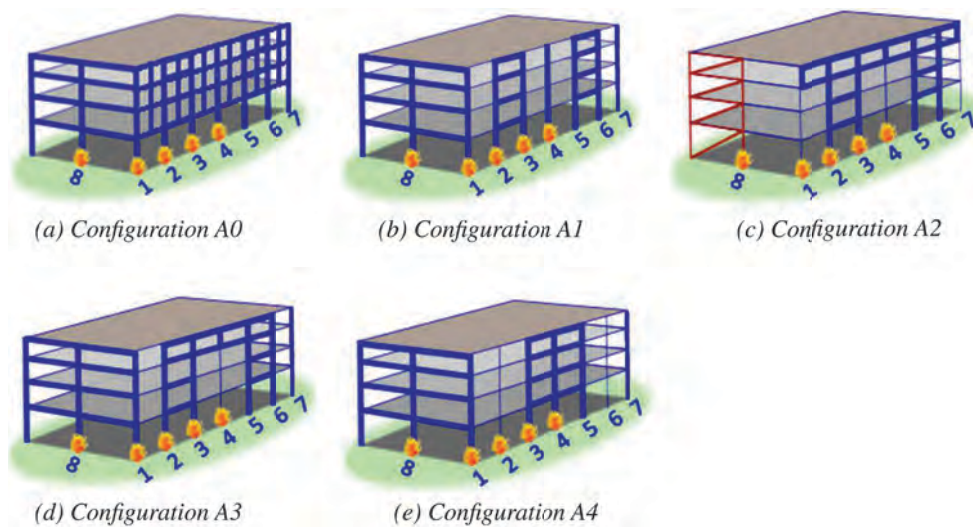
Fig. 9. Building A configurations (thick lines represent moment frame components).

inspired by the Lamar Headquarters. As mentioned previously, the other configurations are variations of the base building, with changes in braced frame locations and variations of framing with and without a stiff story. Again, in order to study the relative cost effectiveness of different framing strategies, some configurations were designed to rely on the LFRS as much as possible for system robustness in the event of column loss. For B1 and B4, the stiff story has been removed, creating a more traditional building. Many of the columns in these configurations are not adjacent to braced frames or supported by a stiff story, making B1 and B4 more vulnerable than other configurations. Configurations B2 and B5 are similar to B1 and B4, respectively, with a stiff story added in the longitudinal direction of the building. B3 and B6 examine the effect of extending a stiff story around the entire perimeter of the building. Chevron braces were selected as the stiff-story elements in lieu of diagonal braces in order to extrapolate the framing of the braced frames in the LFRS, and B1 replaced B0 as the base building for comparisons of robustness.

ALTERNATE PATH ANALYSIS

The Alternate Path (AP) Linear Static Procedure (LSP) provided in UFC 4-023-03, *Design of Buildings to Resist Progressive Collapse* (DoD, 2009), was implemented in order to study each of the configurations presented in the previous sections. ASCE 41-06, *Seismic Rehabilitation of Existing Buildings* (ASCE, 2007), was also used extensively because the UFC guidelines reference ASCE 41-06 often. UFC requires that at least one column near the middle of the structure on the long side, one column near the middle

of the structure on the short side, and one corner column be removed. In this study, however, every unique exterior column removal scenario was conducted for each configuration. Because the buildings are symmetrical, only one of each type of uniquely supported column was selected for removal (identified by the fire symbols in Figures 9 and 10). Columns not supported by moment connections or braces were assumed to be incapable of meeting acceptance criteria in column loss scenarios because the beam-column connections are modeled as pinned connections and do not have rotational resistance. Column removal scenarios at each of these locations are classified as a collapse mechanism.

The structural analysis software, SAP 2000 (CSI, 2014), was used to analyze each column removal scenario through a staged construction process. For each building configuration, two models were created: one for deformation-controlled actions and the other for force-controlled actions. The deformation-controlled model is used when verifying ductile limit states (e.g., column tension, beam flexure), while the force-controlled model is used for verifying brittle limit states (e.g., column compression, beam shear). All members were analyzed according to the AISC *Specification* (AISC, 2010) and using the load combination shown in Equation 1. The load factor Ω_L is 1.0 for areas away from the removed column in both force-controlled and deformation-controlled actions. For areas immediately adjacent to the removed elements, Ω_L is a function of the *m*-factors for deformation-controlled actions and 2.0 for force-controlled actions. In Equation 1, *D*, *L* and *S* are the dead, live and snow loads, respectively.

$$G_L = \Omega_L \left[1.2D + (0.5L \text{ or } 0.2S) \right] \qquad (1)$$

(a) Configuration B0 *(b) Configuration B1* *(c) Configuration B2* *(d) Configuration B3*

(e) Configuration B4 *(f) Configuration B5* *(g) Configuration B6*
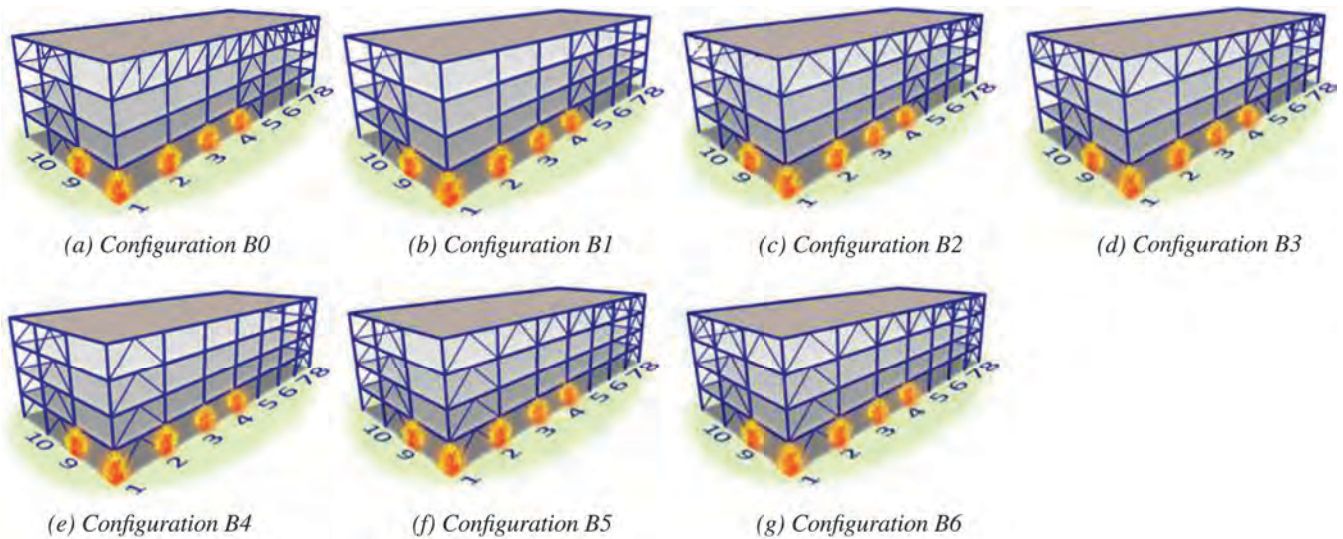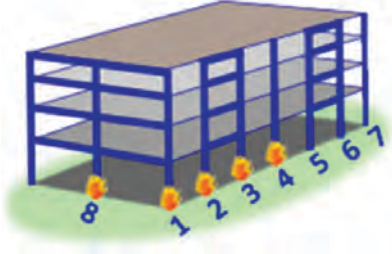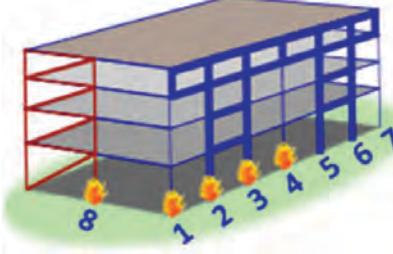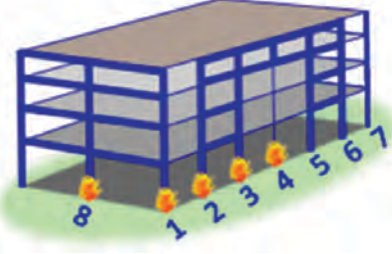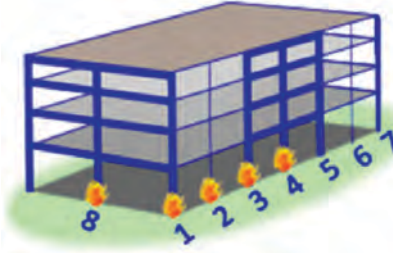
Fig. 10. Building B configurations.

Table 1. Building A Configuration Results Summary

A1 CM = 0 RE = 0	A2 CM = 0 RE = 10
A3 CM = 0 RE = 0	A4 CM = 4 RE = 0

CM = collapse mechanism
RE = elements requiring redesign

Here, *m*-factors are numerical values that are part of the acceptance criteria for structural members and elements. These were derived for seismic loads and are included in ASCE 41 for linear procedures. ASCE 41 and the UFC both make use of *m*-factors in determining load increases and for the final evaluation of member suitability.

For each scenario, the first-story column (and adjoining brace, if applicable) was removed and loads were applied. Results from the column removals of each model were then analyzed to determine which specific frame members are inadequate according to UFC and ASCE 41 criteria. Figure 11 shows results of configuration A0 analyses. The "x" indicates which columns were removed. The circled members are those that did not meet criteria and required redesign. In this scenario, all of the inadequate elements are Vierendeel truss columns adjacent to a missing column, which are carrying a portion of the load originally carried by the missing column. These results are logical because the building was designed without consideration of column removal, and thus, the adjacent columns were not designed for the redistributed loads.

Building A Results

The preceding process was followed to analyze every configuration. The results for building A configurations are summarized in Table 1, which shows the configuration name, number of collapse mechanisms (CMs) resulting from column removals, and the number of elements requiring redesign (RE). The column removal analysis results are based on 16 exterior columns.

Although a stiff story was not directly employed in A1, strategic location of the moment frames allowed the elimination of collapse mechanisms under the elastic analysis. This strategy was sufficient to eliminate column loss risk. For configuration A2, removal of column 8 (and the adjoining brace) caused building torsion, which resulted in five members requiring redesign; therefore, removal of the same column on the opposite face of the building was assumed to also require five members to be redesigned. This building torsion is due to a rigid-body rotation of the braced frame caused by the vertical displacement at the missing column (and brace) location. No redesign was required when a
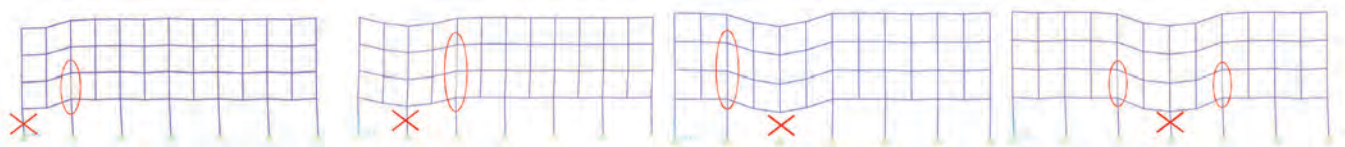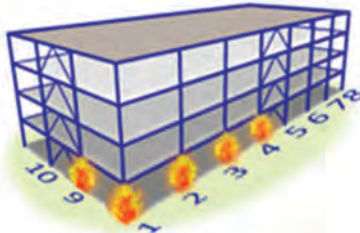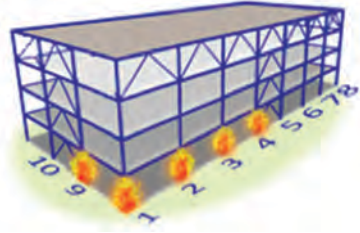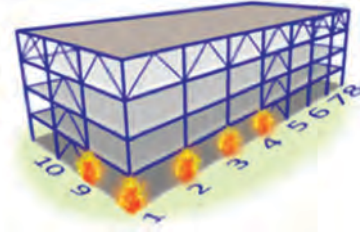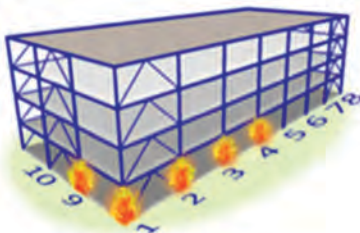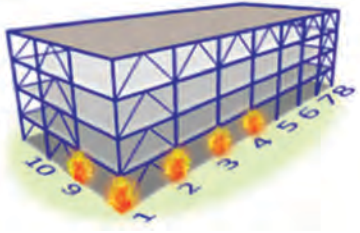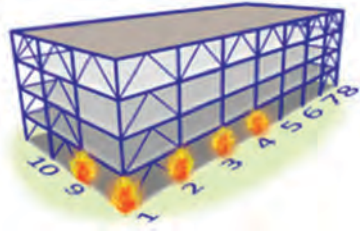
Fig. 11. Column removal deflected shapes for configuration A0. Unsatisfactory members identified with oval.

Table 2. Building B Configuration Results Summary		
B1 CM = 12 RE = 68	B2 CM = 0 RE = 36	B3 CM = 0 RE = 4
B4 CM = 8 RE = 48	B5 CM = 0 RE = 28	B6 CM = 0 RE = 8
CM = collapse mechanism RE = elements requiring redesign		

column under the stiff story (columns 1–7) was removed. Through incorporation of a stiff story and strategic location of LFRSs, all members in configuration A3 passed acceptance criteria. For configuration A4, collapse mechanisms were assumed at columns 2 and 6. The vulnerability on these columns could be mitigated by adding a stiff story in the spans between columns 2–3 and 5–6.

The analysis of this building showed that stiff stories can effectively redistribute loads in column loss scenarios. This was evidenced in configurations A2 and A3. It is believed that because the moment frames were designed to limit interstory drifts, the members had excess load-carrying capacity, allowing the LRFS and stiff-story components to carry the distributed loads without requiring redesign.

Building B Results

Building B configurations were also analyzed for column loss and the results are summarized in Table 2. The number of collapse mechanisms and members requiring redesign is based on the total number of exterior columns in the building (20).

Configuration B1 was used as the baseline and does not have a stiff story. It has 12 columns that, if removed, would result in a CM, making it very vulnerable and the least robust of all configurations. The braced frame configurations in the short direction of the building lacked redundancy, causing many members to require redesign when one of the braced

frame columns was removed. For case B1, 60 of the 68 elements requiring redesign were due to removal of columns 9 and 10, as well as the other two identical columns due to symmetry. This is due to the previously mentioned building torsion that results from removal of the brace causing rigid-body rotation. Configuration B2 is similar to configuration B1, with a stiff story added in the longitudinal direction of the building. This stiff story eliminated the collapse mechanisms and reduced the number of members requiring redesign from 68 to 36. Once again, most of the members requiring redesign were due to the removal of column 9 (and identical columns) causing building torsion. Configuration B3 incorporates stiff-story elements in the short direction of the building, completing the stiff story around the full perimeter of the building. This minimized building torsion under column removal 9 (and identical columns) and resulted in only four members requiring redesign. B4 does not incorporate a stiff story and has eight vulnerable columns, resulting in CMs under static analysis, and 48 members requiring redesign. Forty-four of these member redesigns are due to building torsion effects caused by the loss of column 9 (and identical columns). Configuration B5 has no CMs; however, as for previous configurations, removing column 9 (and identical columns) caused a building torsion that was responsible for the 28 members requiring redesign. It should be noted that in this configuration, no elements required redesign when a column under the stiff story (columns 1–8) was removed. Configuration B6 is the same as B5, but with

a stiff story in the transverse direction as well. This reduced the number of elements requiring redesign. This reduction is mainly due to the additional stiffness provided by the stiff story in the short direction, which helped reduce the building torsion.

The analysis results from the configurations that featured stiff stories show that the stiff-story concept can, when adequately designed, redistribute loads throughout the structure. Removal of a column supported by a stiff story often did not require member redesign for that specific column removal scenario. Some column removals resulted in members that did not meet acceptance criteria but could easily be remedied with a slightly larger section size. The most substantial improvements in performance (i.e., reduction in members requiring redesign) were achieved by continuing the stiff story around the perimeter of the building, as shown by configurations B3 and B6. While RE does not necessarily result in disproportionate collapse, it is an indication of the level of effort required beyond conventional analysis and design for gravity and lateral loads to achieve system robustness.

SUPPORT AND BRACING FACTORS

In order to quantify the vulnerability, robustness and efficiency of each of these configurations, a support factor, S_F, and bracing factor, B_F, were developed. These two factors reflect the scope of the parametric study, which was based on relatively simple building configurations designed for typical gravity and lateral loads but not for column loss. The support factor provides some indication of the relative robustness of the system, while the bracing factor provides an indication of the relative effectiveness of a particular framing configuration in resisting collapse. These factors can be used by designers to evaluate the most efficient configuration for their own building designs.

The support factor is calculated as the percentage of exterior columns that are supported by a braced frame, moment frame, or stiff story. For these case study buildings, each column from ground to roof would count as one column. For a taller building, which might have stiff stories at intervals over its height, this accounting of columns may need to be revised. The stiff stories are effective at preventing CMs of columns they support. For building B1, the support factor, S_F, would then be based on eight columns supported out of 20 exterior columns, resulting in 40%. For configuration B4, the factor would be based on 12 columns supported (or 60%). As shown in Figure 12, there is a direct correlation of support factor, S_F, to number of collapse mechanisms (CM). CM and S_F are essentially complements of one another. For example, 60% of columns supported translates into 40% of columns collapsing, while 100% of columns supported results in no collapse mechanisms.

Relative efficiency, or effectiveness, of different framing solutions would vary by designer. However, if following the same design approach used in this study (i.e., designing initially for gravity and lateral loads without consideration for column loss), and if defining higher effectiveness by lower
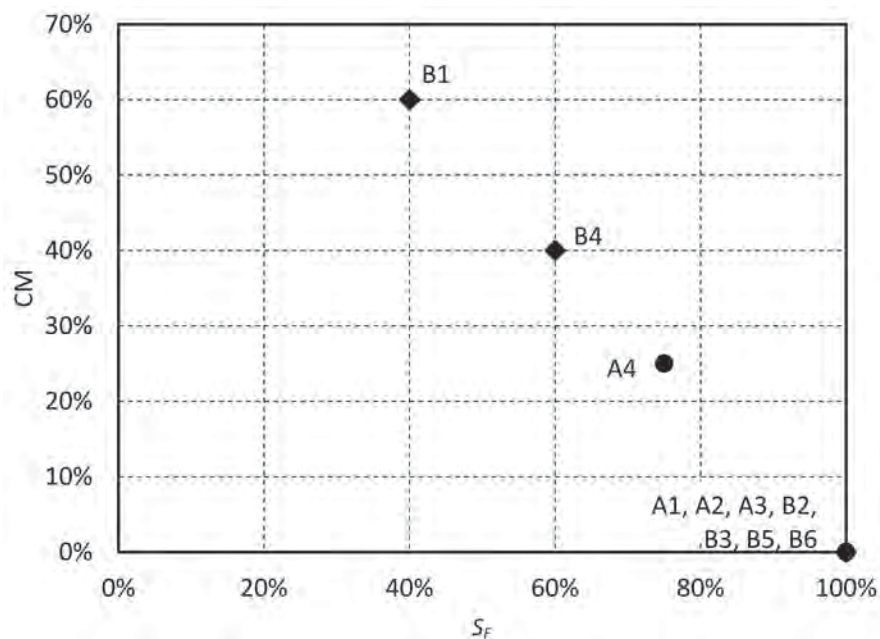
Fig. 12. Support factor, S_F, versus collapse mechanisms, CM, for the building configurations.

numbers of members requiring redesign, then the bracing factor, B_F, provides some indication of relative effectiveness of a given configuration. B_F represents the percentage of exterior bays within the story that are laterally braced or moment connected. A braced bay was defined as a one-story, one-bay frame with diagonal braces or moment connections. The bracing factor, B_F, shown in Equation 2 as a percentage, was established as a simple way of representing the relative efficiency of the combined stiff story and lateral bracing system; n_{BB} and n_B are the number of braced bays and the total number of exterior bays on the structure (80 for building B).

$$B_F = \frac{n_{BB}}{n_B}(100\%) \qquad (2)$$

The relative effectiveness of different configurations can be seen in a plot of the bracing factor, B_F, versus the number of elements requiring redesign, RE (Figure 13). A higher B_F generally means a lower number of members requiring redesign. For most of the configurations studied, a higher bracing factor is preferred.

For buildings with braced frames, some effectiveness can be gained by running the stiff story around the entire perimeter of the building, as in configurations B3 and B6. This benefit can be seen in Figure 13, where the two configurations for building B with the lowest RE values are B3 and B6. Of these two configurations, B3 is the best option because it required fewer braced bays (lower B_F) to achieve a lower RE.

For building A, B_F was at least 50% for all configurations. This large percentage, compared with building B, is partially due to the extra moment frames required to satisfy interstory drift limits.

The evaluation of the alternative configurations for the case study buildings demonstrates that essentially any stiff story solution that ties in with the LFRS and supports all columns will be more robust than traditional framing. This can be seen in a comparison of the support factor, S_F, and the number of collapse mechanisms, CMs.

IMPLEMENTATION AND CONSIDERATIONS OF FRAMING STRATEGIES

The support factor and bracing factor can be used to evaluate the effectiveness of framing strategies. Higher percentages for these factors imply increased robustness. However, it is not the intent of this paper that designers should design excessively robust structures and always incorporate stiff-story framing that may compromise other design aspects. Instead, structural engineers must weigh options to determine the most effective design for the owner's needs.

Other considerations that must be taken into account include cost and aesthetics. Designers must consider not only material costs, but also fabrication and installation costs. For instance, a lightweight building may have a low material cost but many members, which increases both fabrication and installation costs. Also, when comparing moment frame systems to braced frame systems, these cost differences can
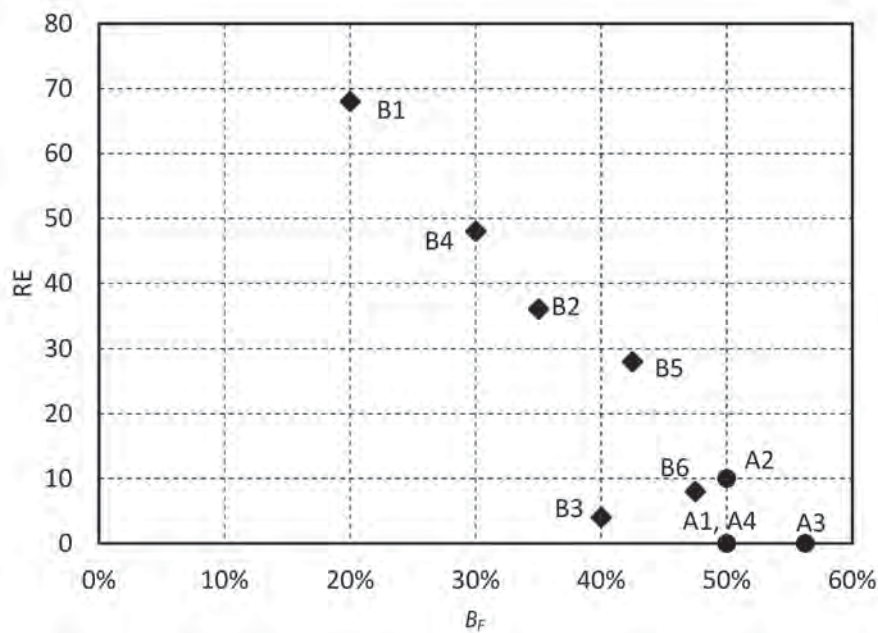
Fig. 13. Bracing factor, B_F, *versus elements requiring redesign, RE.*

Table 3. Sample Relative Cost Considerations			
Cost Category	Braced Frames	Moment Frames	Gravity Frames
Material cost (per lb)	Wide flanges: $0.49 Tube shapes: $0.56		
Fabrication cost (per connection)	$200	$200	$200
Installation (per connection)	$200	$800	

be significant. Braced frame systems are typically lighter weight than moment frame systems, which require large sections to resist drift demands; however, braced frames do not typically have the redundancy of moment frame systems. As shown in the configurations that were presented, moment frame systems are less likely than braced frame systems to be susceptible to collapse mechanisms due to redundancy.

Table 3 displays some approximate cost estimates for a typical low-rise steel building in a low seismic region, provided by a steel fabricator in the Midwest. Transportation costs and detailing are not included in these cost estimates. The fabrication and installation costs provided in the table do not reflect a particular member or connection size. The braced frame connection cost assumes a shop-welded gusset plate that is field welded to the bracing member using plates. The moment frame connection cost conforms to a WUF-B configuration (welded unreinforced flange and a bolted web). Finally, the gravity connection assumed was a typical shear tab connection with a shop-welded single

plate that is field-bolted to the beam web. While the authors acknowledge that the size of the framing members and specific details of the connection will alter the individual cost per connection, the costs reflected in the table are ballpark numbers based on industry experience to provide a quick comparison of different framing layouts as a means to weigh options.

As the table shows, moment connections can be 2.5 and 5 times more expensive than braced connections and gravity shear tab connections, respectively. To determine the percentage increase in building cost, a $15/ft^2 estimate can be used to conservatively estimate material, fabrication and installation costs for a traditionally framed building.

The costs provided in Table 3 were utilized to compare relative connection costs of each building configuration. For each configuration, the total perimeter connection costs were divided by the cost for shear connections at the perimeter framing. This provided a normalized connection cost that is reported on the Y-axis of Figure 14. When compared
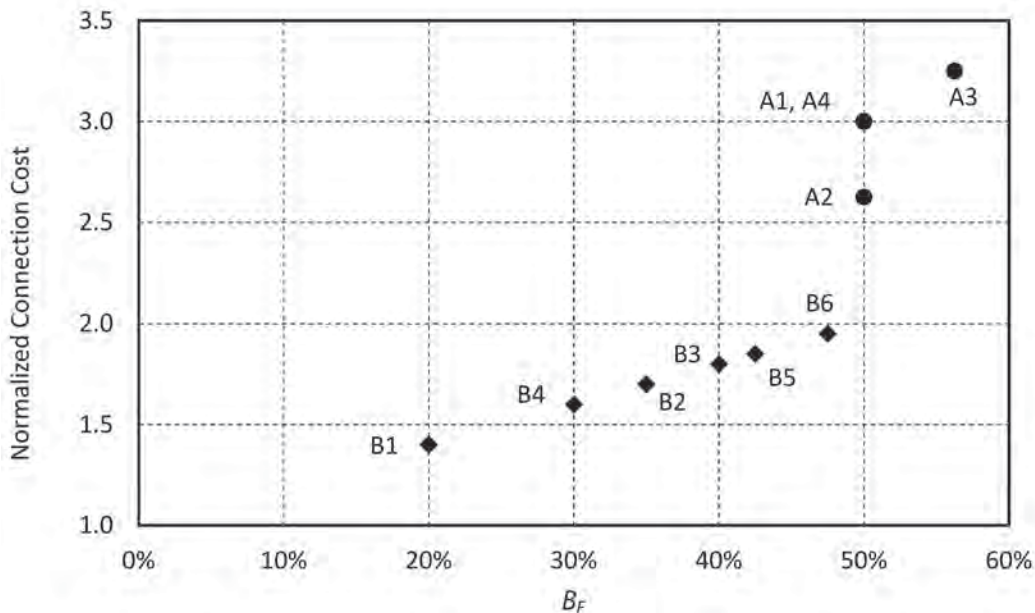
Fig. 14. Normalized connection cost versus bracing factor, B_F.

with the bracing factor, it is evident that an increased bracing factor typically constitutes an increase in connection cost. Additionally, it is clear that while moment frames are effective for distributing loads and providing a high bracing factor, they are significantly more expensive than braced frames.

When comparing the normalized connection cost for each configuration with the members requiring redesign, there is an inverse relationship, as shown in Figure 15. From this graph, it becomes evident that continuing the stiff story around the perimeter can result in a cost-effective increase in robustness. This is clearly observed in configurations B2–B3 and B5–B6, which, for a relatively small increase in connection cost, had a substantial reduction in RE. For more detailed cost comparisons between configurations, material costs could be considered as well.

Building aesthetics are also an important parameter to consider. Braces may negatively affect building views, compromise the exterior aesthetic envisioned by the architect, or inhibit the architectural programming and layout of the space. Similarly, moment frames, which require large members to control drift, could encroach on desired ceiling heights and views. To implement stiff stories without compromising the architectural aesthetic, engineers are encouraged to work with architects to locate stiff stories at levels would that minimize negative architectural impacts. For instance, hat-truss systems are sometimes located at mechanical levels, where views and aesthetics are less important. Skidmore, Owings & Merrill LLP (SOM) used this approach to design a 25-story office tower, which was constructed in Salt Lake City, Utah (SOM, 2016). By strategically designing framing to distribute stiffness and redundancy throughout the structure while balancing cost and aesthetics, the resulting structure can be robust, efficient, and aesthetically pleasing.

CONCLUSIONS

This paper described a study of framing strategies, many of which implemented stiff stories, and an approach for evaluating various configurations for system robustness in the event of a column loss. The configurations were studied using alternate path linear static analysis to evaluate unique column removal scenarios at the ground level.

Results from the analyses showed that any stiff-story framing strategy that is integrated with the LFRS and supports all columns will be more robust than traditional framing. Stiff stories were shown to effectively redistribute loads in column loss scenarios. In particular, when using a braced frame system, continuing the stiff story around the entire perimeter of the building story can substantially increase the number of members that meet acceptance criteria. The moment frame structures studied were more redundant than the braced frame systems, providing more opportunity for load redistribution; however, moment frame structures are also typically more expensive.

Vulnerability indices were developed to evaluate and measure relative robustness among framing strategies. The support factor, S_F, provides some indication of the relative robustness of the system, while the bracing factor, B_F,
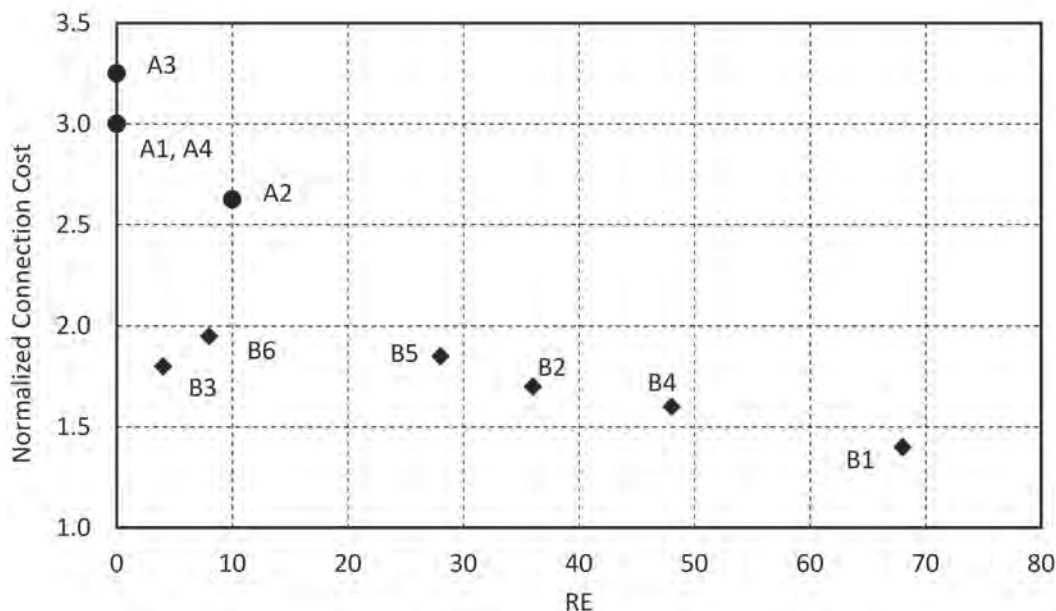
Fig. 15. Normalized connection cost versus members requiring redesign, RE.

provides an indication of the relative effectiveness of a particular framing configuration in resisting collapse. These factors can be used as a first screening when determining the capacity of a particular building in resisting column loss, while also considering cost and aesthetics. A higher B_F generally means a lower number of members requiring redesign (RE); thus, a higher bracing factor is typically preferred. However, an increased bracing factor and lower RE also generally means an increased building cost.

The implications of each framing strategy vary based on building size, location, use, etc. Structural engineers must work with the client and architect to determine the proper trade-off of desired building performance versus cost and aesthetics. From the analyses conducted in this study, the most successful configurations integrated LFRSs with a stiff story around the perimeter to minimize connection costs while still achieving significantly improved robustness.

REFERENCES

AISC (2010), *Specification for Structural Steel Buildings*, ANSI/AISC 360-10, American Institute of Steel Construction, Chicago, IL.

ASCE (2007), *Seismic Rehabilitation of Existing Buildings*, ASCE/SEI 41-06, American Society of Civil Engineers, Reston, Virginia.

ASCE (2010), *Minimum Design Loads for Buildings and Other Structures*, ASCE/SEI 7-10, American Society of Civil Engineers, Reston, Virginia.

Carter, C.J. (2011), "The Inherent Blast-Resistance of Steel Framing," *Modern Steel Construction*, AISC, August.

Cortes, G. and Liu, J. (2015), "Framing Strategies for Robustness in Steel Buildings," American Institute of Steel Construction, Final Report, August.

Cortés, G., Liu, J. and Francisco, T. (2015), "Framing Strategies for Robustness in Steel Buildings," *Proceedings of the ASCE Structures Congress*, April 23–25, Portland, Oregon.

CSI (2014), SAP 2000 v.17, Structural Analysis Program, Computers and Structures Inc., Berkeley, CA.

DoD (2009), *Design of Building to Resist Progressive Collapse*, UFC 4-023-03, U.S. Department of Defense, Washington, D.C.

Ellingwood, B.R., Smilowitz, R., Dusenberry, D.O., Duthinh, D., Lew, H.S. and Carino, N.J. (2007), "Best Practices for Reducing the Potential for Progressive Collapse in Buildings," NISTIR 7396, National Institute of Standards and Technology, Gaithersburg, MD.

Francisco, T. (2014), "Structural Integrity of the Composite Slab in Steel Composite Framing Systems," Doctoral Dissertation, Purdue University, West Lafayette, IN.

Johnson, E.S., Meissner, J. and Fahnestock, L. (2015), "Experimental Behavior of a Half-Scale Steel Concrete Composite Floor System Subjected to Column Removal Scenarios," *Journal of Structural Engineering*, Vol. 142, No. 2.

Liu, J.L. (2010), "Preventing Progressive Collapse through Strengthening Beam-to-Column Connection, Part 1: Theoretical Analysis," *Journal of Constructional Steel Research*, Vol. 66, No. 2, pp. 229–237.

Main, J.A. and Sadek, F. (2012), "Robustness of Steel Gravity-Frame Systems with Single-Plate Shear Connections," NIST Technical Note 1749, National Institute of Standards and Technology, Gaithersburg, MD.

Naderi, D., Adaros, M. and Wood, S. (2015), "Use of Ring Beams for Progressive Collapse Retrofit," *Proceedings of the ASCE Structures Congress*, April 23–25, Portland, Oregon, pp. 1183–1194.

SOM (2016), "Hat Truss-Supported Office Tower Tops Off in Downtown Salt Lake City," Skidmore, Owings & Merrill LLP, March, http://www.som.com/news/hat_truss-supported_office_tower_tops_off_in_downtown_salt_lake_city.

Weigand, J.M. (2014), "The Integrity of Steel Gravity Framing System Connections Subjected to Column Removal Loading," Ph.D. Dissertation, Department of Civil and Environmental Engineering, University of Washington, Seattle, Washington.

Weigand, J. and Berman, J. (2014). "Integrity of Steel Single Plate Shear Connections Subjected to Simulated Column Removal," *Journal of Structural Engineering*, Vol. 140, No. 5.

Assessment of I-Section Member LTB Resistances Considering Experimental Test Data and Practical Inelastic Buckling Design Calculations

LAKSHMI SUBRAMANIAN, WOO YONG JEONG, RAJA YELLEPEDDI and
DONALD W. WHITE

ABSTRACT

The current AASHTO and AISC *Specification* equations characterizing the lateral-torsional buckling (LTB) resistance of steel I-section members are the same, with minor exceptions, and are based in large part on unified provisions calibrated to experimental data. This paper takes a fresh look at the correlation of the flexural strength predictions from these equations with a large experimental data set compiled from research worldwide. To account fully for the moment gradient and end restraint effects present in the physical tests, the study employs practical buckling calculations using inelastic stiffness reduction factors (SRFs) based on the design resistance equations. The study focuses on uniform bending tests as well as moment gradient tests in which the transverse loads are applied at braced locations. Reliability indices are estimated in the context of building design. It is shown that a proposed modified form of the current resistance equations provides a more uniform level of reliability, as a function of the LTB slenderness, consistent with the target intended in the AISC *Specification*. The paper also calls attention to the limited experimental data pertaining to the inelastic LTB resistances in certain cases. The paper concludes by providing additional recommendations for LTB strength calculations in routine design, including illustrative plots conveying the impact of the proposed changes.

Keywords: lateral torsional buckling, inelastic buckling, experimental tests, AASHTO, AISC *Specification*, reliability indices.

INTRODUCTION

The AASHTO Specification (2016) and AISC *Specification* (2016) I-section member lateral-torsional buckling (LTB) strength curves are based largely on the so-called unified provisions (White, 2008). The unified provisions were developed given an extensive assessment of several large experimental datasets encompassing a wide range of member types and strength limit states (White and Jung, 2008; White and Kim, 2008; White et al., 2008). The unified AISC and AASHTO provisions differ in only a few minor technical details, which are discussed in the next section. They also differ in the form in which their rules are presented—the AISC *Specification* emphasizes the simplified design

of compact section members, the AASHTO Specifications feature the simplified design of slender-web members, and the unified provisions present the resistance equations as a single set of flowcharts covering all I-section member types.

Various researchers have observed that finite element (FE) test simulations using idealized boundary conditions and commonly employed deterministic residual stresses and initial geometric imperfections tend to exhibit smaller strengths than indicated by experimental data (Greiner et al., 2001; Kim, 2010; Lokhande and White, 2014; Subramanian and White, 2017a). This disconnect between test simulations and experimental test data has led to wide variations among the results from predictor equations derived predominantly from test simulations, such as the LTB equations defined in CEN (2005), versus those obtained from predictor equations derived predominantly from experimental tests, such as the AASHTO and AISC *Specification* equations. Figure 1, adapted from Ziemian (2010), illustrates the stark differences among the LTB strength predictions employed in various current international steel design standards. Engineers who work on both U.S. and international projects can observe predicted nominal strengths that differ by more than a factor of 2 in the most extreme cases. The reader is referred to Ziemian (2010) for a detailed discussion of the origins and nature of the curves in this plot.

It should be noted that if the members considered in Figure 1 are only slightly singly symmetric, the AISC

Lakshmi Subramanian, Ph.D., P.E., Visiting Professor, IIT Madras, Chennai, India. Email: pslakshmipriya@gmail.com

Woo Yong Jeong, Ph.D., Senior Software Engineer, Intergraph PP&M, Norcross, GA. Email: wooyong.jeong@intergraph.com

Raja Yellepeddi, Design Engineer, Stanley D. Lindsey and Associates Ltd., Atlanta, GA. Email: RYellepeddi@sdlal.com

Donald W. White, Ph.D., Professor, Georgia Institute of Technology, School of Civil and Environmental Engineering Atlanta, Georgia. Email: dwhite@ce.gatech.edu (corresponding)

Specification singly symmetric curve applies. According to the unified provisions, this is the appropriate LTB resistance curve for both doubly- and singly-symmetric sections. In addition, the reader should note that the curve for welded I-section members recommended by MacPhedran and Grondin (2009) is essentially identical to the Standards Association of Australia (SAA) (1998) strength curve. Lastly, it should be noted that the relatively optimistic predictions by MacPhedran and Grondin (2009) (compared to the majority of the other equations) is due to a lack of consideration of end restraint from adjacent test unbraced lengths and, hence, the use of a lateral-torsional buckling effective length factor of 1.0 in the prediction calculations (MacPhedran and Grondin, 2011). The CSA Group (2014) curve is based largely on the statistical analysis conducted by Baker and Kennedy (1984) of Dibley's (1969) rolled I-section member LTB tests, considering the effective lengths reported by Dibley; however, these same tests are included in the analyses by White and Jung (2004, 2008), providing validation of the unified provisions. Therefore, the conclusions from White and Jung (2004, 2008) and from Baker and Kennedy (1984) are at odds. The CSA Group (2014) curve appears to be more related to MacPhedran and Grondin's recommended curve, based on the use of $K = 1.0$. From White and Jung (2004), the unified provisions, using elastic LTB K factors per Nethercot and Trahair (1976), predict Dibley's 30 rolled I-section test resistances with a mean M_{test}/M_n of 1.017 and a coefficient of variation of 0.064. In addition, a substantially larger number of rolled I-section tests are considered in White and Jung (2004, 2008) and White and Kim (2004, 2008), as well as in this paper.

Subramanian and White (2017a) discuss the need to resolve the disconnects between FE test simulations, the AASHTO Specification (generally referred to in this paper as simply AASHTO) design strength equations, and experimental test data. It is essential to resolve these disconnects so that engineers can properly apply refined methods that move beyond traditional effective length and moment modification factors, K and C_b, where merited, to better quantify member LTB strengths. AISC *Specification* Appendix A provides guidance for conducting test simulations for design assessment; however, engineers who employ these methods typically will find that their calculated strengths are substantially smaller than strengths estimated using the ordinary AISC *Specification* Chapter F equations.

Subramanian and White (2017a, 2017b, 2017c) explain that the preceding disconnect can be resolved partly by the use of smaller nominal residual stresses and geometric imperfections in FE test simulations. This finding is based on correlation with experimental data as well as evaluation of sensitivity studies using test simulations (Subramanian and White, 2017a). However, these investigators also recommend the following modifications to the unified LTB resistance equations:

1. The plateau length, $L_p = 0.63 r_t \sqrt{E/F_{yc}}$, should be employed for all cross-section types (Subramanian and White, 2017b), as opposed to the use of this equation with a coefficient of 1.1 in the unified provisions. In addition to the findings by Subramanian and White, Greiner and Kaim (2001) and Kim (2010) have shown that test simulations suggest a smaller plateau length

Fig. 1. Comparison of nominal LTB resistances for W27×84 beams ($F_y = 50$ ksi)
and equivalent section welded beams subjected to uniform bending moment.

than indicated by the unified provisions (as well as by many current design specifications).

2. A smaller maximum stress level for elastic LTB of $F_{yr} = 0.5F_{yc}$ ($F_L = 0.5F_{yc}$ in the context of the AISC *Specification*) should be utilized for all cross-section types, including hybrid girders (Subramanian and White, 2017b). This change recognizes the fact that the LTB resistance can be affected significantly by the combined influence of residual stresses, unavoidable geometric imperfections, and second-order lateral-torsional displacement amplifications at unbraced lengths corresponding to the current F_{yr} (F_L) value of $0.7F_{yc}$.

3. The noncompact web slenderness limit, λ_{rw}, should be modified to

$$\lambda_{rw} = \left(3.1 + 2.5\frac{A_{fc}}{A_{wc}}\right)\sqrt{\frac{E}{F_{yc}}} \qquad (1)$$

$$\geq 4.6\sqrt{\frac{E}{F_{yc}}}$$

$$\leq 5.7\sqrt{\frac{E}{F_{yc}}}$$

(Subramanian and White, 2017b, 2017d). This change is based on observations, from physical tests and test simulations, that I-girders with relatively small flanges compared to the web area exhibit some reduction in their flexural resistances when their webs are near the current noncompact web limit. That is,

noncompact-web girders of this nature tend to perform more like slender-web girders.

Given the preceding recommendations, the proposed LTB resistance curve for the W27×84 and equivalent welded section members is as illustrated by the dark bold curve in Figure 2. It should be noted that the proposed L_p is comparable to the effective L_p values from the CEN (2005) Section 6.3.2.2 equations and that the proposed inelastic LTB curve is approximately tangent to the theoretical elastic LTB curve at the proposed L_r.

This paper takes a fresh look at the predictions relative to the experimental data for uniform moment and moment gradient tests in the context of the unified flexural resistance equations (White, 2008) as well as the above-proposed modifications to these resistance equations. With respect to moment gradient cases, the paper focuses on tests in which the transverse loads are applied at braced locations. Moment gradient tests considering loads applied at nonbraced locations as well as load height effects are addressed by Toğay et al. (2016). The experimental results considered in this paper include the prior data from White and Jung (2008) and White and Kim (2008) plus additional data from Kusuda et al. (1960) and Righman (2005).

In this paper, the nominal design resistances are determined using inelastic buckling calculations based on inelastic stiffness reduction factors (SRFs) obtained from corresponding design LTB resistance equations (White et al., 2016a). This approach allows for a practical, yet reasonably rigorous, accounting for (1) continuity effects across braced points, including the restraint of more heavily yielded member segments by adjacent unbraced lengths that
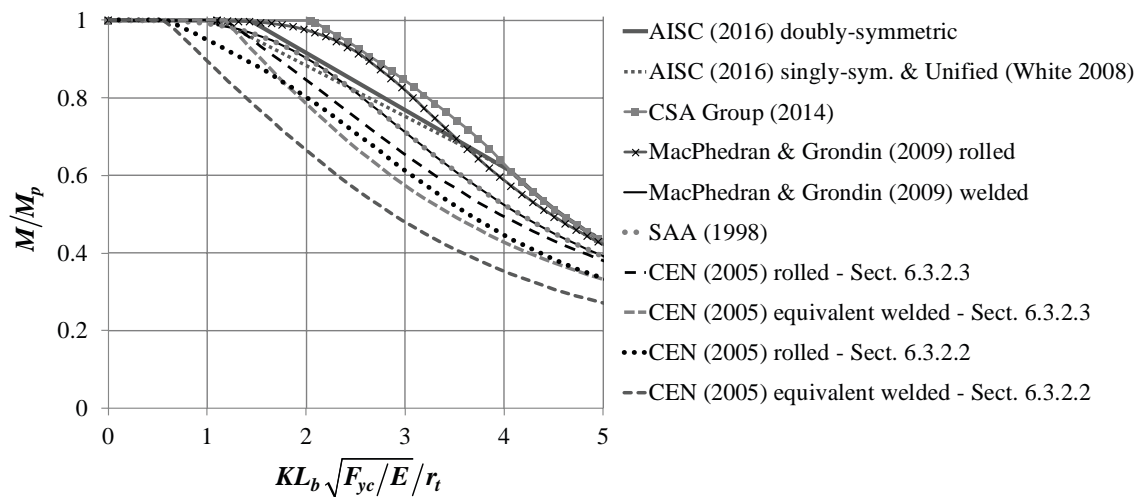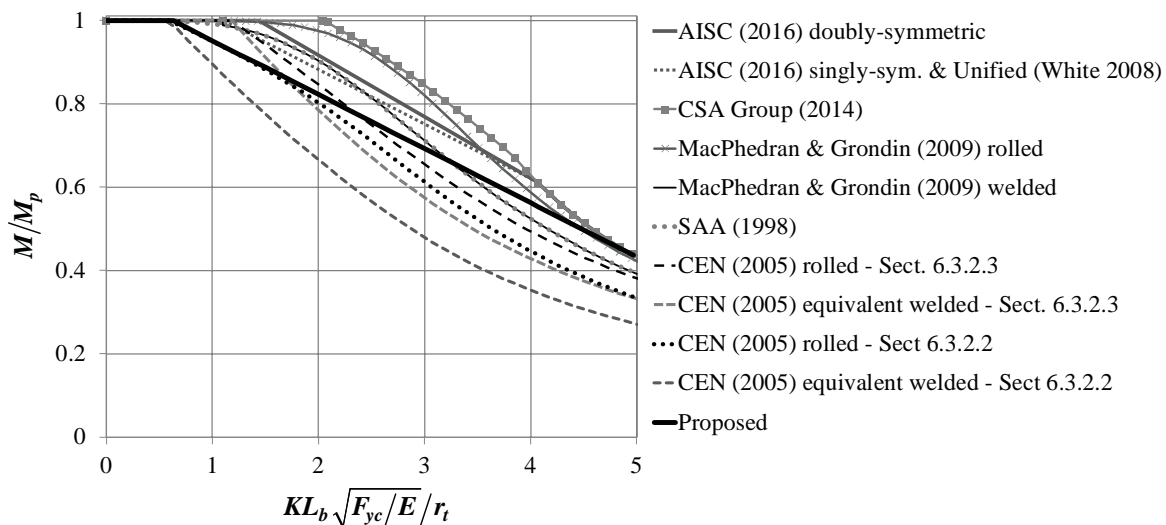

Fig. 2. Comparison of proposed LTB resistance for W27×84 beams ($F_y = 50$ ksi) and equivalent section welded beams subjected to uniform bending moment to current LTB resistance curves.

are relatively elastic (i.e., elastic and inelastic LTB effective length effects), and (2) variations in the spread of yielding along the member lengths due to moment gradient effects (i.e., effects approximated by C_b factors in common manual calculations). The subject inelastic buckling calculations are implemented within the SABRE2 software (White et al., 2016a, 2016b). SABRE2 applies the SRFs associated with the selected design LTB resistance equations along with thin-walled, open-section beam theory for the member strength assessment. SABRE2 allows the choice of either the unified LTB provisions or the proposed modifications to the design strength equations.

It is important to note that accounting for moment gradient effects, as well as end restraint effects from adjacent unbraced lengths and/or end connections, is essential to obtain any meaningful correlation between test and/or test simulation results and LTB strength predictions. The inelastic buckling solutions using the approach implemented in SABRE2 provide, in effect, exact member LTB effective lengths (inelastic or elastic, as applicable) based on the selected design resistance equations. These capabilities provide an unprecedented capability for engineers to account accurately for the combined influence of moment gradient and end restraint effects on the inelastic LTB strength limit states. However, the accuracy of this approach depends critically on the proper definition of the underlying LTB strength curve.

To evaluate the quality of the current unified and recommended modified LTB strength equations, this paper provides estimates of reliability indices, in the context of building design, using the preceding SRF-based approach for the prediction of the LTB test resistances. The reliability indices are estimated across a full range of LTB slenderness values. An important aim of this paper is to compare the reliability indices determined using the unified LTB provisions (which are the basis for the current AASHTO Specifications) to those obtained using the proposed modified LTB equations.

Lastly, the paper provides additional recommendations for LTB strength calculations in routine design, including a set of illustrative plots conveying the impact of the proposed changes.

OVERVIEW OF AISC, AASHTO AND UNIFIED LATERAL-TORSIONAL BUCKLING EQUATIONS

The lateral-torsional buckling (LTB) curves for I-section members in AASHTO (2016) and the AISC *Specification* (2016) consist of three distinct regions: the plateau region, the inelastic LTB region, and the elastic LTB region. The plateau resistance is equal to the plastic flexural strength for compact sections, while for noncompact web sections, it is the yield moment multiplied by the web plastification factor, R_{pc}. The plateau strength for slender-web sections is the yield moment reduced by the web bend-buckling factor, R_b (the parameter R_b in AASHTO is the same as the parameter R_{pg} in the AISC *Specification*). Members in uniform bending with effective unbraced lengths (KL_b) greater than L_r are designed using the theoretical elastic LTB strength, where L_r is the limiting unbraced length at which residual stresses, geometric imperfections, and second-order amplification of the lateral-torsional displacements start to influence the nominal resistance for this type of loading. Members with KL_b between L_p (the limiting length at which a member can attain the plateau strength) and L_r are designed using the inelastic LTB resistance, obtained by linearly interpolating between the plateau and the elastic LTB anchor points at L_p and L_r. It should be noted that both AASHTO and the AISC *Specification* give their LTB equations in terms of just the unsupported length between the braced points, L_b, recognizing the fact that the LTB resistance can be assessed conservatively and practically by assuming a LTB effective length factor of $K = 1$ in most situations. However, the commentaries of both specifications explain that KL_b may be used in place of L_b to obtain a more refined estimate of the LTB resistance when this beneficial refinement is merited.

The LTB equations in AASHTO and the AISC *Specification* follow the unified provisions (White, 2008) with minor exceptions. The differences among the unified provisions, the AISC *Specification*, AASHTO, and proposed modified provisions (Subramanian and White, 2017b) are shown in Table 1. The reader is referred to the AISC *Specification*, AASHTO, or White (2008) for all other equations required to calculate the LTB strengths.

This paper focuses on the differences in the strength predictions between the unified and the proposed modified LTB equations. These differences are quantified directly as well as via estimated reliability indices associated with the two sets of provisions. The paper also provides additional recommendations for LTB strength calculations in routine design, including a discussion of the impact of the proposed modifications.

SHORTCOMINGS OF THE UNIFIED PROVISIONS

The studies conducted in this research are an improvement over the prior calibrations (White and Jung, 2008; White and Kim, 2008) with respect to several key aspects discussed next.

Inelastic versus Elastic Effective Length Effects

The prior calibration of the unified flexural resistance provisions to experimental data (White and Jung, 2008; White and Kim, 2008) was conducted using approximate elastic effective length factors, $K_{elastic}$, calculated per Nethercot and Trahair (1976). When the critical unbraced length experiences some yielding, the restraint provided by adjacent

	Table 1. LTB Equation Comparisons			
Parameter	**Unified Provisions**	**AISC** *Specification*	**AASHTO**	**Proposed Equations**
L_p (doubly-symmetric, compact-web members with compact or noncompact flanges)	$1.1 r_t \sqrt{E/F_{yc}}$	$1.76 r_y \sqrt{E/F_y}$	$1.0 r_t \sqrt{E/F_{yc}}$	$0.63 r_t \sqrt{E/F_{yc}}$
L_p (all other I-section members)	$1.1 r_t \sqrt{E/F_{yc}}$	$1.1 r_t \sqrt{E/F_{yc}}$	$1.0 r_t \sqrt{E/F_{yc}}$	$0.63 r_t \sqrt{E/F_{yc}}$
F_{yr}*	$\min \begin{bmatrix} 0.7 F_{yc} \\ R_h F_{yt} \dfrac{S_{xt}}{S_{xc}} \\ F_{yw} \end{bmatrix}$ $\geq 0.5 F_{yc}$	$\min \begin{bmatrix} 0.7 F_y \\ F_y \dfrac{S_{xt}}{S_{xc}} \end{bmatrix}$ $\geq 0.5 F_{yc}$	$\min \begin{bmatrix} 0.7 F_{yc} \\ R_h F_{yt} \dfrac{S_{xt}}{S_{xc}} \\ F_{yw} \end{bmatrix}$ $\geq 0.5 F_{yc}$	$0.5 F_{yc}$
λ_{rw}	$5.7 \sqrt{\dfrac{E}{F_{yc}}}$	$5.7 \sqrt{\dfrac{E}{F_{yc}}}$	$5.7 \sqrt{\dfrac{E}{F_{yc}}}$	$\left(3.1 + 2.5 \dfrac{A_{fc}}{A_{wc}}\right)\sqrt{\dfrac{E}{F_{yc}}}$ $\geq 4.6 \sqrt{\dfrac{E}{F_{yc}}}$ $\leq 5.7 \sqrt{\dfrac{E}{F_{yc}}}$

* F_{yr} is denoted by F_L in the AISC *Specification*.

segments is typically more effective than when the critical segment is assumed to remain elastic (Subramanian and White, 2017b; Trahair and Hancock, 2004). This results in the theoretical $K_{elastic}$ being larger than the true effective length factor. Subramanian and White (2017b) show that the resulting larger estimated plateau length, L_p, in the unified provisions is due to the implicit inelastic effective length factor, $K_{inelastic}$, being smaller than $K_{elastic}$.

Due to the calibration to experimental test strengths using a larger elastic effective unbraced length ($K_{elastic}L_b$) instead of the smaller and true inelastic effective length ($K_{inelastic}L_b$), the test data are shifted toward the right in LTB strength plots. That is, for a given experimentally determined test strength, the corresponding elastic effective length is generally larger than the true inelastic effective length. The test strengths are, hence, incorrectly taken to be higher at longer lengths, resulting in a falsely optimistic calibration to the data. The use of $K_{inelastic}$ in the calibration to the test data correctly shifts the data toward the left in strength versus effective unbraced length plots compared to the prior calibrations.

Inelastic LTB effective length effects can be considered quite accurately and efficiently using tools such as SABRE2 (White et al., 2016b), which perform buckling analyses using inelastic stiffness reduction factors (SRFs) based directly on the specified design resistance equations. Similar approaches have been proposed by Trahair and Hancock (2004) in the context of the Australian standard (SAA, 1998) and by Kucukler et al. (2015a, 2015b) in the context of Eurocode 3 (CEN, 2005). The inelastic buckling calculations strictly do not require the calculation of any effective length factors. One can simply use the inelastic buckling analysis results directly. However, effective lengths are a convenient way of quantifying the LTB design resistances as a function of the end restraint (warping, lateral bending, and/or lateral displacement) provided to the critical unbraced length of a member.

The use of computational tools such as SABRE2 provides a major advantage over approximate $K_{elastic}$ or $K_{inelastic}$ calculations, in that the calculations are fast. Furthermore, the restraint from adjacent segments is implicitly accounted for, without the need for simplifying assumptions inherent in manual computations. For example, uniform moment tests conducted by Richter (1998) with several unbraced lengths within the test specimen, and with test fixtures providing restraint at the member ends, were assumed to have a K of 1.0 within the critical unbraced segments in the prior research by White and Jung (2004). [As noted earlier, the elastic LTB K factor estimates in these studies used the approach forwarded by Nethercot and Trahair (1976); this

approach gives an estimate of $K = 1$ in Richter's tests.] However, the authors have found that K is significantly smaller than 1.0 for the critical unbraced lengths when there are only three to five unbraced lengths (such as in Richter's tests) due to restraint from the end fixtures. It is only in the presence of a large number of adjacent unbraced segments subjected to uniform moment that $K_{inelastic}$ approaches 1.0. SABRE2 implicitly accounts for the general elastic–inelastic end restraint effects in the design calculation of the test strengths.

Inelastic versus Elastic Moment Gradient Effects

AASHTO and the AISC *Specification* apply a multiplicative moment gradient modification factor, C_b, to the elastic and inelastic LTB regions of the design curves in the case of moment gradient loading. That is, the unified provisions and both of these specifications simply multiply (i.e., scale) the elastic or inelastic LTB resistance by C_b, while limiting the corresponding resistance to the plateau strength. Numerous expressions for C_b exist in the literature—all of which are based on elastic buckling solutions. Subramanian and White (2017c) discuss the implications of using this elastically derived C_b in the inelastic LTB equations and report an "inelastic C_b" effect. That is, the basic C_b factor approach in the current AASHTO Specification and the AISC *Specification* tends to overpredict the moment gradient effects due to partial yielding in the members. This effect is relatively small when the maximum moment occurs at a braced point, as observed in the original developments by Yura et al. (1978). However, it can be more significant for transversely loaded cases, where the maximum moment occurs within an unbraced length. Computational tools such as SABRE2 implicitly account for this "inelastic C_b" effect. Thus, the calculated nominal strengths presented in this paper are expected to be more representative of the true member strengths.

EXPERIMENTAL TEST DATABASE

The experimental tests discussed in this paper are focused on noncomposite I-section members in which LTB is the controlling flexural limit state. Tests governed by flange local buckling (FLB) and tension flange yielding (TFY) limit states are addressed in the referenced prior studies. With the exception of the additional tests included from Kusuda et al. (1960) and Righman (2005), details of the test configurations, cross-section dimensions, and member properties are provided in White and Jung (2004) and White and Kim (2004). The data from the additional tests may be found in the corresponding reports. The prior datasets were a central focus in the development of the unified provisions (White, 2008), which serve as one basis for the current AISC and AASHTO flexural resistance provisions.

In the current study, the flexural resistances are calculated using inelastic buckling analysis procedures (White et al., 2016a) implemented in SABRE2 (White et al., 2016b). Inelastic SRFs for LTB are calculated using the unified provisions as well as the proposed modified provisions. The corresponding resistances are referred to respectively as $M_{nUnified}$ and $M_{nProposed}$. The test members are modeled using the measured geometry and separate measured flange and web yield strengths, where these data are available. The elastic modulus of the steel is taken as $E = 29{,}000$ ksi for all members. For rolled beams, the web-to-flange fillet areas are included in the models and in the underlying resistance calculations. Although this practice does not greatly affect the predicted strength of the members, it has been observed to give the best correlation with the test results (White and Jung, 2008). The web-to-flange fillet areas are taken as zero for welded sections.

The following detailed classifications of the test members are the same as in White and Jung (2004) and White and Kim (2004). Members for which the flange dimensions or the web depths are reported only as nominal values, or where these dimensions are reported to less than three significant digits, are considered as "nominal/approximate geometry." All other tests, including those in which the web thicknesses are reported as nominal values, or where only a single cross-section yield strength is provided, are considered as "accurate measured geometry." This is because of the minor influence of the web yield strength and thickness on the flexural resistance compared with the flange dimensions and the web depths. For rolled sections where the cross-section properties listed in the test reports do not include the web-to-flange fillet areas, the web-to-flange fillet areas are taken equal to the difference between the area listed in nominal property tables and the area calculated from the nominal plate dimensions. The web-to-flange fillet yield strengths are taken to be equal to the yield strength of the flange material.

The results in the following sections are delineated according to the normalized slenderness, c, defined as $\left(KL_b\sqrt{F_{yc}/E}\right)/r_t$. The effective length factor, K, is back-calculated as the value that, when substituted into the proposed LTB equations, yields the nominal resistance obtained from SABRE2 (based on the proposed equations). In the cases where the members attain the plateau resistance per SABRE2, the corresponding K factor is undetermined. In this case, K is calculated using the approximate elastic effective length procedure given by Nethercot and Trahair (1976), which is the procedure utilized in the prior development of the unified provisions (White, 2008). In the event that the plateau strength is not obtained using this $K_{elastic}$ value, K is determined as the largest value for which the member attains the plateau strength. Although this is a coarse estimate of K, it is reasonable considering that the K factors are employed

only to classify the experimental tests into different ranges based on the "LTB slenderness" in this work.

There is one exception to the preceding procedure. In the tests by Suzuki and Kubodera (1973), elaborate test fixtures were employed that provided ideal, torsionally simply supported end conditions on the test unbraced length while developing uniform bending moment within the test. In these cases, K is equal to 1.0. When these tests are modeled in SABRE2, LTB resistances precisely corresponding to the nominal resistance equations with an unbraced length $KL_b = L_b$ are obtained.

In the prior unified resistance calculations (White, 2008), the LTB plateau length is recommended as $L_p = 1.1r_t\sqrt{E/F_y}$ for all uniform bending cases, including rolled members. This equation is specified by AISC for all cross sections with the exception of doubly symmetric I-sections with compact webs and nonslender (i.e., compact or noncompact) flanges. AISC specifies $L_p = 1.76r_y\sqrt{E/F_y}$ for these section types. White and Jung (2008) and White (2008) explain that the latter of these AISC *Specification* equations provides an optimistic estimate of the plateau length and is, in fact, developed by (1) assuming that the design calculations will always use $K = 1$ and (2) dividing by an implicit $K < 1$ in the expression for L_p. The authors submit that a better approach is to allow engineers to apply an explicit $K < 1$ to L_b rather than hide the LTB effective length factor in the L_p equation. Alternatively, a more rigorous approach is to determine the LTB resistance directly, accounting for end restraint effects, via tools such as SABRE2 (White et al., 2016a, 2016b). In either of these situations, the use of $L_p = 1.76r_y\sqrt{E/F_y}$ amounts to a double counting of the end restraint effects, and therefore, this equation is not appropriate.

The unified L_p value is slightly larger than the value employed by AASHTO (2016). AASHTO uses $L_p = 1.0r_t\sqrt{E/F_y}$.

As noted by White and Kim (2008), although the collected experimental data sets are quite extensive, they are not sufficient to encompass the multitude of cross-section types and loading and displacement boundary conditions that form the complete design space. The acute scarcity of the experimental test data in certain inelastic LTB cases is discussed further in the section just prior to the conclusions of this paper. The proposed LTB strength curve (key parameters of which are summarized in Table 1) is based on the experimental data as well as a wider range of test simulations discussed by Subramanian and White (2017b, 2017c).

ESTIMATION OF RELIABILITY INDEX, β

The reliability indices presented in this paper are calculated as detailed in White and Jung (2008) and White and Kim (2008). These calculations, in turn, are based on the prior procedures established by Galambos et al. (1982). Based on the assumption that the resistance, R, and the load effect, Q, are log-normally distributed, the reliability index in the context of LRFD of steel building members is given by the expression

$$\beta = \frac{\ln\left(\dfrac{\overline{R}}{\overline{Q}}\right)}{\sqrt{V_R^2 + V_Q^2}} \tag{2}$$

where $\overline{R}$ and $\overline{Q}$ are the mean values of the resistance and load effects and V_R and V_Q are the respective coefficients of variation (Ellingwood et al., 1980; Ellingwood et al., 1982; Galambos, 2004; Galambos et al., 1982). The determination of $\overline{R}$, $\overline{Q}$, V_R and V_Q is described in detail in White and Jung (2008) and White and Kim (2008). The same procedures are adopted in this paper.

ASSESSMENT OF UNIFORM MOMENT TESTS

Figures 3 and 4 show the professional factors, M_{test}/M_n, from SABRE2 for the proposed and the unified equations considering the rolled and welded member uniform bending tests from the experimental database. The normalized resistances are plotted versus the normalized slenderness $c = (KL_b\sqrt{F_{yc}/E})/r_t$. The reader should note that $c = 1$ corresponds to the length L_p in the AASHTO Specification, whereas $c = 1.1$ corresponds to the length L_p in all cases with the exception of doubly-symmetric compact-web members having nonslender flanges in the AISC *Specification* (2016).

Tables 2 and 3 show the corresponding statistics on M_{test}/M_n. The number of different quantities presented in the tables is substantial; however, this is necessary to assess the ability of the resistance equations to predict the LTB strength limit states for all potential I-section member geometries. The test configurations and characteristics are discussed in detail by White and Jung (2004). Among the tests in the prior database, cases with cover plates and tests with a web depth-to-compression flange width ratio, D/b_{fc}, greater than 7.5 are not considered. A similar restriction on D/b_{fc} was employed by White and Jung (2004). The flexural resistance equations do not perform as well for the limited number of tests with D/b_{fc} larger than this limit. Table 2 summarizes the results for all the tests, including both accurate and nominal/approximate geometry. Table 3 shows the results only for the tests with accurate measured geometry. For c values less than or equal to 0.63, the predicted strengths are equal to the plateau flexural resistance both using the proposed as well as the unified provisions.

It can be observed from Figures 3 and 4 that there is generally a minor increase in the mean and minimum of M_{test}/M_n for the proposed equations compared to the unified equations. It is also observed that the dispersion of the test data in the different regions of c is largely the same for

both calculations. This is corroborated by the coefficient of variation (COV) values reported in Tables 2 and 3. In these tables, the variables N and V denote the number of tests and coefficient of variation of the strength ratio M_{test}/M_n. The following observations can be gleaned from Tables 2 and 3:

1. The statistics for $c \leq 0.63$ indicate that the experimental tests have no trouble attaining the plateau strength at small unbraced lengths. The COV considering all the tests is approximately 4%.

2. The statistics for $0.63 < c \leq 1$ are largely similar for the proposed and unified equations, except for welded

noncompact-web sections. For the tests of this type with accurate measured geometry, the proposed provisions give a slightly larger mean, M_{test}/M_n, of 1.04 versus 1.02 and a slightly smaller COV of 6.28% versus 7.71%. The tests listed in this category are all doubly-symmetric cross sections.

3. Rolled members in the range of $1 < c \leq 2$ show an increase of 0.05 in the mean and minimum values of M_{test}/M_n using the proposed equations compared to the unified equations in Table 2. Welded members show an increase of 0.05 and 0.06 for these values within this

◆ Adams, et.al (1964)
□ McDermott (1969)
△ Lee and Galambos (1962)
○ Dibley (1969)
+ Udagawa et al. (1973)
■ Wakabayashi et al. (1970)
− Suzuki and Ono (1970)
× Dibley (1970)
■ Lee, et.al (1964)
● Prasad & Galambos (1963)
- Janss & Masonet (1967)
▴ Driscoll & Beedle (1957)
× Dux & Kitipornchai (1983)
△ Wong-Chung & Kitipornchai (1987)
● Suzuki & Kubodera (1973)

(a)

◆ Adams, et.al (1964)
□ McDermott (1969)
△ Lee and Galambos (1962)
○ Dibley (1969)
+ Udagawa et al. (1973)
■ Wakabayashi et al. (1970)
− Suzuki and Ono (1970)
× Dibley (1970)
■ Lee, et.al (1964)
● Prasad & Galambos (1963)
- Janss & Masonet (1967)
▴ Driscoll & Beedle (1957)
× Dux & Kitipornchai (1983)
△ Wong-Chung & Kitipornchai (1987)
● Suzuki & Kubodera (1973)

(b)

Fig. 3. Uniform moment professional factors M_{test}/M_n *for rolled members: (a) unified equations; (b) proposed equations.*

range, considering the cases with nominal/approximate geometry. The trend is similar when only the tests with accurate measured geometry are considered (Table 3). Welded members with compact, noncompact and slender webs show increases in these values ranging from 0.05 to 0.09 in Table 2. The mean values change from slightly less than 1.0 to slightly greater than 1.0 for many of the cases.

4. The statistics for rolled members in the range of $2 < c \leq 3$ show an increase of 0.06 in the mean M_{test}/M_n using the proposed equations. This result is observed considering all tests as well as tests with only accurately measured geometry. The minimum value for the tests

with accurate geometry increases from 0.90 with the unified equations to 0.94 when the proposed equations are used. The increase in these values is larger for welded members. The mean and minimum of the test data for all the welded members increase by 0.08 by using the proposed equations (see Table 2). The increase is 0.06 for compact-web welded, 0.09 for noncompact-web welded, and 0.15 for slender-web welded members, considering all the available tests (Table 2). If only tests with accurate geometry are considered, the overall welded test mean and minimum M_{test}/M_n values increase by 0.09 for $2 < c < 3$. There are no compact-web welded members in this range

(a)

(b)
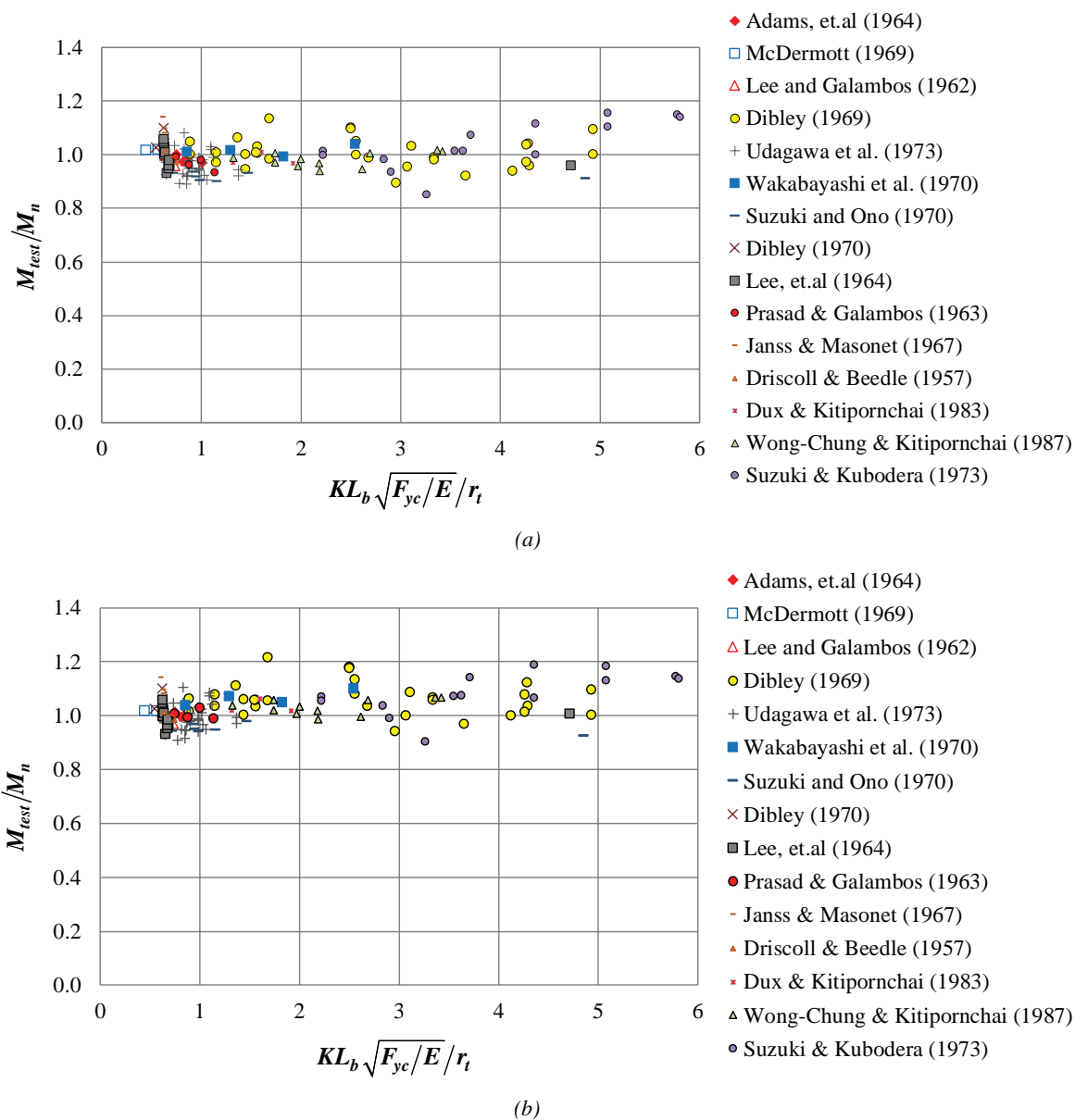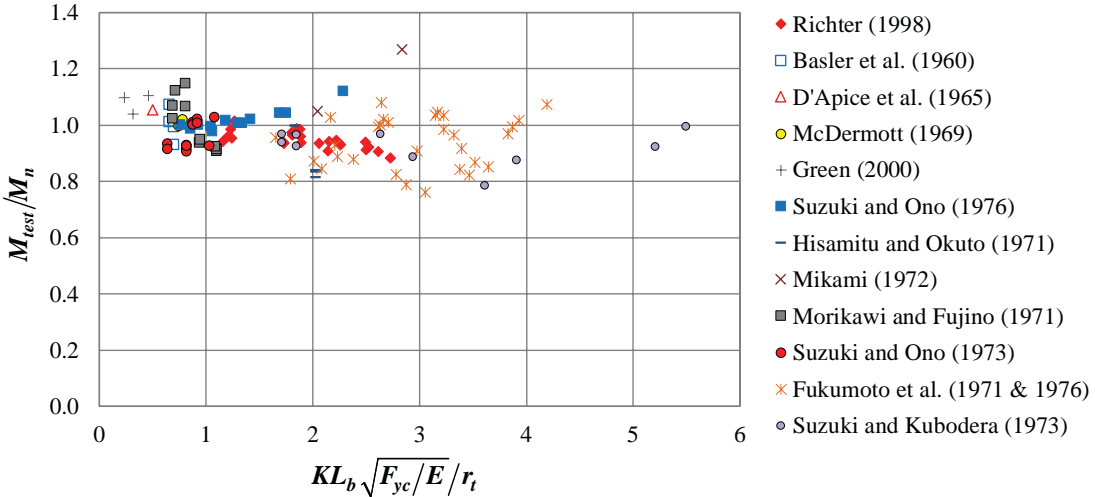
Fig. 4. *Uniform moment professional factors* M_{test}/M_n *for welded members: (a) unified equations; (b) proposed equations.*

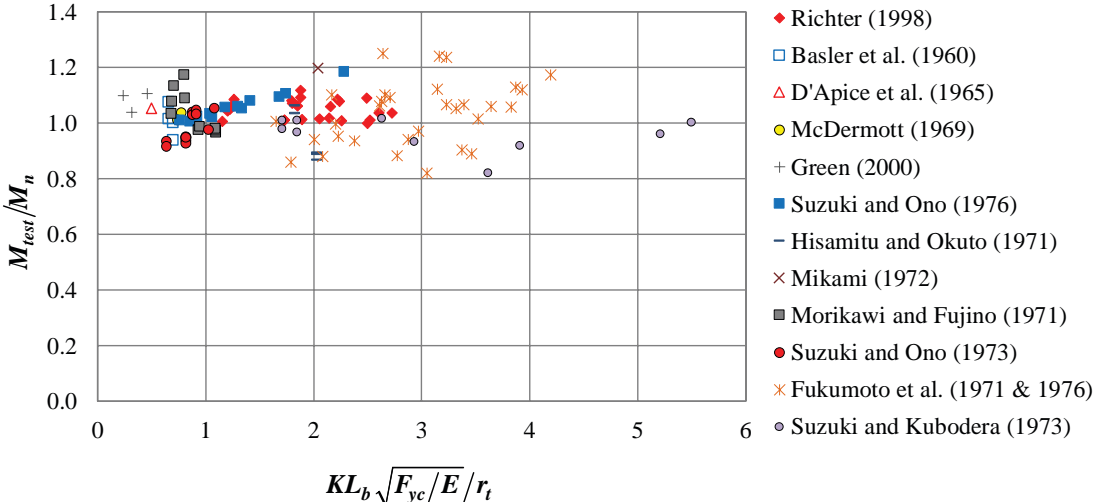| Table 2. M_{test}/M_n Statistics for Unified and Proposed LTB Equations—Uniform Bending Tests with Accurate and Nominal/Approximate Geometry											
(a) Rolled Members											
	$c \leq 0.63$	$0.63 < c \leq 1$		$1 < c \leq 2$		$2 < c \leq 3$		$3 < c \leq 4$		$c \geq 4$	
	M_{test}/M_n	$M_{test}/M_{nUnified}$	M_{test}/M_{nPr}	$M_{test}/M_{nUnified}$	M_{test}/M_{nPr}	$M_{test}/M_{nUnified}$	M_{test}/M_{nPr}	$M_{test}/M_{nUnified}$	M_{test}/M_{nPr}	$M_{test}/M_{nUnified}$	M_{test}/M_{nPr}
N	16	61		34		17		11		12	
Min	0.99	0.89	0.91	0.90	0.95	0.88	0.93	0.85	0.90	0.91	0.92
Median	1.03	0.98	0.99	0.98	1.03	0.99	1.04	1.01	1.07	0.98	1.03
Max	1.14	1.08	1.11	1.13	1.22	1.10	1.18	1.07	1.14	1.12	1.19
Mean	1.04	0.97	0.99	0.98	1.03	0.99	1.05	0.99	1.05	1.00	1.05
V (%)	4.07	4.46	4.00	4.86	5.05	6.14	6.78	6.08	6.20	6.16	6.56
(b) All Welded Members											
	$c \leq 0.63$	$0.63 < c \leq 1$		$1 < c \leq 2$		$2 < c \leq 3$		$3 < c \leq 4$		$c \geq 4$	
	M_{test}/M_n	$M_{test}/M_{nUnified}$	M_{test}/M_{nPr}	$M_{test}/M_{nUnified}$	M_{test}/M_{nPr}	$M_{test}/M_{nUnified}$	M_{test}/M_{nPr}	$M_{test}/M_{nUnified}$	M_{test}/M_{nPr}	$M_{test}/M_{nUnified}$	M_{test}/M_{nPr}
N	4	27		34		33		16		1	
Min	1.04	0.90	0.92	0.81	0.86	0.79	0.87	0.76	0.82		
Median	1.08	1.00	1.01	0.97	1.04	0.93	1.02	0.94	1.06		
Max	1.11	1.15	1.17	1.04	1.12	1.27	1.50	1.05	1.24		
Mean	1.07	0.99	1.01	0.97	1.03	0.94	1.03	0.92	1.03	1.07	1.17
V (%)	3.06	6.46	6.35	4.78	5.02	10.37	12.17	10.25	12.63		
(c) Rolled and Welded Members Combined											
	$c \leq 0.63$	$0.63 < c \leq 1$		$1 < c \leq 2$		$2 < c \leq 3$		$3 < c \leq 4$		$c \geq 4$	
	M_{test}/M_n	$M_{test}/M_{nUnified}$	M_{test}/M_{nPr}	$M_{test}/M_{nUnified}$	M_{test}/M_{nPr}	$M_{test}/M_{nUnified}$	M_{test}/M_{nPr}	$M_{test}/M_{nUnified}$	M_{test}/M_{nPr}	$M_{test}/M_{nUnified}$	M_{test}/M_{nPr}
N	20	88		68		50		27		13	
Min	0.99	0.89	0.91	0.81	0.86	0.79	0.87	0.76	0.82	0.91	0.92
Median	1.04	0.98	1.00	0.97	1.03	0.94	1.04	0.98	1.07	1.00	1.04
Max	1.14	1.15	1.17	1.13	1.22	1.27	1.50	1.07	1.24	1.12	1.19
Mean	1.05	0.98	1.00	0.97	1.03	0.96	1.04	0.95	1.04	1.01	1.06
V (%)	4.01	5.21	4.93	4.84	5.00	9.34	10.56	9.17	10.32	6.20	7.06
(d) Welded Members with Compact Webs											
	$c \leq 0.63$	$0.63 < c \leq 1$		$1 < c \leq 2$		$2 < c \leq 3$		$3 < c \leq 4$		$c \geq 4$	
	M_{test}/M_n	$M_{test}/M_{nUnified}$	M_{test}/M_{nPr}	$M_{test}/M_{nUnified}$	M_{test}/M_{nPr}	$M_{test}/M_{nUnified}$	M_{test}/M_{nPr}	$M_{test}/M_{nUnified}$	M_{test}/M_{nPr}	$M_{test}/M_{nUnified}$	M_{test}/M_{nPr}
N	3	16		20		18		10		0	
Min	1.04	0.90	0.92	0.81	0.86	0.81	0.87	0.76	0.82		
Median	1.10	0.99	1.01	0.99	1.04	0.90	0.96	0.92	0.98		
Max	1.11	1.02	1.05	1.04	1.11	1.12	1.19	1.04	1.12		
Mean	1.08	0.97	0.99	0.98	1.03	0.93	0.99	0.91	0.98		
V (%)	3.40	4.56	4.83	5.42	5.34	9.46	9.71	11.06	12.19		

Table 2. M_{test}/M_n Statistics for Unified and Proposed LTB Equations— Uniform Bending Tests with Accurate and Nominal/Approximate Geometry (cont'd)											
(e) Welded Members with Noncompact Webs											
	$c \leq 0.63$	$0.63 < c \leq 1$		$1 < c \leq 2$		$2 < c \leq 3$		$3 < c \leq 4$		$c \geq 4$	
	M_{test}/M_n	$M_{test}/M_{nUnified}$	M_{test}/M_{nPr}	$M_{test}/M_{nUnified}$	M_{test}/M_{nPr}	$M_{test}/M_{nUnified}$	M_{test}/M_{nPr}	$M_{test}/M_{nUnified}$	M_{test}/M_{nPr}	$M_{test}/M_{nUnified}$	M_{test}/M_{nPr}
N	0	5		5		4		0		0	
Min		0.94	0.98	0.94	1.01	0.91	1.00				
Median		1.02	1.03	0.94	1.01	0.93	1.01				
Max		1.12	1.13	1.01	1.09	0.94	1.02				
Mean		1.02	1.04	0.95	1.03	0.92	1.01				
V (%)		7.71	6.28	3.59	3.28	1.13	0.68				
(f) Welded Members with Slender Webs											
	$c \leq 0.63$	$0.63 < c \leq 1$		$1 < c \leq 2$		$2 < c \leq 3$		$3 < c \leq 4$		$c \geq 4$	
	M_{test}/M_n	$M_{test}/M_{nUnified}$	M_{test}/M_{nPr}	$M_{test}/M_{nUnified}$	M_{test}/M_{nPr}	$M_{test}/M_{nUnified}$	M_{test}/M_{nPr}	$M_{test}/M_{nUnified}$	M_{test}/M_{nPr}	$M_{test}/M_{nUnified}$	M_{test}/M_{nPr}
N	1	6		9		11		6		1	
Min		0.93	0.94	0.91	0.97	0.79	0.94	0.85	1.02		
Median		1.04	1.05	0.96	1.06	0.94	1.08	0.96	1.10		
Max		1.15	1.17	0.98	1.12	1.27	1.50	1.05	1.24	1.07	1.17
Mean	0.99	1.04	1.05	0.95	1.04	0.97	1.12	0.95	1.13		
V (%)		7.15	7.76	2.89	5.39	13.05	13.61	8.92	8.48		

considering only accurate geometry. The increases are 0.09 and 0.14 for both the minimum and mean values respectively for noncompact- and slender-web sections with accurate measured geometry. The mean values are closer to 1.0 with the proposed equations for several groups where the unified equations give values significantly less than 1.0.

5. The statistics for rolled members in the range of $3 < c \leq 4$ show an increase of 0.05 in the mean when the proposed equations are used for all the tests, as well as for the tests having only accurate measured geometry. The mean of the data increases by 0.11 from 0.92 with the unified equations to 1.03 when the proposed equations are used for the welded test specimens. There are no welded tests in this range with accurately measured geometry.

6. The statistics for rolled members show an increase of 0.05 and 0.04 in the mean of the data for nominal/approximate and accurate geometry in the range $c \geq 4$. There is only one welded member test in this range.

7. The COV for all the tests is largely similar for the proposed and unified equations in both Tables 2 and 3. It is observed that the COV is larger for tests in the middle of the inelastic LTB region in Table 2. When only the tests with accurate geometry are considered (Table 3), this COV is reduced. For example, in the range of $2 < c \leq 3$, the COV for welded members is reduced from 9.71% for all tests to 3.19% for accurately measured tests.

8. It is observed that the largest unconservatism of the unified equations is in the middle to end of the inelastic LTB region ($2 < c \leq 4$). The unified equations overpredict the experimental test data by as much as 14% for welded members with accurate geometry, and by as much as 32% for tests with nominal/approximate geometry (the minimum values of $M_{test}/M_{nUnified}$ are 0.88 and 0.76, respectively; therefore, $M_{nUnified}/M_{test}$ is equal to 1.14 and 1.32, respectively). This is consistent with the observations by Subramanian and White (2017a, 2017b, 2017c) that the unified equations tend to overpredict the finite element test simulation data within the inelastic LTB region. These observations are a key reason the proposed modifications should be implemented in the AISC *Specification* and AASHTO.

Figure 5 shows the reliability indices, estimated as explained in the previous section. The target reliability index in the AISC LRFD *Specification* is 2.6 for statically

	c ≤ 0.63	0.63 < c ≤ 1		1 < c ≤ 2		2 < c ≤ 3		3 < c ≤ 4		c ≥ 4	

Table 3. M_{test}/M_n Statistics for Unified and Proposed LTB Equations— Uniform Bending Tests with Accurate Measured Geometry

(a) Rolled Members

	c ≤ 0.63	0.63 < c ≤ 1		1 < c ≤ 2		2 < c ≤ 3		3 < c ≤ 4		c ≥ 4	
	M_{test}/M_n	$M_{test}/M_{nUnified}$	M_{test}/M_{nPr}	$M_{test}/M_{nUnified}$	M_{test}/M_{nPr}	$M_{test}/M_{nUnified}$	M_{test}/M_{nPr}	$M_{test}/M_{nUnified}$	M_{test}/M_{nPr}	$M_{test}/M_{nUnified}$	M_{test}/M_{nPr}
N	13	28		20		11		7		8	
Min	1.00	0.93	0.93	0.93	0.99	0.90	0.94	0.92	0.97	0.94	1.00
Median	1.05	0.99	1.00	0.99	1.04	0.99	1.04	0.99	1.07	0.99	1.02
Max	1.14	1.08	1.08	1.13	1.22	1.10	1.18	1.03	1.09	1.10	1.12
Mean	1.05	0.99	1.00	1.00	1.05	1.00	1.06	0.99	1.04	1.00	1.04
V (%)	3.91	3.28	3.13	4.46	4.68	6.42	7.29	3.91	4.14	5.34	4.63

(b) All Welded Members

	c ≤ 0.63	0.63 < c ≤ 1		1 < c ≤ 2		2 < c ≤ 3		3 < c ≤ 4		c ≥ 4	
	M_{test}/M_n	$M_{test}/M_{nUnified}$	M_{test}/M_{nPr}	$M_{test}/M_{nUnified}$	M_{test}/M_{nPr}	$M_{test}/M_{nUnified}$	M_{test}/M_{nPr}	$M_{test}/M_{nUnified}$	M_{test}/M_{nPr}	$M_{test}/M_{nUnified}$	M_{test}/M_{nPr}
N	2	13		16		11		0		0	
Min	1.05	0.93	0.94	0.91	0.97	0.88	1.00				
Median		1.02	1.03	0.96	1.05	0.93	1.04				
Max	1.11	1.15	1.17	1.01	1.12	0.95	1.09				
Mean	1.08	1.03	1.04	0.95	1.04	0.92	1.04				
V (%)		6.55	6.29	3.06	4.55	2.14	3.19				

(c) Rolled and Welded Members Combined

	c ≤ 0.63	0.63 < c ≤ 1		1 < c ≤ 2		2 < c ≤ 3		3 < c ≤ 4		c ≥ 4	
	M_{test}/M_n	$M_{test}/M_{nUnified}$	M_{test}/M_{nPr}	$M_{test}/M_{nUnified}$	M_{test}/M_{nPr}	$M_{test}/M_{nUnified}$	M_{test}/M_{nPr}	$M_{test}/M_{nUnified}$	M_{test}/M_{nPr}	$M_{test}/M_{nUnified}$	M_{test}/M_{nPr}
N	15	41		36		22		7		8	
Min	1.00	0.93	0.93	0.91	0.97	0.88	0.94	0.92	0.97	0.94	1.00
Median	1.05	1.00	1.01	0.97	1.04	0.94	1.04	0.99	1.07	0.99	1.02
Max	1.14	1.15	1.17	1.13	1.22	1.10	1.18	1.03	1.09	1.10	1.12
Mean	1.06	1.00	1.01	0.98	1.04	0.96	1.05	0.99	1.04	1.00	1.04
V (%)	3.84	4.80	4.77	4.41	4.52	6.22	5.59	3.91	4.14	5.34	4.63

(d) Welded Members with Compact Webs

	c ≤ 0.63	0.63 < c ≤ 1		1 < c ≤ 2		2 < c ≤ 3		3 < c ≤ 4		c ≥ 4	
	M_{test}/M_n	$M_{test}/M_{nUnified}$	M_{test}/M_{nPr}	$M_{test}/M_{nUnified}$	M_{test}/M_{nPr}	$M_{test}/M_{nUnified}$	M_{test}/M_{nPr}	$M_{test}/M_{nUnified}$	M_{test}/M_{nPr}	$M_{test}/M_{nUnified}$	M_{test}/M_{nPr}
N	1	2		2		0		0		0	
Min		1.00	1.01	0.98	1.05						
Median		1.01	1.02	0.99	1.06						
Max		1.02	1.04	0.99	1.06						
Mean	1.11	1.01	1.02	0.99	1.06						
V (%)		1.59	1.68	0.16	0.71						

Table 3. M_{test}/M_n Statistics for Unified and Proposed LTB Equations— Uniform Bending Tests with Accurate Measured Geometry (cont'd)											
(e) Welded Members with Noncompact Webs											
	$c \le 0.63$	$0.63 < c \le 1$		$1 < c \le 2$		$2 < c \le 3$		$3 < c \le 4$		$c \ge 4$	
	M_{test}/M_n	$M_{test}/M_{nUnified}$	M_{test}/M_{nPr}	$M_{test}/M_{nUnified}$	M_{test}/M_{nPr}	$M_{test}/M_{nUnified}$	M_{test}/M_{nPr}	$M_{test}/M_{nUnified}$	M_{test}/M_{nPr}	$M_{test}/M_{nUnified}$	M_{test}/M_{nPr}
N	0	5		5		4		0		0	
Min		0.94	0.98	0.94	1.01	0.91	1.00				
Median		1.02	1.03	0.94	1.01	0.93	1.01				
Max		1.12	1.13	1.01	1.09	0.94	1.02				
Mean		1.02	1.04	0.95	1.03	0.92	1.01				
V (%)		7.71	6.28	3.59	3.28	1.13	0.68				
(f) Welded Members with Slender Webs											
	$c \le 0.63$	$0.63 < c \le 1$		$1 < c \le 2$		$2 < c \le 3$		$3 < c \le 4$		$c \ge 4$	
	M_{test}/M_n	$M_{test}/M_{nUnified}$	M_{test}/M_{nPr}	$M_{test}/M_{nUnified}$	M_{test}/M_{nPr}	$M_{test}/M_{nUnified}$	M_{test}/M_{nPr}	$M_{test}/M_{nUnified}$	M_{test}/M_{nPr}	$M_{test}/M_{nUnified}$	M_{test}/M_{nPr}
N	1	6		9		7		0		0	
Min		0.93	0.94	0.91	0.97	0.88	1.02				
Median		1.04	1.05	0.96	1.06	0.94	1.06				
Max		1.15	1.17	0.98	1.12	0.95	1.09				
Mean	1.00	1.04	1.05	0.95	1.04	0.92	1.06				
V (%)		7.15	7.76	2.89	5.39	2.64	2.67				

determinate compact-section beams under uniform moment, based on a live load–to–dead load ratio (L/D) of 3. Bartlett et al. (2003) and Galambos (2004) have shown that 2.6 is a reasonable lower-bound reliability index for these member types when discretization error is not considered. In addition, White (2008) explains that the reliability index is 2.6 corresponding to the ASCE 7 load model and elastic LTB of general statically determinate beams. Rolled beams in general have been observed to have higher reliability than welded members (Galambos, 2004; White and Jung, 2008; White and Kim, 2008).

Figure 5 shows the reliability indices for various live load–to–dead load ratios, given a resistance factor, ϕ_b, of 0.9. The results presented in this paper do not consider discretization error (Bartlett et al., 2003). In cases where there are fewer than four tests, the reliability estimates are very coarse due to the sparsity of the test data. The evaluation of the reliability index for elastic LTB is discussed in White and Jung (2008) and is not reproduced here.

Figure 5 shows the reliability indices for both the unified and the proposed equations. The values for the unified equations are different in this paper compared to those shown in White and Jung (2008) because of the more accurate consideration of end restraint effects in the calculation of the ordinate values and the use of the more rigorous K factors in the calculation of the abscissa ($K_{inelastic}$ vs. $K_{elastic}$).

The following can be gleaned from Figure 5:

1. The reliability in the inelastic and less slender elastic LTB regions is increased by using the proposed equations. The target reliability is based on a live load–to–dead load ratio (L/D) of 3. For rolled members, the corresponding reliability index is as low as 2.4 for the unified equations in the region c ≥ 4. This value is improved to 2.7.

2. The reliability index for welded members is improved from 2.2 and 2.1 to 2.5 and 2.5 for $L/D = 3$ in the ranges of $2 < c \le 3$ and $3 < c \le 4$ for the tests that include nominal/approximate geometry. For tests with accurate geometry, both values increase from 2.5 to 2.9 for $L/D = 3$.

3. With the proposed equations, one obtains a more uniform reliability across all the LTB slenderness ranges.

ASSESSMENT OF MOMENT GRADIENT TESTS

Figures 6 and 7 show how the moment gradient experimental test results compare with results from SABRE2 for the unified and the proposed equations. Tables 4 and 5 show the results for the rolled and welded cross sections from the experimental database. The test configurations are detailed in White and Kim (2004), except for the tests from Kusuda et al. (1960) and Righman (2005). Among the tests in the prior database, tests containing cover plates and tests with a ratio of web depth to compression flange width $D/b_{fc} > 7.5$

are not considered in the statistics presented in this paper.

As in the case of the uniform moment tests, the parameter c is calculated based on the $K_{inelastic}$ value that yields the same theoretical strength as the inelastic buckling solution in SABRE2. In determining the $K_{inelastic}$ to be used in the expression for c, C_b is calculated from the equation developed by Salvadori (1955),

$$C_b = 1.75 + 1.05\left(\frac{M_1}{M_2}\right) + 0.3\left(\frac{M_1}{M_2}\right)^2 \le 2.3 \qquad (3)$$

(a) All tests (accurate and nominal/approximate geometry)—141 rolled members

(b) All tests (accurate and nominal/approximate geometry)—107 welded members

(c) All tests (accurate and nominal/approximate geometry)—248 rolled and welded members combined

(d) Tests with accurate measured geometry—87 rolled members

(e) Tests with accurate measured geometry—42 welded members

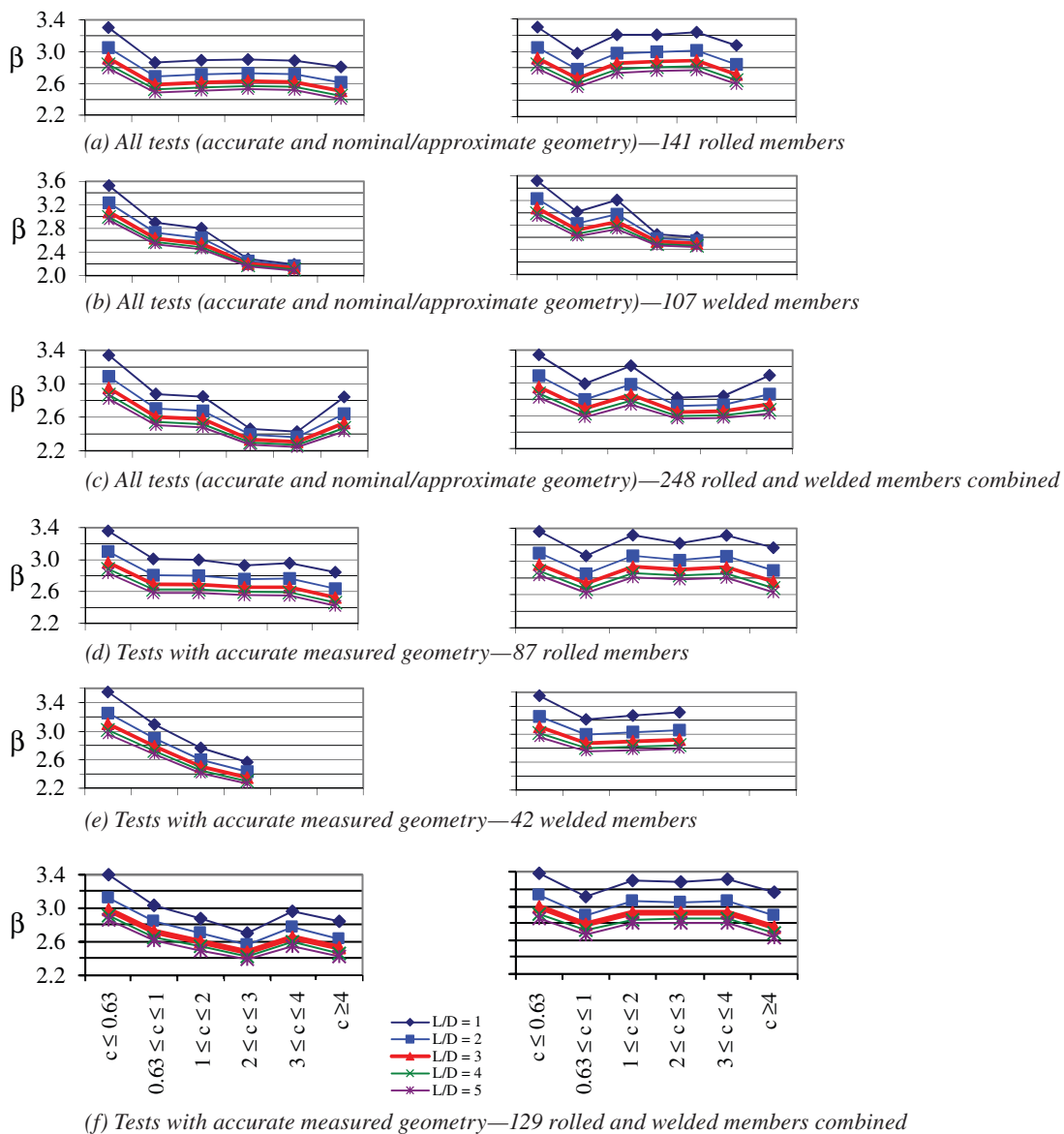*(f) Tests with accurate measured geometry—129 rolled and welded members combined*

Fig. 5. Reliability indices for uniform moment tests at various ranges of $c = \left(KL_b\sqrt{F_{yc}/E}\right)/r_t$ and live load–to–dead load ratios (L/D), $\phi = 0.9$; unified provisions (left) and proposed equations (right).

which is Equation C-F1-1 in the AISC *Specification* Commentary, where M_1 and M_2 are the smaller and larger moments at the ends of the unbraced lengths, respectively, and M_1/M_2 is positive for reversed curvature bending. This expression gives a better lower-bound elastic C_b factor compared to AISC *Specification* Equation F1-1 for cases where the moment diagram is linear between braced points. For example, given an unbraced length with zero moment at one end and maximum moment at the other end, Equation 3 gives $C_b = 1.75$ versus $C_b = 1.67$ using AISC *Specification* Equation F1-1. All the loading cases discussed in this paper fall under this category. Test cases where transverse loads are applied away from the brace points, and where load-height effects are predominant, are evaluated by Toğay et al. (2016). It should be noted that the preceding C_b approximation influences only the abscissa within the plots and the categorization of the tests in terms of their LTB slenderness in the tables because Equation 3 is used only in estimating $K_{inelastic}$. The ordinate values are determined directly using SABRE2 (White et al., 2016a, 2016b).

Similar to the uniform bending tests, there is one exception to the earlier calculation of $K_{inelastic}$. A number of the moment gradient tests involve three-point bending with equal unbraced lengths on each side of the braced point at the member midspan. In these cases, $K = 1$. When these tests are modeled in SABRE2, rigorous LTB resistances are

Fig. 6. Moment gradient professional factors M_{test}/M_n for rolled members: (a) unified provisions; (b) proposed equations.

obtained corresponding to the nominal resistance equations with an unbraced length $KL_b = L_b$, including an "inelastic C_b" effect.

The following can be observed from Figures 6 and 7:

1. Both the unified equations and the proposed equations tend to be conservative for smaller values of c. This is due to strain hardening effects, which are a predominant feature of moment gradient tests of compact-section members with short unbraced lengths.

2. Similar to the trends observed for the uniform moment tests, the proposed equations result in smaller predicted

flexural resistances, resulting in larger professional factors M_{test}/M_n. This changes the M_{test}/M_n for rolled members from values that are, in some cases, less than 1.0 to values that are predominantly 1.0 or higher.

3. An increase in the professional factors is also evident for the welded member tests, especially at longer unbraced lengths [e.g., see the data points from Frost and Schilling (1964) and Righman (2005) in Figure 7]. However, a number of these M_{test}/M_n values are still less than 1.0.

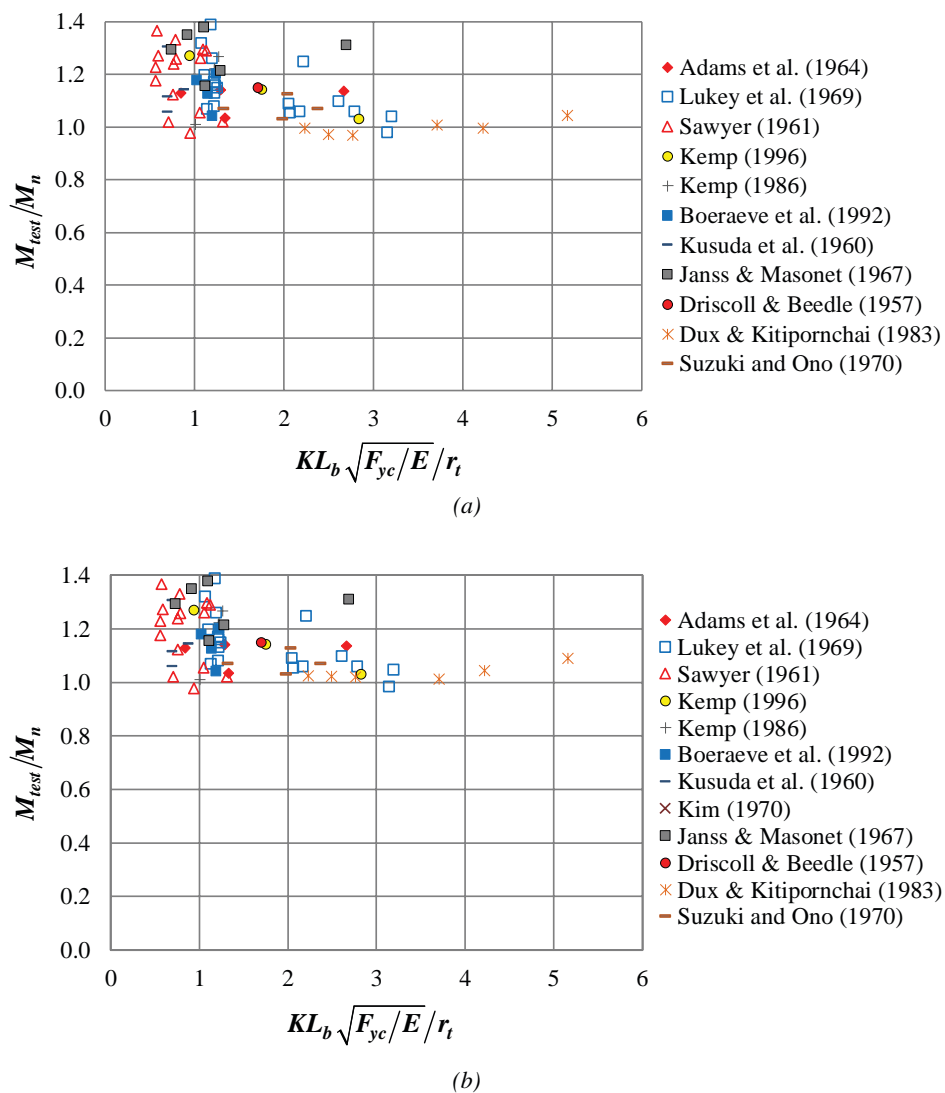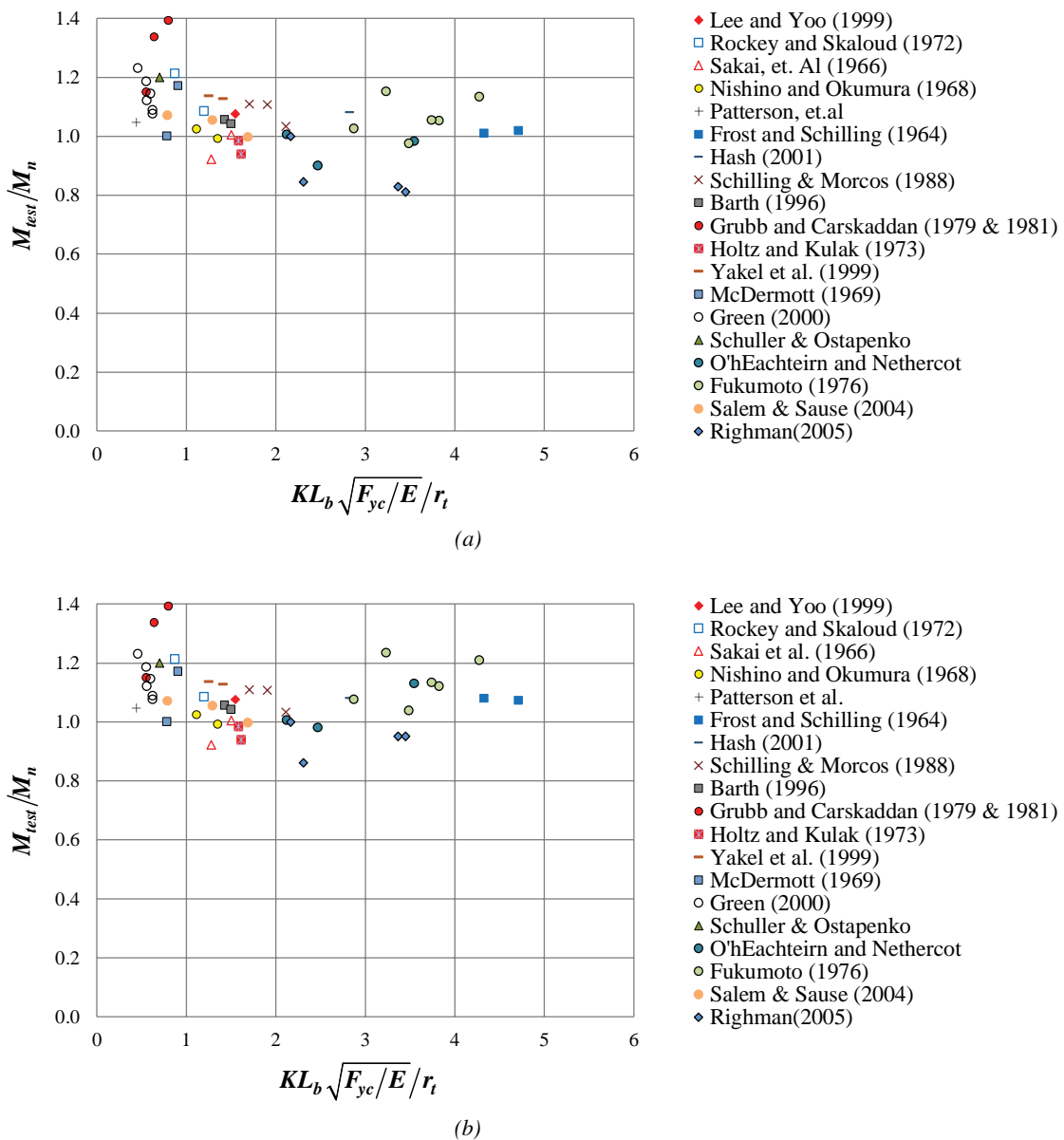Fig. 7. Moment gradient professional factors M_{test}/M_n for welded members: (a) unified provisions; (b) proposed equations.

Table 4. M_{test}/M_n Test Statistics for Unified and Proposed LTB Equations—Moment Gradient Tests with Accurate and Nominal/Approximate Geometry								
(a) Rolled Members								
	$c \leq 2$		$2 < c \leq 3$		$3 < c \leq 4$		$c \geq 4$	
	$M_{test}/M_{nUnified}$	M_{test}/M_{nPr}	$M_{test}/M_{nUnified}$	M_{test}/M_{nPr}	$M_{test}/M_{nUnified}$	M_{test}/M_{nPr}	$M_{test}/M_{nUnified}$	M_{test}/M_{nPr}
N	54		15		3		2	
Min	0.98	0.98	0.97	1.01	0.98	0.98	0.99	1.04
Median	1.20	1.20	1.06	1.06	1.01	1.01	1.02	1.07
Max	1.48	1.48	1.31	1.31	1.04	1.05	1.05	1.09
Mean	1.21	1.21	1.08	1.09	1.01	1.01	1.02	1.07
V (%)	10.24	10.24	8.81	7.92	3.00	3.18	3.52	3.12
(b) All Welded Members								
	$c \leq 2$		$2 < c \leq 3$		$3 < c \leq 4$		$c \geq 4$	
	$M_{test}/M_{nUnified}$	M_{test}/M_{nPr}	$M_{test}/M_{nUnified}$	M_{test}/M_{nPr}	$M_{test}/M_{nUnified}$	M_{test}/M_{nPr}	$M_{test}/M_{nUnified}$	M_{test}/M_{nPr}
N	53		7		7		3	
Min	0.92	0.92	0.85	0.86	0.81	0.95	1.01	1.07
Median	1.19	1.19	1.01	1.01	0.98	1.12	1.02	1.08
Max	1.62	1.62	1.08	1.08	1.15	1.24	1.13	1.21
Mean	1.18	1.18	0.98	1.01	0.98	1.08	1.05	1.12
V (%)	11.74	11.73	8.33	7.37	12.67	9.73	6.61	6.91
(c) Rolled and Welded Members Combined								
	$c \leq 2$		$2 < c \leq 3$		$3 < c \leq 4$		$c \geq 4$	
	$M_{test}/M_{nUnified}$	M_{test}/M_{nPr}	$M_{test}/M_{nUnified}$	M_{test}/M_{nPr}	$M_{test}/M_{nUnified}$	M_{test}/M_{nPr}	$M_{test}/M_{nUnified}$	M_{test}/M_{nPr}
N	107		22		10		5	
Min	0.92	0.92	0.85	0.86	0.81	0.95	0.99	1.04
Median	1.20	1.20	1.04	1.06	1.00	1.04	1.02	1.08
Max	1.62	1.62	1.31	1.31	1.15	1.24	1.13	1.21
Mean	1.19	1.19	1.05	1.06	0.99	1.06	1.04	1.10
V (%)	10.98	10.98	9.58	8.50	10.45	8.76	5.35	5.87
(d) Welded Members with Compact Webs								
	$c \leq 2$		$2 < c \leq 3$		$3 < c \leq 4$		$c \geq 4$	
	$M_{test}/M_{nUnified}$	M_{test}/M_{nPr}	$M_{test}/M_{nUnified}$	M_{test}/M_{nPr}	$M_{test}/M_{nUnified}$	M_{test}/M_{nPr}	$M_{test}/M_{nUnified}$	M_{test}/M_{nPr}
N	37		1		4		3	
Min	0.92	0.92			0.98	1.04	1.01	1.07
Median	1.21	1.21			1.06	1.13	1.02	1.08
Max	1.36	1.36			1.15	1.24	1.13	1.21
Mean	1.18	1.18	1.03	1.08	1.06	1.13	1.05	1.12
V (%)	10.99	10.99			6.81	7.09	6.61	6.91

Table 4. M_{test}/M_n Test Statistics for Unified and Proposed LTB Equations— Moment Gradient Tests with Accurate and Nominal/Approximate Geometry (cont'd)								
(e) Welded Members with Noncompact Webs								
	$c \leq 2$		$2 < c \leq 3$		$3 < c \leq 4$		$c \geq 4$	
	$M_{test}/M_{nUnified}$	M_{test}/M_{nPr}	$M_{test}/M_{nUnified}$	M_{test}/M_{nPr}	$M_{test}/M_{nUnified}$	M_{test}/M_{nPr}	$M_{test}/M_{nUnified}$	M_{test}/M_{nPr}
N	8				0		0	
Min	1.04	1.04						
Median	1.08	1.08						
Max	1.15	1.15						
Mean	1.09	1.09						
V (%)	3.49	3.51						
(f) Welded Members with Slender Webs								
	$c \leq 2$		$2 < c \leq 3$		$3 < c \leq 4$		$c \geq 4$	
	$M_{test}/M_{nUnified}$	M_{test}/M_{nPr}	$M_{test}/M_{nUnified}$	M_{test}/M_{nPr}	$M_{test}/M_{nUnified}$	M_{test}/M_{nPr}	$M_{test}/M_{nUnified}$	M_{test}/M_{nPr}
N	8		6		3		0	
Min	1.05	1.05	0.85	0.86	0.81	0.95		
Median	1.21	1.21	1.00	1.00	0.83	0.95		
Max	1.62	1.62	1.08	1.08	0.98	1.13		
Mean	1.25	1.25	0.98	0.99	0.87	1.01		
V (%)	15.43	15.41	8.96	7.40	10.86	10.29		

4. Two data points [one from Rockey and Skaloud (1972) and one from Righman (2005)] have essentially the same M_{test}/M_n with both the proposed and unified equations. This is because these tests achieve the plateau resistance in both predictions.

Table 4 shows the results for all tests, including cases with nominal/approximate geometry, and Table 5 shows the results for tests with only accurate geometry. Values of c that are less than or equal to 2.0 fall on the plateau of the LTB curves for both the unified and proposed provisions.

The following can be gleaned from Tables 4 and 5:

1. The test statistics for $c \leq 2$ indicate that the experimental tests have no trouble attaining the plateau strength and that both the unified and proposed equations are conservative. The mean M_{test}/M_n is as high as 1.21 for rolled members, both when considering all the tests and when considering only accurate geometry. The mean M_{test}/M_n for welded members is 1.11 for tests with accurate geometry and 1.18 for tests that include members with approximate geometry. The COV is similar for the unified and proposed equations. The COV is between 10 and 11% when the rolled and welded members are combined as one data set.

2. The test statistics for rolled members in the range of $2 < c \leq 3$ show a small increase in the mean M_{test}/M_n from 1.08 to 1.09 when using the proposed versus the unified equations. This is observed for all tests as well as tests with accurate measured geometry in this range. For rolled members, the minimum value of M_{test}/M_n for accurate geometry increases from 0.97 (unified equations) to 1.01 (proposed equations). The mean of the test data for all welded members (including approximate geometry) increases from 0.98 to 1.01 when using the proposed equations within this range of c. The M_{test}/M_n increases from 1.03 to 1.08 for a single compact-web welded member, and the mean M_{test}/M_n increases from 0.98 to 0.99 for slender-web welded members. There are no noncompact-web members in this range. All the slender-web welded members considered here have accurate measured geometry. There are no tests with compact or noncompact webs with accurate geometry.

3. The maximum M_{test}/M_n for rolled members in the range of $3 < c \leq 4$ increases from 1.04 to 1.05 when using the proposed equations for all tests as well as tests with accurately measured geometry. The mean of the data increases from 0.98 (unified equations)

Table 5. M_{test}/M_n Statistics for Unified and Proposed LTB Equations—Moment Gradient Tests with Accurate Measured Geometry							
(a) Rolled Members							
	$c \leq 2$		$2 < c \leq 3$		$3 < c \leq 4$		$c \geq 4$	
	$M_{test}/M_{nUnified}$	M_{test}/M_{nPr}	$M_{test}/M_{nUnified}$	M_{test}/M_{nPr}	$M_{test}/M_{nUnified}$	M_{test}/M_{nPr}	$M_{test}/M_{nUnified}$	M_{test}/M_{nPr}
N	52		13		3		2	
Min	0.97	0.98	0.97	1.01	0.98	0.98	0.99	1.04
Median	1.21	1.21	1.06	1.06	1.01	1.01	1.02	1.07
Max	1.48	1.48	1.31	1.31	1.04	1.05	1.05	1.09
Mean	1.21	1.21	1.08	1.09	1.01	1.01	1.02	1.07
V (%)	10.05	10.05	9.45	8.49	3.00	3.18	3.52	3.12
(b) All Welded Members							
	$c \leq 2$		$2 < c \leq 3$		$3 < c \leq 4$		$c \geq 4$	
	$M_{test}/M_{nUnified}$	M_{test}/M_{nPr}	$M_{test}/M_{nUnified}$	M_{test}/M_{nPr}	$M_{test}/M_{nUnified}$	M_{test}/M_{nPr}	$M_{test}/M_{nUnified}$	M_{test}/M_{nPr}
N	30		6		3		2	
Min	0.92	0.92	0.85	0.86	0.81	0.95	1.01	1.07
Median	1.11	1.11	1.00	1.00	0.83	0.95	1.01	1.08
Max	1.27	1.27	1.08	1.08	0.98	1.13	1.02	1.08
Mean	1.11	1.11	0.98	0.99	0.87	1.01	1.01	1.08
V (%)	7.71	7.71	8.96	7.40	10.86	10.29	0.62	0.53
(c) Rolled and Welded Members Combined							
	$c \leq 2$		$2 < c \leq 3$		$3 < c \leq 4$		$c \geq 4$	
	$M_{test}/M_{nUnified}$	M_{test}/M_{nPr}	$M_{test}/M_{nUnified}$	M_{test}/M_{nPr}	$M_{test}/M_{nUnified}$	M_{test}/M_{nPr}	$M_{test}/M_{nUnified}$	M_{test}/M_{nPr}
N	82		19		6		4	
Min	0.92	0.92	0.85	0.86	0.81	0.95	0.99	1.04
Median	1.16	1.16	1.03	1.03	0.98	1.00	1.01	1.08
Max	1.48	1.48	1.31	1.31	1.04	1.13	1.05	1.09
Mean	1.18	1.18	1.05	1.06	0.94	1.01	1.02	1.07
V (%)	10.16	10.16	10.21	9.10	10.29	6.81	2.10	1.89
(d) Welded Members with Compact Webs							
	$c \leq 2$		$2 < c \leq 3$		$3 < c \leq 4$		$c \geq 4$	
	$M_{test}/M_{nUnified}$	M_{test}/M_{nPr}	$M_{test}/M_{nUnified}$	M_{test}/M_{nPr}	$M_{test}/M_{nUnified}$	M_{test}/M_{nPr}	$M_{test}/M_{nUnified}$	M_{test}/M_{nPr}
N	18		0		0		2	
Min	0.92	0.92					1.01	1.07
Median	1.12	1.12					1.01	1.08
Max	1.27	1.27					1.02	1.08
Mean	1.12	1.12					1.01	1.08
V (%)	9.07	9.07					0.62	0.53

Table 5. M_{test}/M_n Statistics for Unified and Proposed LTB Equations—Moment Gradient Tests with Accurate Measured Geometry (cont'd)							
(e) Welded Members with Noncompact Webs							
	$c \leq 2$		$2 < c \leq 3$		$3 < c \leq 4$		$c \geq 4$	
	$M_{test}/M_{nUnified}$	M_{test}/M_{nPr}	$M_{test}/M_{nUnified}$	M_{test}/M_{nPr}	$M_{test}/M_{nUnified}$	M_{test}/M_{nPr}	$M_{test}/M_{nUnified}$	M_{test}/M_{nPr}
N	7		0		0		0	
Min	1.04	1.04						
Median	1.09	1.09						
Max	1.15	1.15						
Mean	1.09	1.09						
V (%)	3.73	3.76						
(f) Welded Members with Slender Webs							
	$c \leq 2$		$2 < c \leq 3$		$3 < c \leq 4$		$c \geq 4$	
	$M_{test}/M_{nUnified}$	M_{test}/M_{nPr}	$M_{test}/M_{nUnified}$	M_{test}/M_{nPr}	$M_{test}/M_{nUnified}$	M_{test}/M_{nPr}	$M_{test}/M_{nUnified}$	M_{test}/M_{nPr}
N	5		6		3		0	
Min	1.05	1.05	0.85	0.86	0.81	0.95		
Median	1.12	1.12	1.00	1.00	0.83	0.95		
Max	1.21	1.21	1.08	1.08	0.98	1.13		
Mean	1.13	1.13	0.98	0.99	0.87	1.01		
V (%)	6.65%	6.64%	8.96	7.40	10.86	10.29		

to 1.08 (proposed equations) for welded test sections with nominal/approximate geometry included within this range of c. The mean of the data increases from 0.87 to 1.01 for welded members when only tests with accurate geometry are considered. Clearly, 0.87 is a low value for the mean of the data. The minimum M_{test}/M_n for these section types in this range is only 0.81 using the unified equations. It increases to 0.95 using the proposed equations. However, only three tests, each with accurate geometry, are available for each of the rolled and welded member categories in this LTB region.

4. The test statistics for rolled members show an increase in the mean of the data from 1.02 to 1.07 for both nominal/approximate and accurate geometry in the range $c \geq 4$. The mean M_{test}/M_n for the welded members increases from 1.05 to 1.12 for the tests with accurate and nominal/approximate geometry and 1.01 to 1.08 for the tests with accurate measured geometry in this range. However, there are only two welded and two rolled member tests in this range that have accurate measured geometry.

5. The COV for all the tests is largely similar for the proposed and unified equations in Tables 4 and 5.

This is the same as the trend observed for the uniform moment tests.

6. For the moment gradient tests, it is observed that the largest unconservatism in the unified equations is in the inelastic LTB region ($3 < c \leq 4$), similar to the behavior for the uniform moment tests. The unified equations overpredict the experimental test data by as much as 23% for welded members with accurate and nominal/ approximate geometry, while the proposed equations overpredict the data by as much as 5% (the minimum of M_{test}/M_n in this range is 0.81 for the unified provisions and 0.95 for proposed equations; therefore, $M_{test}/M_n =$ 1.23 and 1.05, respectively). This overprediction of the test data is manifested clearly in the low reliability indices presented in Figure 8 and is discussed in detail next. The predictions by the current AISC *Specification* equations are identical to the unified provisions for all of these tests.

Figure 8 shows the reliability indices for the moment gradient tests, estimated as explained in the previous section on uniform moment tests. The following can be gleaned from this figure:

1. The reliability with respect to LTB is increased across all the ranges of LTB slenderness by using the proposed

equations. For rolled members, the target reliability of 2.6 for $L/D = 3$ is achieved for all ranges of c with the unified provisions. The estimated minimum reliability index is increased to 2.8 by using the proposed equations.

2. For tests that include nominal/approximate geometry and $L/D = 3$, the reliability index for welded members is improved from 2.5 and 2.3 to 2.7 and 2.9 in the ranges $2 < c \leq 3$ and $3 < c \leq 4$. For tests with accurate geometry, the values respectively increase from 2.4 and 1.9 to 2.6 and 2.5. When welded and rolled members

are considered together, the proposed equations give a reliability index estimate of 2.8 and 2.7 in these ranges of c.

3. For $L/D = 3$, the reliability index obtained using the unified equations is particularly low ($\beta = 1.9$) for welded members with accurate geometry in the region $3 < c \leq 4$. Figures 9 and 10 show the reliability indices for the welded members with accurate test geometry, considering two different ranges of C_b. Figure 9 summarizes the results for the unified provisions, whereas Figure 10 corresponds to the proposed
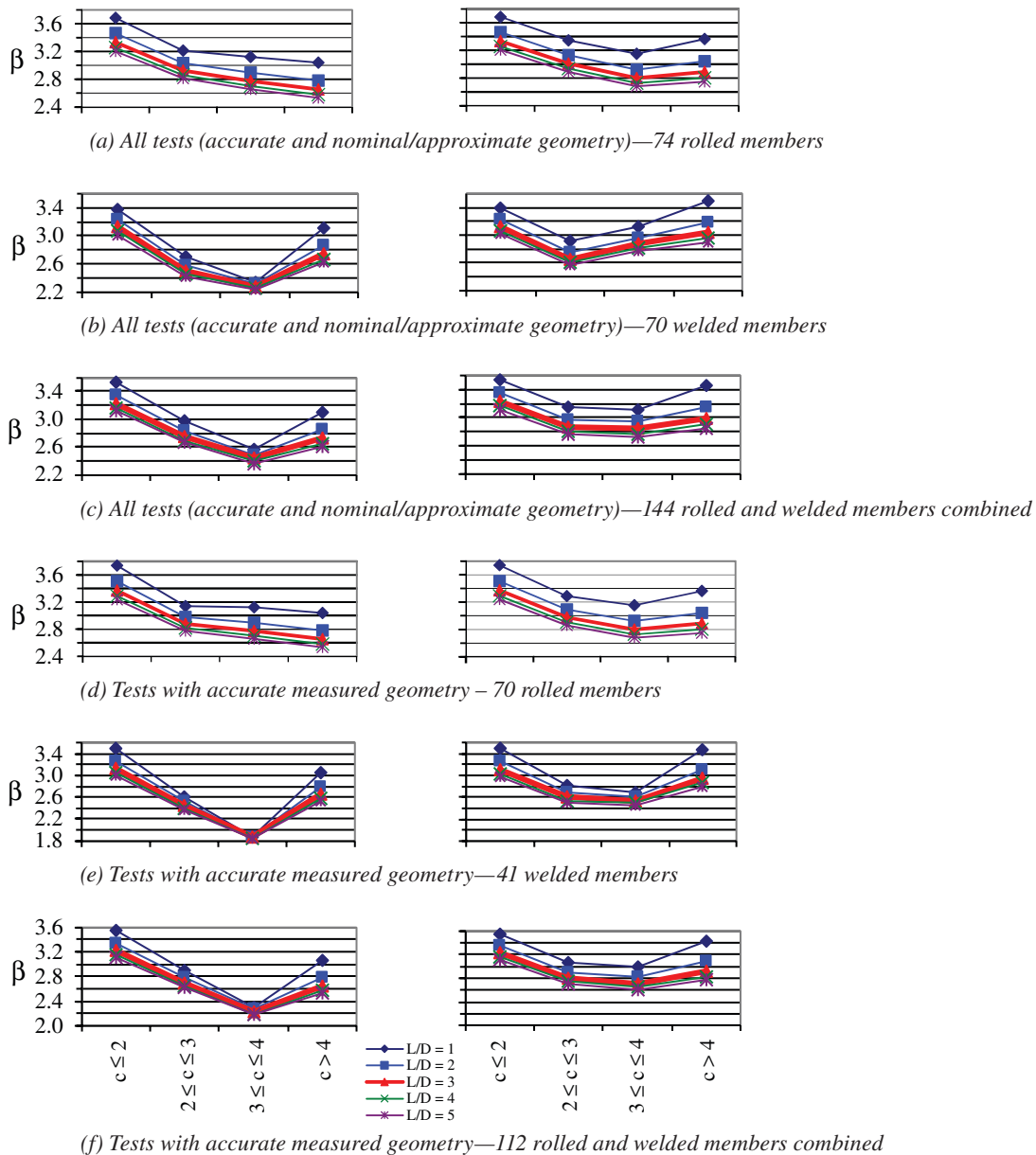

(a) All tests (accurate and nominal/approximate geometry)—74 rolled members

(b) All tests (accurate and nominal/approximate geometry)—70 welded members

(c) All tests (accurate and nominal/approximate geometry)—144 rolled and welded members combined

(d) Tests with accurate measured geometry – 70 rolled members

(e) Tests with accurate measured geometry—41 welded members

(f) Tests with accurate measured geometry—112 rolled and welded members combined

Fig. 8. Reliability indices for moment gradient tests at various ranges of $c = (KL_b\sqrt{F_{yc}/E})/r_t$ and live load–to–dead load ratios (L/D), $\phi = 0.9$; unified provisions (left) and proposed equations (right).

equations. The plots on the left show the results for all the tests that range from $C_b = 1.0$ to $C_b = 1.3$. The plots on the right are for tests with $C_b = 1.75$. It is observed that the moment gradient tests with the smaller C_b yield a lower estimated reliability index.

4. From Table 5, it can be seen that there are only three welded members in the range $3 < c \leq 4$, all of which have slender webs. Two out of these three tests are from Righman (2005) and were not included in the prior database calibration by White and Kim (2008). These test cross sections are extremely singly symmetric ($I_{yc}/I_{yt} < 0.3$) in addition to having slender webs ($\lambda_w > \lambda_{rw}$). Clearly, the current AASHTO equations are an inadequate predictor for these tests.

IMPACT OF PROPOSED MODIFICATIONS ON ROUTINE DESIGN STRENGTH CALCULATIONS

The preceding sections show that the proposed LTB equations result in a clear improvement in achieving a more uniform level of reliability across all ranges of LTB slenderness within the plastic and inelastic buckling ranges, consistent with the AISC LRFD *Specification* target of 2.6 for statically determinate beams and a live load–to–dead load ratio of 3. These reliability estimates are based on refined inelastic/elastic buckling solutions associated with the inelastic stiffness reductions implied by the LTB design equations (White

et al., 2016a, 2016b). As noted in the Introduction, accurate accounting for the moment gradient and end restraint effects on critical unbraced lengths is essential to achieving any meaningful correlation among experimental test data, test simulation results, and LTB strength predictions.

In routine practice, designers commonly assume $K = 1.0$ when calculating member LTB resistances. In these situations, when considering shorter and shorter critical unbraced lengths within the inelastic LTB range, the more extensive yielding within the critical unbraced length commonly results in a "true" LTB K factor that can be significantly less than 1.0. Related to this attribute, Yura et al. (1978) stated in the context of compact-section beams, "For uniform moment, the theory indicates that a very small bracing spacing of 2 ft. is required just to reach M_p … The apparent disagreement at the M_p level is due mainly to the torsionally pinned boundary conditions assumed in the theory. A laboratory beam that models actual conditions in practice must have adjacent spans to generate the moments. These spans will then also offer some restraint. Also, for beams with small unbraced lengths, the effects of boundary conditions are more dominating." Based on this behavior, the AISC *Specifications* have traditionally divided by an implicit effective length factor when setting the limiting length, L_p, for the plateau of the LTB resistance curves (White, 2008). With the advent of the 2005 AISC *Specification* (AISC, 2005), this practice has been limited to the L_p for doubly-symmetric nonslender flange members (i.e., 1.76 $r_y\sqrt{E/F_y}$). As demonstrated by
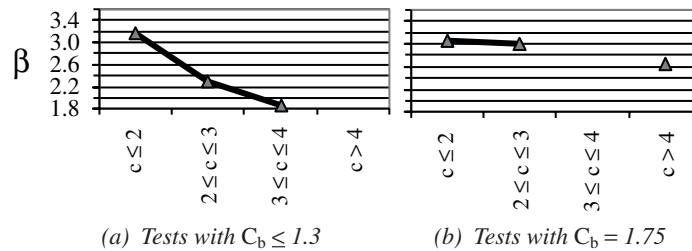

(a) Tests with $C_b \leq 1.3$ *(b) Tests with* $C_b = 1.75$

Fig. 9. Estimated reliability indices for the unified provisions, $L/D = 3$ *and* $\phi = 0.9$; *moment gradient tests of welded members with accurate test geometry.*

(a) Tests with $C_b \leq 1.3$ *(b) Tests with* $C_b = 1.75$
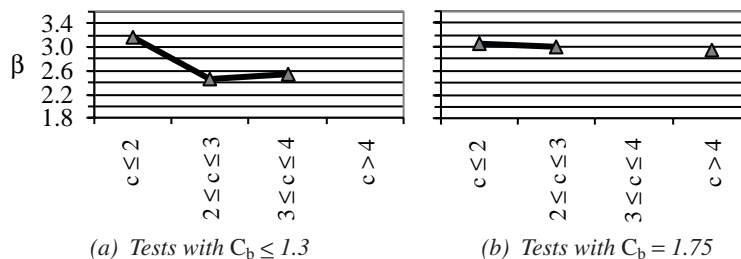
Fig. 10. Estimated reliability indices for the proposed equations, $L/D = 3$ *and* $\phi = 0.9$; *moment gradient tests of welded members with accurate test geometry.*

the correlations of the unified and proposed LTB equations with the experimental data, the use of this L_p equation is overly optimistic if employed with any LTB calculations that accurately account for end restraint effects. The use of this equation along with any other accounting for $K < 1$ amounts to a double counting of the end restraint effects. In addition, the equation $L_p = 1.76 \, r_y\sqrt{E/F_y}$ is inappropriate if one is comparing to the results of test simulations conducted using ideal torsionally simply supported end conditions (because this equation implicitly assumes that the unbraced length has significant end restraint).

In the context of the routine use of $K = 1.0$ in LTB calculations, and based on all of the earlier considerations, it is recommended that the expression for L_p can be divided by $K = 0.8$ for all types of I-section members. Even in beams that have physical end conditions that are very close to ideal torsionally simply supported, it is common to observe some incidental restraint. Furthermore, it can be inferred from Figures 5 and 8 (and Figures 3, 4, 6 and 7) that a small increase in L_p of this magnitude can be tolerated in terms of its influence on the estimated reliability.

Figures 11 through 15 show the impact of the recommended modifications relative to the corresponding unified resistance equations, including division of the proposed L_p equation by $K = 0.8$, resulting in the use of $L_p = 0.63r_t\sqrt{E/F_{yc}} / 0.8 = 0.8r_t\sqrt{E/F_{yc}}$. The moment capacity ordinate is normalized by the section plateau resistance, M_{max}, for the homogeneous slender-web member cases, where $M_{max} = R_{pg}M_{yc}$ using the AISC *Specification* notation or R_bM_{yc} using the AASHTO notation. The ordinate is normalized by the section yield moment M_y for the compact rolled-section member cases. The abscissa is the normalized unbraced length $L_b\sqrt{F_y/E} / r_t$ in all the plots.
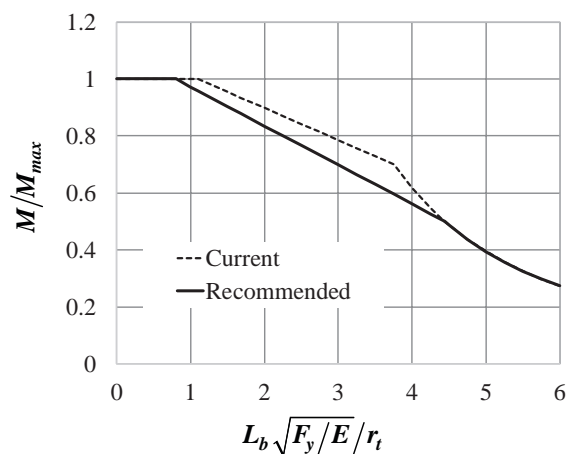
The following observations can be gleaned from Figures 11 through 15:

1. Figure 11 conveys the relationship between the unified and proposed LTB resistance curves for uniform bending of all types of slender-web members. One can observe that the recommended reduction relative to the unified resistance curve, which is identical to the AISC *Specification* LTB strength curve for these member types, ranges from 6.2% at the current L_p limit (i.e., at $L_b\sqrt{F_y/E} / r_t = 1.1$) to 15.7% at the current unified/ AISC *Specification* L_r limit. The proposed and current curves are coincident at normalized lengths larger than 4.44 (i.e., at lengths larger than L_r based on the proposed $F_L = 0.5F_{yc}$). The inelastic LTB portion of the recommended strength curve is nearly tangent to the theoretical elastic LTB curve at the proposed values of L_r.

2. Figure 12 shows comparable slender-web member curves for a representative moment gradient case with $C_b = 1.3$. In this case, there is no difference between the current and the proposed strength curves for normalized lengths smaller than 2.48 or larger than 4.44. The maximum difference between the curves is again 15.7%, corresponding to the current L_r.

3. Figure 13 shows the current and proposed LTB resistance curves for W36×150 members, which are representative of relatively lightweight, wide-flange rolled beams, subjected to uniform bending. It should be noted that for normalized lengths smaller than 1.8, the moment capacity of these members is larger than the yield moment M_y, and thus the member compression flange is extensively yielded throughout

Fig. 11. Current (unified) and proposed LTB strength curves for slender-web I-section members subjected to uniform bending moment.
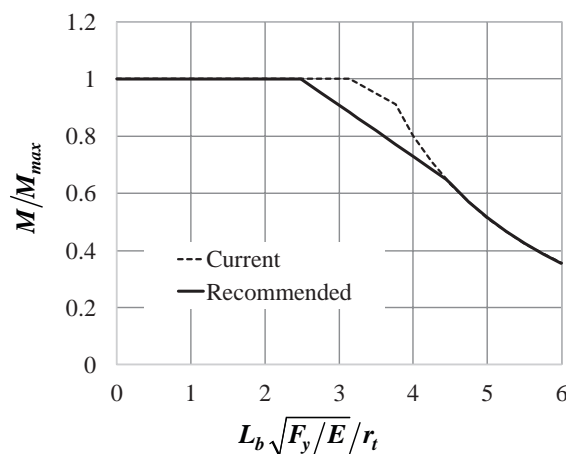

Fig. 12. Current (unified) and proposed LTB strength curves for slender-web I-section members subjected to moment gradient loading with C_b = 1.3.

the unbraced length. The reduction in the resistance relative to the current unified values varies from 6.0% at the normalized current unified L_p value of 1.1 to 8.9% at the current unified (and AISC *Specification*) L_r, which corresponds to a normalized length of 4.12. The curves become coincident for normalized lengths larger than 5.05, corresponding to the proposed L_r.

4. Figure 14 shows the results for the current and proposed W36×150 strength curves for a moment gradient case with $C_b = 1.3$. The curves are coincident for normalized lengths less than 2.53 and greater than 5.05. The largest reduction relative to the current unified resistance is again 8.9%.

5. Lastly, Figure 15 shows the results for W14×257 column-type rolled members. This is a representative

intermediate-weight column-type section. In this case, the recommended and current unified curves are practically coincident throughout the lengths shown in the plot. One should note that a normalized length of 7.2 corresponds to $L_b/r_y = 200$; therefore, it is expected that normalized lengths larger than 7.2 would be rare.

SHORTAGE OF EXPERIMENTAL DATA

It is evident from Tables 2 through 5 that despite the large total number of experimental tests used in the calibration of the AASHTO Specification LTB curves, there is a paucity of data in the inelastic LTB region. This is particularly the case for welded members with unbraced lengths close to L_r as defined by the proposed equations. For example, from Tables 2 and 3, it is seen that there is only one welded
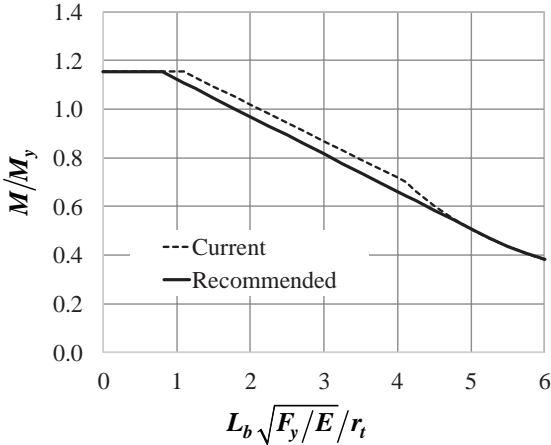

Fig. 13. Current (unified) and proposed LTB strength curves for W36×150 members subjected to uniform bending moment.
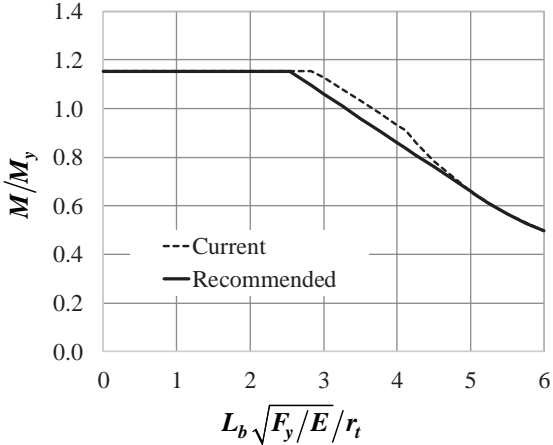

Fig. 14. Current (unified) and proposed LTB strength curves for W36×150 members subjected to moment gradient loading with $C_b = 1.3$.
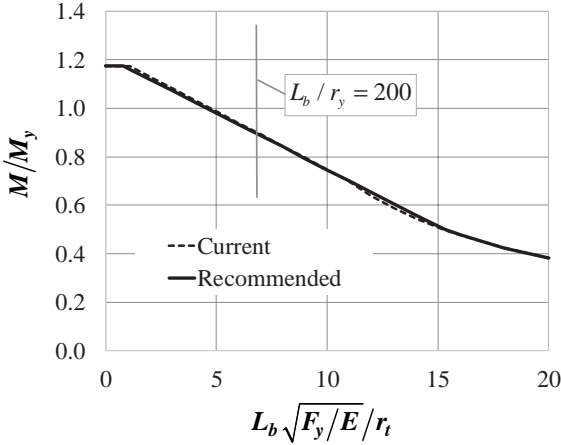

Fig. 15. Current (unified) and proposed LTB strength curves for W14×257 members subjected to uniform bending moment.

member experimental test in the region $c \geq 4$ subjected to uniform moment. This test is of a welded member with a slender web and nominal/approximate geometry. There are no experimental test data for welded members with accurate geometry or for members with compact and noncompact webs in this region. Table 3 shows further that there are no test data for welded members with compact webs and accurate measured geometry in the region $2 < c \leq 3$ and that there are only two tests in the region $1 < c \leq 2$. The number of noncompact-web welded member tests in these regions is five or less, with only a slightly higher number of available tests for slender-web members.

Tables 4 and 5 show that there is a scarcity of experimental test data in certain regions for both rolled and welded I-section members subjected to moment gradient loading. There are only three tests in the region $3 < c \leq 4$ and two in the region $c \geq 4$, for both rolled and welded members with accurate geometry. There are no welded member tests with compact webs in the regions $2 < c \leq 3$ and $3 < c \leq 4$ and only two tests in the region $c \leq 4$. There are no test data for welded members with noncompact webs for $c > 2$. While there are three slender-web welded member tests in the region $3 < c \leq 4$, it is important to note that two of these tests are from Righman (2005) and were not included in the prior calibration (White, 2008). Figures 9 and 10 show that the reliability is substantially improved in this region using the proposed equations. The unified equations are extremely unconservative in estimating the strengths observed in Righman's tests.

The scarcity of experimental data and the improved reliability in the inelastic LTB region using the proposed equations highlights the need to consider a larger database of tests for acceptable reliability computations. Subramanian and White (2017b, 2017c) propose the modified LTB equations based on FE test simulations that encompass a wide variety of cross sections, while simultaneously ensuring a fit to the available experimental data.

CONCLUSIONS

This paper presents a comprehensive analysis of the correlation between nominal strength predictions, obtained based on practical LTB calculations using inelastic stiffness reduction factors (SRFs), with a large suite of experimental data compiled from research worldwide. Both current design resistance equations as well as modified equations recommended by Subramanian and White (2017b, 2017c) are considered. The following are the key conclusions from this study:

1. The equations proposed herein and in Subramanian and White (2017a, 2017b, 2017c, 2017d) are shown to provide a more uniform reliability index compared with the unified provisions, based on the available experimental test data. The proposed equations also provide estimates of the reliability index that are all approximately equal to or greater than the intended values for statically determinate members in the AISC *Specification*. The sparsity of experimental tests in certain regions of the design space is countered by a large number of additional finite element test simulation studies in Subramanian and White (2017b, 2017c). Several important experimental tests are included that were not available at the time of the calibrations by White and Jung (2008) and White and Kim (2008). These tests include extreme singly symmetric slender-web cross sections with unbraced lengths in the inelastic LTB region. These tests indicate a relatively low reliability index for the unified provisions within the intermediate inelastic LTB range. The proposed equations address this shortcoming.

2. The use of inelastic SRFs in LTB calculations provides a practical means of accurately representing the restraining effects from adjoining unbraced lengths, as well as the moment gradient effects associated with partial yielding. The calculations for the effective length and moment gradient factors (K and C_b) in the prior calibration efforts have involved various simplifying assumptions. These simplifications, along with the availability of new test data subsequent to the prior calibration efforts, result in smaller levels of reliability than intended for the LTB strength curve in certain cases. This is particularly the case when the unified provisions are employed in the context of accurate accounting of end restraint and moment gradient effects, such as can be accomplished with practical inelastic buckling analysis methods.

Although the inelastic buckling calculations provide better estimates of the true strengths, engineers may also calculate the LTB design resistance using theoretical elastic effective length factors for the unbraced length, as given by Nethercot and Trahair (1976), or using other estimates. Elastic estimates provide larger values of K than those determined from inelastic buckling calculations. The LTB resistances thus calculated tend to be conservative relative to the "true" solutions. However, it should be noted that when end warping and/or lateral bending restraint are accounted for in the buckling calculations of members subjected to moment gradient, the combined effects of the commonly used K and C_b factors can lead to higher strength predictions than obtained using tools such as SABRE2 or refined finite element test simulations (Subramanian, 2015). That is, the C_b factor equations, which are commonly derived assuming torsionally simply supported end conditions, are not necessarily a good representation of the moment gradient effects in unbraced lengths having significant end warping and/or lateral bending restraint.

It is recommended that in routine design practice, when $K = 1$ is assumed in the LTB strength calculations, the proposed L_p value may be divided by an implicit K value of 0.8, thus providing some liberalization of the more restrictive L_p equation recommended when end restraint effects are addressed directly within the design calculations.

Additional experimental data and inelastic buckling predictions involving transverse loading on members with no intermediate brace points, including load height effects, are discussed by Toğay et al. (2016).

SYMBOLS

A_{fc}	Area of compression flange
A_{wc}	Area of web in compression
C_b	Moment modification factor
D	Dead load
D_c	Depth of web in compression measured from the inside of the compression flange
E	Modulus of elasticity
F_y	Yield strength of steel
F_{yc}	Yield strength of compression flange
F_{yr}	Compression flange stress at nominal onset of yielding including the effects of residual stresses, taken as $0.7F_y$ for homogeneous doubly symmetric I-sections in the AISC *Specification* and AASHTO, denoted by F_L in the AISC *Specification*.
K	Effective length factor for lateral-torsional buckling
$K_{elastic}$	Elastic effective length factor for lateral-torsional buckling
$K_{inelastic}$	Inelastic effective length factor for lateral-torsional buckling
L	Live load
L_b	Unbraced length of beam or girder
L_p	Limiting effective unbraced length below which the strength under uniform bending is characterized by the plateau resistance
L_r	Limiting effective unbraced length above which the strength under uniform bending is characterized by the theoretical elastic lateral-torsional buckling resistance

M_{max}	Maximum possible flexural resistance obtained for short member unbraced lengths, equal to M_p for compact section members and equal to $R_{pg}M_{yc}$ (AISC) $= R_bM_{yc}$ (AASHTO) for homogeneous slender-web members
$M_{n\ Unified}$	Moment calculated using the unified provisions
M_{nPr}	Moment calculated using the proposed changes to the AISC *Specification*, AASHTO, and unified LTB resistance equations
M_p	Plastic moment
M_{test}	Maximum moment obtained from experimental tests as reported by authors
M_y	Nominal yield moment
M_{yc}	Yield moment corresponding to the compression flange
M_{yt}	Yield moment corresponding to the tension flange
N	Number of experimental tests considered in the statistical analysis
Q	Load effects on member
$\overline{Q}$	Mean of load effects
R	Resistance of cross-section
$\overline{R}$	Mean of resistance effects
R_b	Web bend-buckling factor, which accounts for the typical decrease in the LTB plateau strength of slender-web sections due to load shedding to the compression flange caused by web bend-buckling, denoted by R_{pg} in the AISC *Specification*.
R_h	Hybrid factor, which accounts for early web yielding when the member has a lower yield strength web as compared to the tension and/or compression flange
R_{pc}	Web plastification or cross-section effective shape factor for the compression flange, which accounts for the typical increase in the LTB plateau strength above M_{yc} for noncompact and compact web sections
R_{pt}	Web plastification or cross-section effective shape factor for the tension flange, which accounts for an increase in the tension flange yield strength over M_{yt}
V	Coefficient of variation
V_Q	Coefficient of variation of load effects

V_R	Coefficient of variation of resistance effects
b_{fc}	Width of compression flange
c	Normalized LTB slenderness, equal to $KL_b\sqrt{F_{yc}/E}$)/ r_t; $c = 1$ corresponds to the length L_p in the AASHTO Specifications (2016), whereas $c = 1.1$ corresponds to the length L_p in all cases in the AISC *Specification* (2016), with the exception of doubly-symmetric compact-web members having nonslender (i.e., compact or noncompact) flanges
r_t	Effective radius of gyration for LTB (in), approximated by $r_t = \dfrac{b_{fc}}{\sqrt{12\left(1+\dfrac{1}{3}\dfrac{D_c t_w}{b_{fc} t_{fc}}\right)}}$
r_y	Radius of gyration of a steel I-section with respect to its minor axis
t_{fc}	Thickness of compression flange
t_w	Thickness of web
β	Reliability index
λ_{rw}	Noncompact web slenderness limit
λ_w	Web slenderness ratio

REFERENCES

AASHTO (2016), *AASHTO LRFD Bridge Design Specifications.* 7th Ed., with Interim Revisions, American Association of State Highway and Transportation Officials, Washington, DC.

Adams, P.F., Lay, M.G. and Galambos, T.V. (1964), "Experiments on High Strength Steel Members," Fritz Engineering Laboratory Rep. No. 297.8, Lehigh University, Bethlehem, Pa.

AISC (2005), *Specification for Structural Steel Buildings,* ANSI/AISC 360-05, American Institute of Steel Construction, Chicago, IL.

AISC (2016), *Specification for Structural Steel Buildings,* ANSI/AISC 360-16, American Institute of Steel Construction, Chicago, IL.

Baker, K.A. and Kennedy, D.J.L. (1984), "Resistance Factors for Laterally Unsupported Steel Beams and Biaxially Loaded Steel Beam Columns," *Canadian Journal of Civil Engineering*, Vol. 11, pp. 1008–1019.

Barth, K.E. (1996), "Moment-Rotation Characteristics for Inelastic Design of Steel Bridge Beams and Girders," Doctoral Dissertation, Department of Civil Engineering, Purdue University, West Lafayette, IN.

Bartlett, F.M., Dexter, R.J., Graeser, M.D., Jelinek, J.J., Schmidt, B.J. and Galambos, T.V. (2003), "Updating Standard Shape Material Properties Database for Design and Reliability," *Engineering Journal*, AISC, Vol. 40, No. 1, pp. 2–14.

Basler, K., Yen, B.T., Mueller, J.A. and Thurlimann, B. (1960), "Web Buckling Tests on Welded Plate Girders," *WRC Bulletin No. 64*, Welding Research Council, New York, NY.

Boeraeve, P., Lognard, B., Janss, J., G'erady, J.C. and Schleich, J.B. (1993), "Elasto-Pastic Behavior of Steel Frameworks," *Journal of Constructional Steel Research*, Vol. 27, No. 1-3, pp. 3–21.

CEN (2005), *Design of Steel Structures*, *Part 1-1: General Rules and Rules for Buildings,* EN 1993-1-1:2005:E, Incorporating Corrigendum February 2006, European Committee for Standardization, Brussels, Belgium.

CSA Group (2014), *S16-14—Design of Steel Structures*, Canadian Standards Association, 222 pp.

D'Apice, M.A., Fielding, D.J. and Cooper, P.B. (1966), "Static Tests on Longitudinally Stiffened Plate Girders," *WRC Bulletin No. 117*, Welding Research Council, New York, NY.

Dibley, J.E. (1969). "Lateral Torsional Buckling of I-Sections in Grade 55 Steel," *Proceedings of the Institution of Civil Engineers*, Vol. 43 (August).

Dibley, J.E. (1970), "A Preliminary Investigation into the Use of High Strength Structural Steel in Structures Designed Plastically," BIRSA Open Report EG/A/13/70, British Steel Corporation, London.

Driscoll, G.C. and Beedle, L.S. (1957), "The Plastic Behavior of Structural Members and Frames," *The Welding Journal*, Vol. 36, No. 6, pp. 275s–286s.

Dux, P.F. and Kitipornchai, S. (1983), "Inelastic Beam Buckling Experiments," *Journal of Constructional Steel Research*, Vol. 3, No. 1, pp. 3–9.

Ellingwood, B.E., Galambos, T.V., MacGregor, J.G. and Cornell, C.A. (1980), "Development of a Probability Based Load Criterion for American National Standard A58," *NBS Publication 577*, June, 219 pp.

Ellingwood, B.E., MacGregor, J.G., Galambos, T.V. and Cornell, C.A. (1982), "Probability-Based Load Criteria: Load Factors and Load Combinations," *Journal of the Structural Division,* ASCE, Vol. 108, No. 5, pp. 978–997.

Frost, R.W. and Schilling, C.G. (1964), "Behavior of Hybrid Beams Subjected to Static Loads," *Journal of the Structural Division,* ASCE, Vol. 107, No. ST1, pp. 89–103.

Fukumoto, Y. (1976), Lateral Buckling of Welded Beams and Girders in HT 80 Steel," *Proceedings of the 10th Congress, IABSE*, pp. 403–408.

Fukumoto, Y., Fujiwara, M. and Watanebe, N. (1971), "Inelastic Lateral Buckling Tests on Welded Beams and Girders," *Proceedings of the JSCE,* Vol. 189, pp. 165–181 (in Japanese).

Galambos, T.V. (2004), "Reliability of the Member Stability Criteria in the 2005 AISC Specification," *Steel Structures*, Vol. 4, pp. 223–230.

Galambos, T.V., Ellingwood, B.E., MacGregor, J.G. and Cornell, C.A. (1982), "Probability-Based Load Criteria: Assessment of Current Design Practice," *Journal of the Structural Division,* ASCE, Vol. 108, No. 5, pp. 959–977.

Green, P.S. (2000), "The Inelastic Behavior of Flexural Members Fabricated from High Performance Steel," Doctoral Dissertation, Department of Civil Engineering, Lehigh University, Bethhelem, PA.

Greiner, R. and Kaim, P. (2001), "Comparison of LT-Buckling Design Curves with Test Results," ECCS TC8, Report 23, European Convention for Constructional Steelwork, Brussels, Belgium.

Greiner, R., Salzgeber, G. and Ofner, R. (2001), "New Lateral Torsional Buckling Curves k_{LT}—Numerical Simulations and Design Formulae," ECCS TC8, Report 30, June 2000 (rev), European Convention for Constructional Steelwork, Brussels, Belgium.

Grubb, M.A. and Carskaddan, P.S. (1979), "Autostress Design of Highway Bridges, Phase 3: Initial Moment Rotation Tests," Research Laboratory Report, United States Steel Corporation, Monroeville, PA.

Grubb, M.A. and Carskaddan, P.S. (1981), "Autostress Design of Highway Bridges, Phase 3: Moment Rotation Requirements," Research Laboratory Report, United States Steel Corporation, Monroeville, PA.

Hash, J. B. (2001). "Shear Capacity of Hybrid Steel Girders," Masters Thesis, Department of Civil Engineeeing, University of Nebraska, Nebraska.

Hisamitu, S. and Okuto, K. (1971), "Lateral Buckling Tests on Beams with Residual Stresses," *Preprint*, *Annual Meeting of AIJ*, May (in Japanese).

Holtz, N.M. and Kulak, G.L. (1973), "Web Slenderness Limits for Compact Beams," Structural Engineering Report No. 43, University of Alberta, Alberta, Canada.

Janss, J. and Massonnet, C. (1967), "The Extension of Plastic Design to Steel A52," *Publications of the IABSE*, Vol. 27, pp. 15–30.

Kemp, A.R. (1986), "Factors Affecting the Rotation Capacity of Plastically Designed Members," *The Structural Engineer*, Vol. 64B, No. 2, pp. 28–35.

Kemp, A.R. (1996), "Inelastic Local and Lateral Buckling in Design Codes," *Journal of Structural Engineering,* ASCE, Vol. 122, No. 4, pp. 374–382.

Kim, Y.D. (2010), "Behavior and Design of Metal Building Frames Using General Prismatic and Web-Tapered Steel I-Section Members," Doctoral Dissertation, School of Civil and Environmental Engineering, Georgia Institute of Technology, Atlanta, GA.

Kucukler, M., Gardner, L. and Macorini, L. (2015a), "Lateral-Torsional Buckling Assessment of Steel Beams through a Stiffness Reduction Method," *Journal of Constructional Steel Research*, Vol. 109, pp. 87–100.

Kucukler, M., Gardner, L. and Macorini, L. (2015b), "Flexural-Torsional Buckling Assessment of Steel Beam-Columns through a Stiffness Reduction Method," *Engineering Structures*, Vol. 101, pp. 662–676.

Kusuda, T., Sarubbi, R.G. and Thurliman, B. (1960), "The Spacing of Lateral Bracing in Plastic Design," Fritz Engineering Laboratory Rep. No. 205E.11, Lehigh University, Bethlehem, PA.

Lee, G.C., Ferrara, A.T. and Galambos, T.V. (1964), "Experiments on Braced Wide-Flange Beams," *Welding Research Council Bulletin*, Vol. 99, pp. 1–15.

Lee, G.C. and Galambos, T.V. (1962), "Post-Buckling Strength of Wide-Flange Beams," *Journal of the Engineering Mechanics Division*, ASCE, Vol. 88, No. 1, pp. 59–75.

Lee, S.C. and Yoo, C.H. (1999), "Experimental Study on Ultimate Shear Strength of Web Panels," *Journal of Structural Engineering*, ASCE, Vol. 125, No. 8, pp. 838–846.

Lokhande, A.M. and White, D.W. (2014), "Evaluation of Steel I-Section Beam and Beam-Column Bracing Requirements by Test Simulation," Masters Thesis, School of Civil and Environmental Engineering, Georgia Institute of Technology, Atlanta, GA.

Lukey, A.F., Smith, R.J., Hosain, M.U. and Adams, P.F. (1969), "Experiments on Wide-Flange Beams under Moment Gradient," *WRC Bulletin No. 142*, Welding Research Council, New York, NY.

MacPhedran, I. and Grondin, G.Y. (2009), "A Proposed Simplified Canadian Beam Design Approach," *Proceedings of the Annual Stability Conference*, SSRC, Phoenix, AZ.

MacPhedran, I. and Grondin, G.Y. (2011), "A Simple Steel Beam Design Curve," *Canadian Journal of Civil Engineering*, Vol. 38, pp. 141–153.

McDermott, J.F. (1969), "Plastic Bending of A514 Steel Beams," *Journal of the Structural Division,* ASCE, Vol. 95, No. 9, pp. 1851–1871.

Mikami, I. (1972), "Study on Buckling of Thin Walled Girders Under Bending," Doctoral Dissertation, Department of Civil Engineering, Nagoya University, Japan (in Japanese).

Morikawi, N. and Fujino, S. (1971), "Ultimate Bending Strength of Plate Girders," *Preprint, Annual Meeting of JSCE* (in Japanese).

Nethercot, D.A. and Trahair, N.S. (1976), "Lateral Buckling Approximations for Elastic Beams," *The Structural Engineer*, Vol. 54, No. 6, pp. 197–204.

Nishino, F. and Okumura, T. (1968), "Experimental Investigation of the Strength of Plate Girders in Shear," *Proceedings of the 8th Congress, IABSE*, pp. 451–463.

O'Eachterin, P.O. (1983), "An Experimental Investigation into the Lateral Buckling Strength of Plate Girders," Doctoral Dissertation, Department of Civil and Structural Engineering, University of Sheffield.

Patterson, P.J., Corrodo, J.A., Huang, J.S. and Yen, B.T. (1970), "Fatigue and Static Tests of Two Welded Plate Girders," *WRC Bulletin No. 155*, Welding Research Council, New York, NY.

Prasad, J. and Galambos, T.V. (1963), "The Influence of the Adjacent Spans on the Rotation Capacities of Beams," Fritz Engineering Laboratory Report No. 205H.12, Lehigh University, Bethlehem, PA.

Richter, J.F. (1998), "Flexural Capacity of Slender Web Plate Girders," Masters Thesis, School of Civil, Architectural and Environmental Engineering, The University of Texas at Austin, Austin, TX.

Righman, J. (2005), "Rotation Compatibility Approach to Moment Redistribution for Design and Rating of Steel I-Girders," Doctoral Dissertation, School of Civil Engineering, West Virginia University, Morgantown, West Virginia.

Rockey, K.C. and Skaloud, M. (1972), "The Ultimate Load Behavior of Plate Girders Loaded in Shear," *The Structural Engineer*, Vol. 50, No. 1, pp. 29–47.

Sakai, F., Doi, K., Nishino, F. and Okumura, T. (1966), "Failure Tests of Plate Girders Using Large Sized Models," Structural Engineering Report, Department of Civil Engineering, University of Tokyo, Tokyo, Japan.

Salem, E.S. and Sause, R. (2004), "Flexural Strength and Ductility of Highway Bridge I-Girders Fabricated from HPS-100W Steel," ATLSS Report No. 04-12.

Salvadori, M.G. (1955), "Lateral Buckling of I-Beams," *ASCE Transactions*, Vol. 120, pp. 1165–1177.

Sawyer, H.A. (1961), "Post-Elastic Behavior of Wide-Flange Steel Beams," *Journal of the Structural Division,* ASCE, Vol. 87, No. ST8, pp. 43–71.

Schilling, C.G. and Morcos, S.S. (1988), "Moment Rotation Tests on Steel Girders with Ultracompact Flanges," Report on Project 188, American Iron and Steel Institute, Washington, DC.

Schuller, W. and Ostapenko, A. (1970), "Tests on a Transversely Stiffened and on a Longitudinally Stiffened Unsymmetrical Plate Girder," *WRC Bulletin No. 156*, Welding Research Council, New York, NY.

Standards Association of Australia (SAA) (1998), "Steel Structures," AS4100-1998, Australian Institute of Steel Construction, Sydney, Australia.

Subramanian, L.P. (2015), "Flexural Resistance of Longitudinally Stiffened Plate Girders," Doctoral Dissertation, School of Civil and Environmental Engineering, Georgia Institute of Technology, Atlanta, GA.

Subramanian, L.P. and White, D.W. (2017a), "Resolving the Disconnect between Lateral Torsional Buckling Experimental Tests, Test Simulations, and Design Strength Equations," *Journal of Constructional Steel Research*, Vol. 128, pp. 331–334.

Subramanian, L.P. and White, D.W. (2017b), "Reassessment of the Lateral Torsional Buckling Resistance of I-Section Members: Uniform-Moment Studies," *Journal of Structural Engineering*, ASCE, Vol. 143, No. 3, Published Online: October 2016.

Subramanian, L.P. and White, D.W. (2017c), "Reassessment of the Lateral Torsional Buckling Resistance of Rolled I-Section Members: Moment Gradient Tests," *Journal of Structural Engineering*, ASCE, Vol. 143, No. 4, Published Online: October 2016.

Subramanian, L.P. and White, D.W. (2017d), "Improved Noncompact Web Slenderness Limit for Steel I-Girders," *Journal of Structural Engineering*, ASCE, Vol. 143, No. 4, Published Online: November 2016.

Suzuki, T. and Kubodera, M. (1973), "Inelastic Lateral Buckling of Steel Beams," *Preprint, Annual Meeting of AIJ* (in Japanese).

Suzuki, T. and Ono, T. (1970), "Experimental Study of Inelastic Beams (1)—Beam Under Uniform Moment," *Transactions of the Architectural Institute of Japan*, Vol. 45, No. 168, pp. 77–84 (in Japanese).

Suzuki, T. and Ono, T. (1973), "Inelastic Lateral Buckling of Steel Beams," *Preprint, Annual Meeting of AIJ* (in Japanese).

Suzuki, T. and Ono, T. (1976), "Deformation Capacity of High-Strength Steel Members," *Proceedings, Preliminary Report, 10th Congress IABSE*.

Toğay, O., Jeong, W.Y. and White, D.W. (2016), "Load Height Effects on Lateral Torsional Buckling of I-Section Members—Design Estimates, Inelastic Buckling Calculations and Experimental Results," Structural Engineering, Mechanics and Materials Report No. 111, School of Civil and Environmental Engineering, Georgia Institute of Technology, Atlanta, GA.

Trahair, N. and Hancock, G. (2004), "Steel Member Strength by Inelastic Lateral Buckling," *Journal of Structural Engineering*, ASCE, Vol. 130, No. 1, pp. 64–69.

Udagawa, K., Saisho, M., Takanashi, K. and Tanaka, H. (1973), "Experiments on Lateral Buckling of H-Shaped Beams Subjected to Monotonic Loadings," *Transactions of the Architectural Institute of Japan*, Vol. 48, No. 212, pp. 23–33.

Wakabayashi, M., Nakamura, T. and Okamura, N. (1970), "Studies on Lateral Buckling of Wide Flange Beams (1)," *Disaster Prevention Research Institute Annals*, Vol. 14A, Kyoto University, Kyoto, Japan (in Japanese).

White, D.W. (2008), "Unified Flexural Resistance Equations for Stability Design of Steel I-Section Members: Overview," *Journal of Structural Engineering*, ASCE, Vol. 134, No. 9, pp. 1405–1424.

White, D.W., Barker, M. and Azizinamini, A. (2008), "Shear Strength and Moment-Shear Interaction in Transversely-Stiffened Steel I-Girders," *Journal of Structural Engineering,* ASCE, Vol. 134, No. 9, pp. 1437–1449.

White, D.W., Jeong, W.Y. and Toğay, O. (2016a), "Comprehensive Stability Design of Steel Members and Systems via Inelastic Buckling Analysis," *International Journal of Steel Structures*, Vol. 16, No. 4, pp. 1029–1042.

White, D.W., Jeong, W.Y. and Toğay, O. (2016b), SABRE2, white.ce.gatech.edu/sabre (August 15, 2016).

White, D.W. and Jung, S.-K. (2004), "Unified Flexural Resistance Equations for Stability Design of Steel I-Section Members—Uniform Bending Tests," Structural Engineering, Mechanics and Materials Report No. 28, School of Civil and Environmental Engineering, Georgia Institute of Technology, Atlanta, GA, 128 pp.

White, D.W. and Jung, S.-K. (2008), "Unified Flexural Resistance Equations for Stability Design of Steel I-Section Members: Uniform Bending Tests," *Journal of Structural Engineering*, ASCE, Vol. 134, No. 9, pp. 1450–1470.

White, D.W. and Kim, Y.D. (2004), "Unified Flexural Resistance Equations for Stability Design of Steel I-Section Members—Moment Gradient Tests," Structural Engineering, Mechanics and Materials Report No. 04-29, School of Civil and Environmental Engineering, Georgia Institute of Technology, Atlanta, GA, 149 pp.

White, D.W. and Kim, Y.D. (2008), "Unified Flexural Resistance Equations for Stability Design of Steel I-Section Members: Moment Gradient Tests," *Journal of Structural Engineering*, Vol. 134, No. 9, pp. 1471–1486.

Wong-Chung, A.D. and Kitipornchai, S. (1987), "Partially Braced Inelastic Beam Buckling Experiments," *Journal of Constructional Steel Research*, Vol. 7, No. 3, pp. 189–211.

Yakel, A.J., Mans, P. and Azizinamini, A. (1999), "Flexural Capacity of HPS-70W Bridge Girders," NaBRO Report, University of Nebraska, Lincoln, NE.

Yura, J.A., Galambos, T.V. and Ravindra, M.K. (1978), "The Bending Resistance of Steel Beams," *Journal of the Structural Division,* ASCE, Vol. 104, No. ST9, pp. 1355–1370.

Ziemian, R.D. (2010), *Guide to Stability Design Criteria for Metal Structures*, Structural Stability Research Council, 6th Ed., Wiley.

Cyclic Inelastic In-Plane Flexural Behavior of Concrete-Filled, Sandwich Steel Panel Walls with Different Cross-Section Properties

ERKAN POLAT and MICHEL BRUNEAU

ABSTRACT

Flexure-dominated, concrete-filled, sandwich steel plate walls (CFSSP-Walls) walls have been studied experimentally by various researchers using a small number of cross-sections and wall aspect ratios. Using these past results to calibrate finite element models, the expected behavior of CFSSP-Walls having different geometries and cross-section properties is investigated here using finite element approaches. Results obtained show that the plastic moment can be used to conservatively predict maximum flexural strength in all cases considered and to provide valuable insights into stress and strain demands at various points during nonlinear response. Results also provide quantification of the contribution of concrete infill on the wall effective stiffness, assessment of wall ductility having a failure criteria based on cumulative plastic strain at steel plate fracture, and effect of wall flange width on the wall behavior of T-shaped sections.

Keyword: steel plate walls, CFSSP, effective stiffness, plate fracture.

INTRODUCTION

Concrete-filled, sandwich steel panel walls (CFSSP-Walls) have been the subject of extensive research in recent years, with an emphasis on their potential application in nuclear power plants or high rises (e.g., Oduyemi and Wright, 1989; Wright et al., 1991a, 1991b; Xie and Chapman, 2006; Eom et al., 2009; Ramesh, 2013; Zhang et al., 2014; Sener and Varma, 2014; Varma et al., 2014; Epackachi et al., 2014; Sener et al., 2015; Epackachi et al., 2015; Booth et al., 2015; Kurt et al., 2016; Seo et al., 2016; Alzeni and Bruneau, 2017; Polat and Bruneau, 2017). Referred to as "composite plate shear walls—concrete filled (C-PSW/CF) by the AISC *Seismic Provisions* (AISC, 2016), and steel concrete (SC) walls in some of the above-cited publications, these walls consist of dual-steel-plate "sandwiching" a concrete infill. Their appeal over traditional reinforced concrete walls mainly lies in their rapid site construction (because the steel plates can provide temporary formwork and can resist alone some of the construction loads), their high composite strength, and their smaller thickness (resulting in greater leasable floor space in high-rise applications). Experimental research has demonstrated that CFSSP-Walls can be highly ductile in flexure (e.g., Eom et al., 2009; Alzeni and Bruneau, 2014), as long as the ties that connect the steel plates are properly designed (Bowerman et al., 1999; Ramesh, 2013) and plate buckling only occurs after development of the plastic moment.

Design requirements for CFSSP-Walls specified by the AISC *Seismic Provisions* (AISC, 2016) are based on results from a limited number of tests, largely conducted on planar walls and for a small number of cross-section aspect ratios. While further testing is desirable, and anticipated to occur in the future, finite element analysis can be used to investigate the expected behavior of other CFSSP-Wall configurations and aspect ratios and to determine if satisfactory behavior is also obtained in these other cases, possibly providing enhanced confidence over a broader range of applicability. This can be done as long as the finite element models used for this purpose have been developed and calibrated against prior CFSSP-Wall experimental results. Such development and calibration has been done by Polat and Bruneau (2017), using experimental results from Alzeni and Bruneau (2014, 2017). The finite element models developed in that study were able to replicate the cyclic inelastic in-plane flexural behavior of the CFSSP-Wall up to failure and to capture the mechanisms that control this behavior (namely, in this case, steel yielding and strain hardening, concrete cracking and confinement, global strength and stiffness degradation, plastic local buckling, pinching of the hysteresis loops, and cumulative-plastic strains prior to fracture). In the process, suitable material models, element types, element sizes, and

Erkan Polat, Ph.D., Department of Civil, Structural and Environmental Engineering, University at Buffalo, State University of New York, Buffalo, NY. E-mail: erkanpol@buffalo.edu (corresponding)

Michel Bruneau, Professor, Department of Civil, Structural and Environmental Engineering, University at Buffalo, State University of New York, Buffalo, NY.

Table 1. Cross-Sectional Properties of the CFSSP-Walls						
Wall Designation	W, in.	b, in.	t_s, in.	t_c, in.	S, in.	d_{in}, in.
CFSSP-B1	44	30	5⁄16	6	8	8
CFSSP-B2	44	30	5⁄16	6	12	8
CFSSP-NB1	48.625	40	5⁄16	8	8	8
CFSSP-NB2	48.625	40	5⁄16	8	12	8

contact models were identified. This study also accounted for the flexibility induced by the footing at the wall base (as part of the test set-up) by explicitly modeling it. Furthermore, it was demonstrated (Polat and Bruneau, 2017; Alzeni and Bruneau, 2014, 2017) that the ultimate flexural strength of these planar walls can be conservatively predicted by equations based on simple plastic theory that assume uniform steel yield strength, F_y, and uniform compressive concrete strength. f'_c.

Here, using the finite element model developed and validated by Polat and Bruneau (2017), a number of CFSSP-Walls having different cross-section properties are investigated. For this purpose, analysis of the CFSSP-Walls experimentally tested by Alzeni and Bruneau, but without their footing, was first conducted to establish a basis for all comparisons; this was done because only fixed-base walls results are of interest here (i.e., to ensure that only wall behavior is compared here because the footings were only needed for experimental purposes and differ from how wall-base connection would be accomplished in actual applications). Analysis results from these fixed-base wall models are also used to predict the contribution of infill concrete on the wall effective lateral stiffness. Then presented are the results from a parametric study considering many cross-section aspect ratios and properties, conducted to assess the adequacy of the simple plastic moment equations to predict the results obtained from the finite element models. Finally, the finite element model is used to investigate the behavior of a T-shaped CFSSP-Wall tested by Eom et al. (2009), and a modified version of that wall having a much wider flange.

Note that while much research has also been conducted on shear (or shear-flexure) in-plane behavior of CFSSP-Walls having low aspect ratio ranging from 0.6 to 1.0 (Varma et al., 2014; Zhang et al., 2014; Epackachi et al., 2015, Kurt et al., 2016; Seo et al., 2016), the focus here is on flexure-dominated CFSSP-Walls that are expected to yield in flexure because this is the case in high-rise applications.

CFSSP-WALLS AND FINITE ELEMENT MODELING

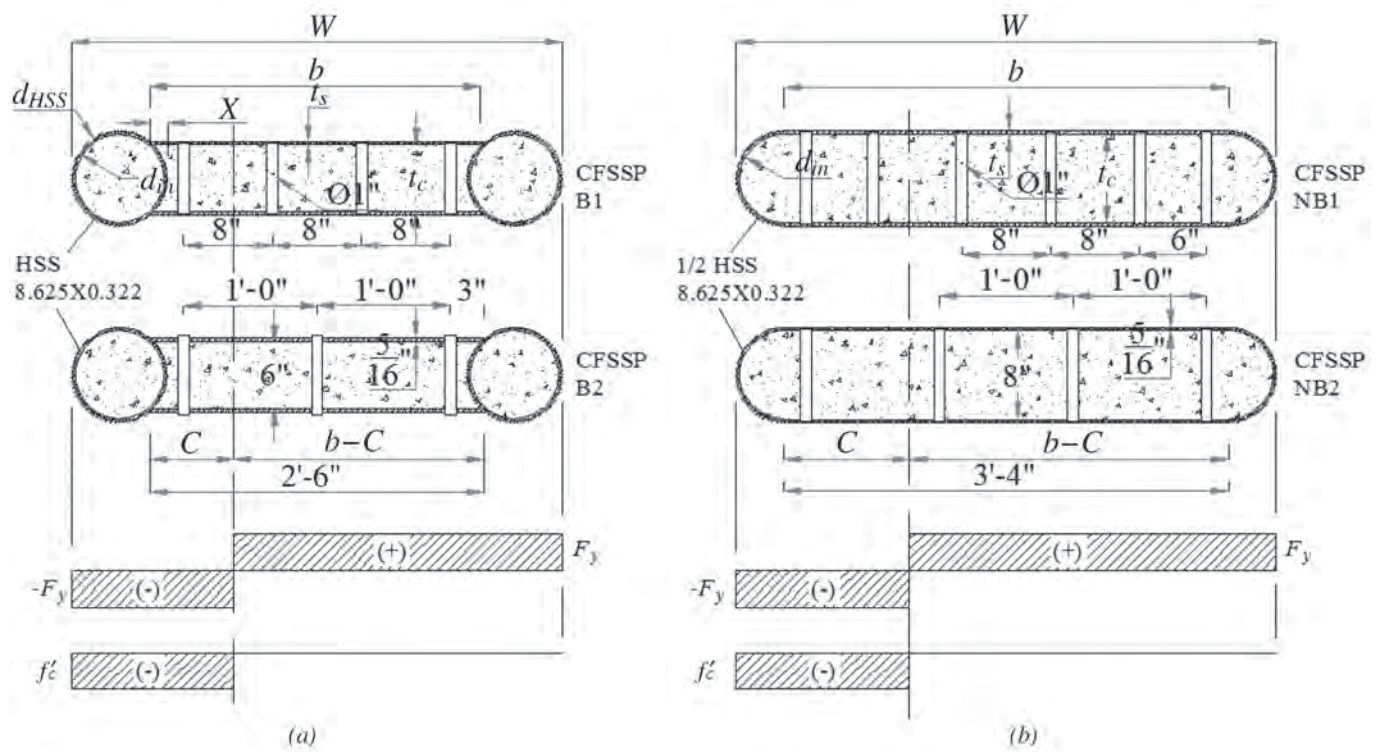Figure 1 illustrates the cross-section of the CFSSP-Walls tested by Alzeni and Bruneau (2014, 2017) and used by Polat and Bruneau (2017) to develop and calibrate the finite element model; it also shows the plastic stress distributions and closed-form equations (provided in AISC *Seismic Provisions* Eqs. C-H7-2 through C-H7-6), used to calculate the plastic flexural strength, M_p, of the walls. Table 1 presents the values of the parameters that define the cross-sections shown in Figure 1. Note that tie spacing, S, of these walls was selected based on AISC *Seismic Provisions* Equation H7-1 ($S = 1.8t_s\sqrt{E/F_y}$) to ensure steel plate yielding before plate buckling. These walls were (and will be) referred as B1, B2 (group B) and NB1, NB2 (group NB) as shown in Figure 1. Note that the ends of group B walls consisted of round HSS columns, whereas half-round HSS columns were used for group NB walls. The walls were cantilever type, and the height of the specimens above the footing was 120 in.

The finite element study of the walls was performed using LS-Dyna (LSTC, 2015). Following is a brief description of the element types, material models, and contact models used in the finite element analyses performed by Polat and Bruneau (2017). Note that the work presented here (for the parametric study of CFSSP-Walls and for the study on T-shaped walls) follows the same modeling approach.

The concrete infill was modeled using an eight-node, constant stress solid element (*solid 1*) with reduced integration and the *Winfrith_concrete* model (Material 084/085 in LS-Dyna). The size of the solid elements was 1×1×1 in. The steel sandwich panels and HSS were modeled using four-node, fully integrated shell elements (*shell 16*) with Belytschko-Tsay shell formulation with three integration points through thickness and the *plastic_kinematic* (Material 3 in LS-Dyna) bi-linear material model with kinematic hardening. The shell elements were 1×1 in. and had the thickness of steel panels. The ties that extend between the dual plates (needed to develop composite action and transfer shear forces along the steel-concrete interface) were modeled using two-node beam elements (*beam 1*) with Hughes-Liu beam formulation with two integration points and the *plastic_kinematic* material model. Note that the average uniaxial tension coupon test data reported in Alzeni and Bruneau (2014) were used for the steel material model properties, and the average uniaxial compression test data were used for the concrete material model properties. As reported in Polat and Bruneau (2017), the elastic modulus used in

the simulations was 29,800 ksi (205,463 MPa) for the steel web and 27,500 ksi (189,605 MPa) for the HSS. For the web plate (WP) and HSS, as far as the other bi-linear steel model parameters were concerned, Fy_{WP} of 62 (427), 64 (441), 61 (420), and 63 ksi (434 MPa); E_{T_WP} of 100 (689), 100 (689), 80 (551), and 110 ksi (758 MPa); $Fy_{\_HSS}$ of 56 (386), 56 (386), 52 (358), and 51 ksi (351 MPa); and E_{T_HSS} of 80 (551), 60 (413), 50 (344), and 50 ksi (344 MPa) were used for the models B1, B2, NB1, and NB2, respectively, where Fy is the yield strength and E_T is the tangent modulus after yielding. Similarly, the average concrete compressive strengths were 7.1 (50), 4.8 (33), 6.9 (47), and 6.8 ksi (47 MPa) for B1, B2, NB1, and NB2.

The interaction between the steel sandwich panels and the infill concrete was defined using the *automatic_ surface_to_surface_mortar* contact model with static interface friction coefficient of 0.3 and increased contact stiffness [the work substantiating the choice of this contact model is presented in Polat and Bruneau (2017)]. The displacement controlled drift reversals were modeled with a single cycle per drift amplitude, as opposed to the multiple cycles per drift amplitude in the actual tests. In the numerical simulation, displacement histories with user-defined time steps was used to apply the displacement history; this was done to define the time intervals of the numerical integration for the implicit solution procedure in the program and to expedite

Fig. 1. Cross-sectional dimensions of CFSSP-Walls, stress blocks, and closed-form solutions used to calculate plastic flexural strength, M_p, of CFSSP-Walls: (a) group B walls; (b) group NB walls (Polat and Bruneau, 2017).

simulation run time and increase convergence, as defined in Polat and Bruneau (2017).

The implementation of the steel material model (material 3) in LS-Dyna is based on the formulation by Kreig and Key (1976) (see also Hallquist, 2006). In this material model, the yield criteria is based on the von Mises (also known as effective stress) interaction of stresses. The definition of effective stress and effective plastic strain (in tensorial notation) is given by the following equations:

$$\sigma_{VM} = \frac{1}{\sqrt{2}} \left[(\sigma_x - \sigma_y)^2 + (\sigma_y - \sigma_z)^2 + (\sigma_z - \sigma_x)^2 + \right.$$
$$\left. 6(\sigma_{xy}^2 + \sigma_{yz}^2 + \sigma_{zx}^2) \right]^{\frac{1}{2}} \tag{1}$$

$$\varepsilon_{eff}^p = \int_0^t \left[2/3 \left(\dot{\varepsilon}_{ij}^p \dot{\varepsilon}_{ij}^p \right) \right]^{\frac{1}{2}} dt \tag{2}$$

where σ_x, σ_y, σ_z are normal stresses; σ_{xy}, σ_{yz}, σ_{zx} are shear stresses in a three-dimensional continuum body; and $\dot{\varepsilon}_{ij}^p$ is the plastic component of the rate of deformation tensor. The effective plastic strain (grows whenever the material is actively yielding) was used in this study to determine the initiation and propagation of the fracture critical region of the steel section.

Note that the Winfrith concrete model in LS-Dyna (material 85) considers smeared cracking and has a crack formulation (Wittmann et al., 1988) that considers aggregate size, concrete compressive strengths, loading rates, cement-to-water ratios, and test specimen size (Schwer, 2011). The material model is capable of simulating the opening and closing of the concrete cracks under tensile and compressive stresses, respectively, which is essential to capture the pinching effect observed in the wall's hysteresis curves, as effectively demonstrated by Goto et al. (2010) and Imani and Bruneau (2014) for concrete-filled steel tube columns. Schwer (2011) explains the plasticity models, the strain rate formulation, and tensile cracking options of this material model. Note that the Winfrith concrete model has also been used by Epackachi et al. (2015) and Kurt et al. (2015) in the simulation of SC composite shear walls with aspect ratios of 0.6 to 1.0.

FINITE ELEMENT ANALYSES OF FIXED-BASE CFSSP-WALL MODELS

Analyses of the CFSSP-Walls, including foundation flexibility by Polat and Bruneau (2017), showed that the force distribution inside the wall footing is rather complex. Explicit modeling of the wall footing introduced flexibility at the wall base due to its deformation under shear and moment forces from the embedded part of the wall under wall deformation. Base flexibility may alter the wall response in a number of ways, the ultimate drift ratio at failure of wall is increased due to additional drift that stems from the base rotation introduced within the footing, and steel plate buckling likewise occurs at larger drifts due to reduced axial strains at a
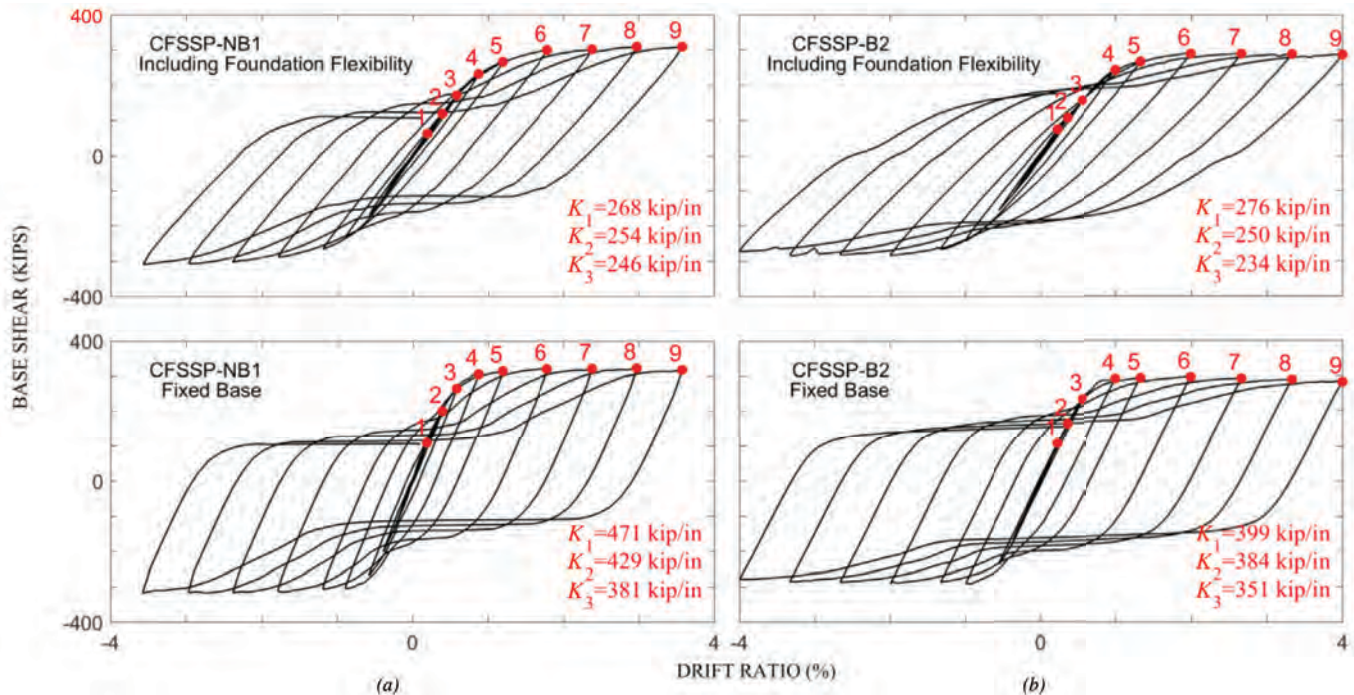

Fig. 2. Comparison of initial wall stiffness of LS-Dyna models with and without foundation flexibility: (a) CFSSP-NB1; (b) CFSSP-B2.

particular drift. Wall displacement ductility (given by the ratio between ultimate wall drift and yield drift) may also be effected, to a lesser degree.

To illustrate the effect of foundation flexibility on the wall response, Figure 2 shows a comparison of hysteretic curves of selected CFSSP-Walls (NB1 and B2) analyzed with and without their foundation. [Note that comparisons for the wall models NB2 and B1 were not included due to space concerns; however, model B2 was intentionally chosen because this model was also used by Polat and Bruneau (2017) to obtain effective plastic strain values for steel plate fracture for specimen with flexible foundation; similar work is also performed here, but for the fixed-base model of B2.] Initial wall stiffnesses from each curve are reported using secant stiffness values at the first three peak positive-drift locations shown in the figures (peak positive drift locations are denoted with numbers from 1 to 9). Stiffness values

(shown on the figures) indicate that fixed-base models are approximately 1.4 to 1.80 times stiffer than their counterpart with base flexibility.

To compare the effect of wall stiffness on the axial strain demand, Figure 3 shows the lateral force versus axial strain hysteresis of these walls obtained from the outermost steel element at the wall base. This demonstrates that axial strain amplitudes of the fixed-base model are much larger than those of the model with foundation flexibility at the same drift amplitude. Note that for the fixed-base wall models of the CFSSP-NB1 and B2 walls, steel plate local buckling develops at a drift amplitude of 1.20 and 1.33%, respectively [whereas it was 1.80 and 2.00% for the same walls with base flexibility, as shown in Polat and Bruneau (2017)]. The tensile-axial-strains of these models at the onset of steel plate buckling were 0.024 in./in. and 0.031 in./in., respectively, for CFSSP NB1 ($S/t_s = 25.6$) and B2 ($S/t_s = 38.4$).
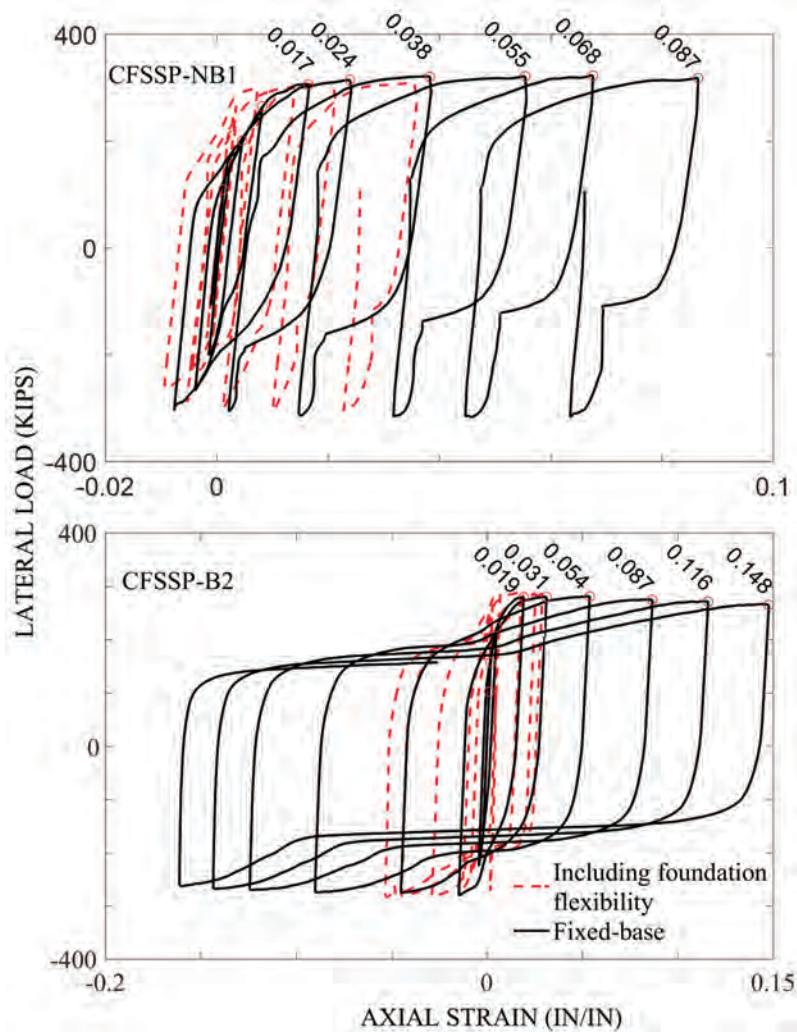

Fig. 3. Comparison of lateral load versus steel strain relationships for CFSSP-NB1 for fixed base and including foundation flexibility.

Figures 4 and 5 show the lateral force–drift ratio hysteresis of the fixed-base models for the group B and NB specimens, including relative contributions of the steel and concrete components of the cross-section to the total hysteretic curves. The base shear (denoted as V_p) at which the walls attain their plastic flexural strength (see Figure 1 for M_p), is also shown ($V_p = M_p/H$, where M_p is based on simple plastic theory and H is the wall height). Figures 4 and 5 reveal that the steel section accounts for about 80% of the wall strength, which is consistent with the design values recommended by Alzeni and Bruneau (2014). These figures also indicate a reduction of the flexural strength of steel skin as a result of steel plate buckling after about 1.0% drift ratio. [Note that the experimental measurement and findings of the CFSSP-Walls reported in Alzeni and Bruneau (2014, 2017) showed that some minor strength degradation occurred post-buckling; the main strength degradation of the specimens mostly occurred following steel plate fracture. Modeling of steel plate fracture in an explicit manner is a complex issue to be investigated in future research.] The reduction of steel flexural strength, due to steel plate buckling, is more severe for the group NB wall models (~45% reduction for NB1 and ~60% for NB2) than for the group B wall models (~20% reduction for B1 and ~30% for B2). Note that while Polat and Bruneau (2017) provide stress distribution plots for the

CFSSP-Walls considering foundation flexibility to match that of the specimens tested, such plots are not provided here for the fixed-base walls considered in this paper due to space limitations. However, the stress distribution of the planar CFSSP-Walls [provided in Polat and Bruneau (2017)] does not indicate concrete crushing (which is defined to occur when both degradation in the strength contributed by concrete and reduction in maximum concrete stresses occur simultaneously), which is consistent with the CFSSP-Wall hysteresis shown in Figures 4 and 5.

Note that the lateral force-drift hysteresis of concrete shows that stiffness and strength contribution of concrete is delayed under subsequent drift amplitudes, following the drift amplitude of 1.0%. This is a result of the opening and closing of the horizontal tensile cracks forming in concrete under reversed cyclic drifts and the development of higher crack widths or formation of new cracks along the uncrack region of the concrete under increased drift amplitudes, which can be explained as follows. Under cyclic loading, in a given displacement direction, residual tensile strains develop in the steel skin, which results in elongations in the steel section and horizontal tensile cracking in the infill concrete. Under reversal of displacements, while the steel section that has residual tensile strains can still resist compressive stresses as well as shear stresses, the cracked
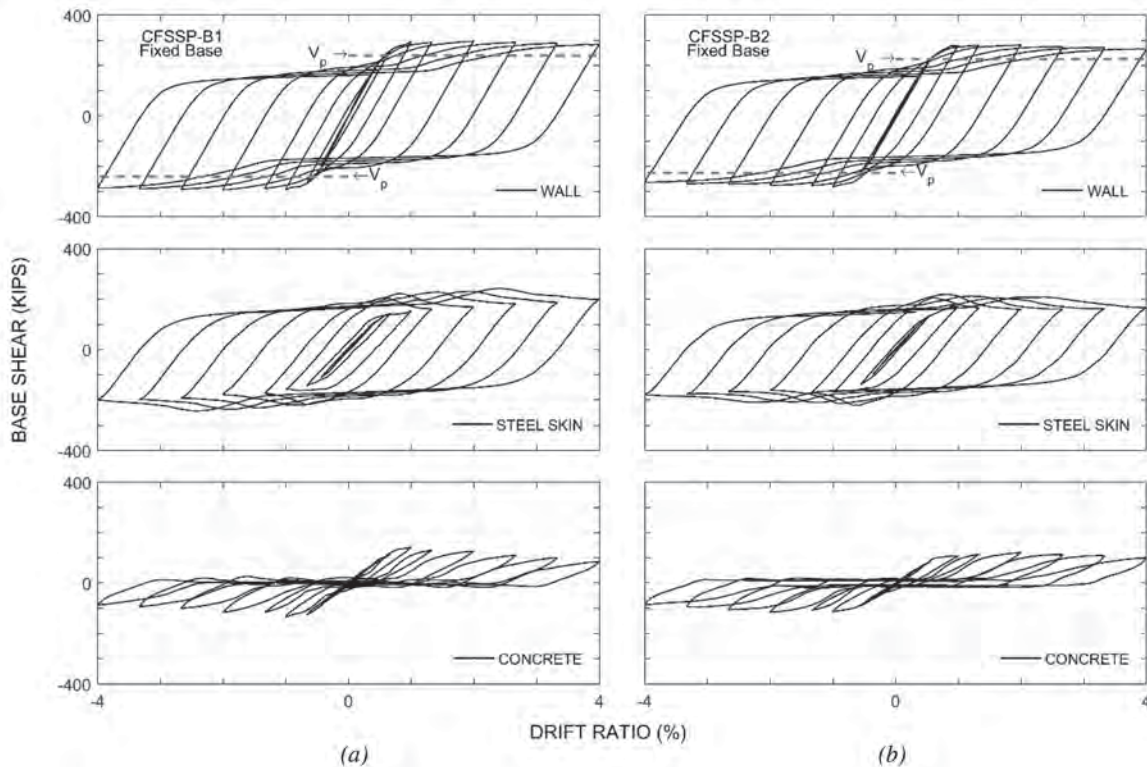

Fig. 4. Hysteresis curves of the LS-Dyna model for group B walls: (a) CFSSP-B1; (b) CFSSP-B2.

concrete does not resist any normal and shear stresses until the tensile cracks are closed. During the opening and closing of the horizontal tensile cracking, shear resistance is mainly provided by the steel section of the wall, while limited contribution comes from the concrete section. The relative contribution of concrete increases with closure of the horizontal tensile cracks following the development of steel plate buckling.

Contribution of Concrete to Equivalent Effective Stiffness of CFSSP-Walls

Equivalent effective stiffness is typically represented as the sum of the stiffness contributions from the steel and concrete as given by Equation 3 (AISC, 2016). In Equation 3, I_S and I_C are the gross moment of inertia of the steel and concrete parts of the CFSSP-Wall cross-section, respectively. C_3 is a reduction factor accounting for the cracking of concrete.

$$EI_{eff} = E_S I_S + C_3 E_C I_C \qquad (3)$$

Alzeni and Bruneau (2014) recommended a C_3 factor of 0.4 based on results of finite element analyses conducted using ABAQUS (SIMULIA, 2012). Although, those models were calibrated based on flexural test results, Polat and Bruneau (2017) showed that better results could be obtained using the Winfrith concrete model (available in LS-Dyna, not in ABAQUS, at the time of this writing), compared to those obtained using the concrete damage plasticity model in ABAQUS (Hibbett et al., 1998), particularly when it came to replicate pinching of the hysteresis loops and peak strength at each cycle of loading.

The availability of finite element results, using a model calibrated on the experimental results and then equivalently converted into a fixed-base model, makes it possible to assess the value of C_3 in Equation 3 for this structural system. Assuming the wall acting as a cantilever beam, with a tip lateral deflection of $\Delta = PL^3/3EI$ (for a beam length L, flexural rigidity EI, and unit load P at the tip), C_3 can be calculated using the stiffness values obtained from the finite element analyses results by replacing EI in the equation with EI_{eff}. In this calculation, the effective flexural rigidity of the LS-Dyna models, EI_{eff}, the peak displacement, Δ, and the corresponding load, P, at the first loading cycle were used. The calculated EI_{eff} and corresponding C_3 values for each CFSSP-Walls are given in Table 2. The values for C_3 are between 0.30 and 0.45 and are in relative agreement with that recommended ($C_3 = 0.4$) by Alzeni and Bruneau (2014).
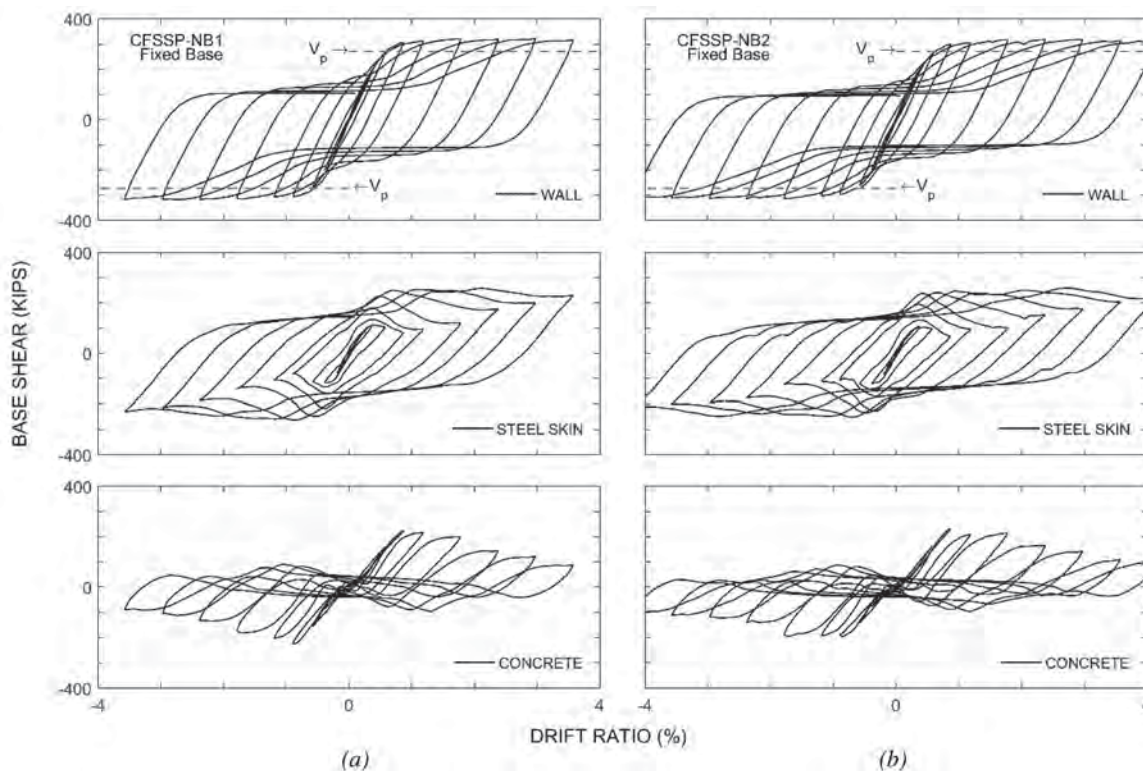

Fig. 5. Hysteresis curves of the LS-Dyna models for group NB walls: (a) CFSSP-NB1; (b) CFSSP-NB2.

Table 2. C_3 Values for Each of the LS-Dyna Models for CFSSP-Walls		
CFSSP-Wall	**EI_{eff}**	**C_3, FE Model**
CFSSP-NB1	271447306	0.37
CFSSP-NB2	261590952	0.31
CFSSP-B1	232520184	0.44
CFSSP-B2	232018928	0.43

Yielding and Prediction of Failure Drift Ratio for a Fixed-Base CFSSP-Wall

As noted before, the steel plates yielding was modeled using the von Mises yield criteria, which is a combination of three-dimensional normal and shear stresses. Polat and Bruneau (2017) showed that the uniaxial yield strength of the steel skin at the wall boundaries is increased under tension and decreased under compression (as a result of the von Mises' relationship describing interaction between stresses on the yield surface).

Furthermore, although the numerical models do not consider material damage within their hysteretic formulations, a failure criteria can be established for the steel material model by setting a failure cumulative plastic strain limit, such that if this value is exceeded, elements using this material model are eroded. Polat and Bruneau (2017) determined this limit by correlating finite element and experimental results at drift when fracture was observed to occur the for CFSSP-B2 wall. Figures 6 and 7 show the von Mises stress and plastic strain contours of the bottom one-third of the steel skin of the B2 and NB1 wall models, which illustrates yielding and damage-prone regions of the steel skin across the wall base. Figures 6b and 7b show that effective plastic strains are higher in regions where local buckling of steel skin takes place. Therefore, cumulative plastic strain histories obtained from the failure critical element of this buckling region of the steel skin were used to predict the failure drift ratio of the fixed base wall model of CFSSP-B2.

Polat and Bruneau (2017) reported effective plastic strain histories of the fracture critical element for the CFSSP-B2 model with base flexibility. The failure strain values for the finite element model, corrected to correspond to the plastic strain values for the actual specimens subjected to more cycles than the finite element models, were obtained by calculating the plastic strain values at the drift where steel skin fracture was observed to initiate in the actual specimen. The reported plastic strain was 1.40–1.45 from the numerical model under single-cycle loading, and the corrected cumulative plastic strain value for the actual specimen was 2.60 under multiple-cycle loading per drift level. Using the corrected plastic strain for the actual specimen, failure drift of the fixed-base numerical model was determined. Table 3 presents the history of the cumulative plastic strain values of the fracture critical element of the numerical model at various drifts. From the table, the drift level at which this element attain the failure strain is found to be 3.33%.
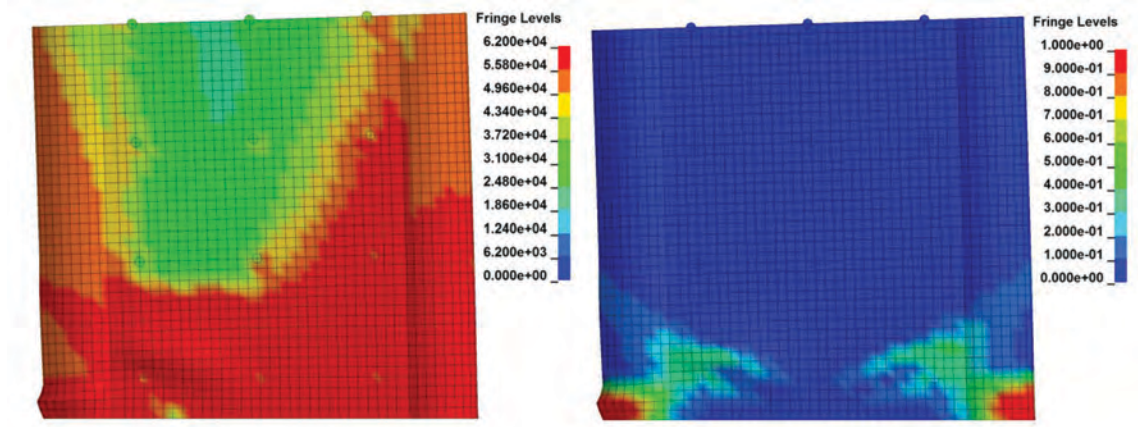

Fig. 6. Von Mises yield stress (a) and effective plastic strain (b) contours of the LS-Dyna model for CFSSP-B2 at 3.33% drift.

Table 3. Effective Plastic Strain Values for the Fixed-Base CFSSP-B2 Wall Model (failure strain defined by ΣPS)						
Drift Ratio (%)	Cycle Order (i)	Cycle for Each Drift (n)	Cumulative Plastic Strain (PS) LS-Dyna (single cycle)	$PS_{i+1} - PS_i$	$n \times$ $PS_{i+1} - PS_i$	$\Sigma n \times$ $(PS_{i+1} - PS_i)$
0.23	1	3	0	0	0	0
0.36	2	3	0.0002	0.0002	0.0006	0.0006
0.56	3	3	0.0042	0.004	0.012	0.0126
1.00	4	3	0.0281	0.0239	0.0717	0.0843
1.33	5	3	0.1134	0.0853	0.2559	0.3402
2.00	6	2	0.318	0.2046	0.4092	0.7494
2.67	7	2	0.7432	0.4252	0.8504	1.5998
—	—	*1.5*	*1.4168*	*0.6736*	*1.0104*	*2.6102*
3.33	8	2	1.4168	0.6736	1.3472	3.9574
						$\Sigma PS = 2.61$

PARAMETRIC STUDY

Finite element analysis was then conducted, using the preceding models, to investigate the possible in-plane behavior of wall configurations similar to the tested CFSSP-NB (i.e., without full HSS boundary elements) but having cross-section geometries different than those considered in the experimental program conducted by Alzeni and Bruneau (2014). The scope of the parametric study was limited to only cover the following aspects:

1. The D/t_s ratio, which is the ratio between the diameter of the HSS part of the cross-section and its thickness, taken as $0.076\ E/F_y$ in addition to the value of $0.044E/F_y$ used in the experiments.

2. The S/t_s ratio, which is the ratio between the tie-bars spacing and the thickness of the skin plate, taken as an arbitrary value of 50 here in addition to the S/t_s ratio of 25.6 and 38.4 used in the experiments.

3. The t_c/b ratio, which is the ratio between the thickness of the concrete and the length of the steel web, with values of 0.1, 0.4, 0.57 and 0.80 considered in addition to 0.2 used in the tested CFSSP-NB wall.

Figure 8 illustrates the cross-section of the walls considered in this parametric study. Table 4 provides the corresponding values for the wall dimensions. Note that to keep the wall aspect ratio similar to the original wall tested (~2.50), the walls with reduced plate widths were reduced in height (i.e., with a wall height of 70 in. for NB-0.4b, 55 in. for NB-0.57b, and 45 in. for NB-0.8b).

Figure 9 shows the lateral load–drift hysteresis of these walls, including the relative contributions from the steel skin
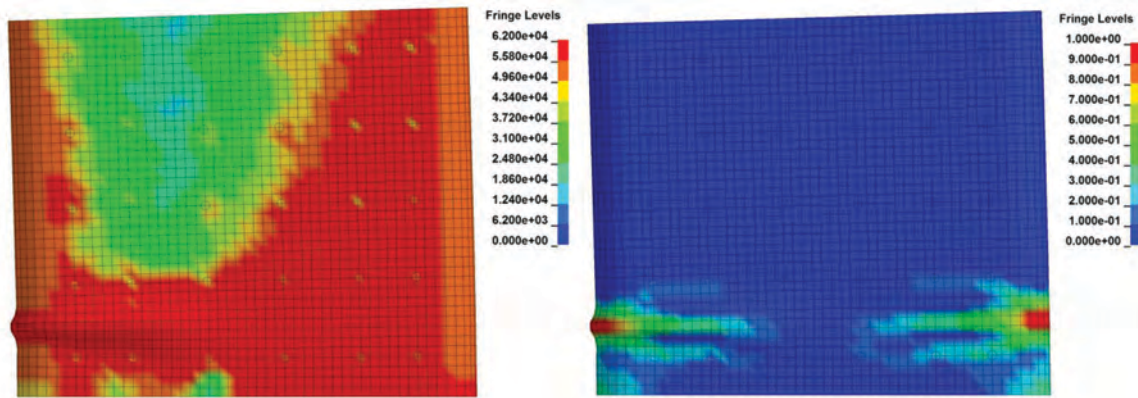

Fig. 7. Von Mises yield stress (a) and effective plastic strain (b) contours of the LS-Dyna model for CFSSP-NB1 at 3.00% drift.

Table 4. Wall Parameters Considered in Parametric Study											
CFSSP Model	D/t_s	S/t_s	t_c, in.	b, in	t_c/b	Wall Height, in.	Aspect Ratio	Web Thickness, in.	HSS Diameter, in.	HSS Thickness, in.	Design Parameter Investigation
NB-D/t_s	44.8	25.6	8	40	0.20	120	2.47	5/16	8.3125	5/32	D/t
NB-S/t_s	25.52	51.2	8	40	0.20	120	2.47	5/16	8.3125	5/16	S/t
NB-0.1b	25.52	25.6	4	40	0.10	120	2.70	5/16	4.3125	5/32	t_c
NB-0.4b	25.52	25.6	8	20	0.40	70	2.45	5/16	8.3125	5/16	t_c
NB-0.57b	25.52	25.6	8	14	0.57	55	2.43	5/16	8.3125	5/16	t_c
NB-0.8b	25.52	25.6	8	10	0.80	45	2.42	5/16	8.3125	5/16	t_c
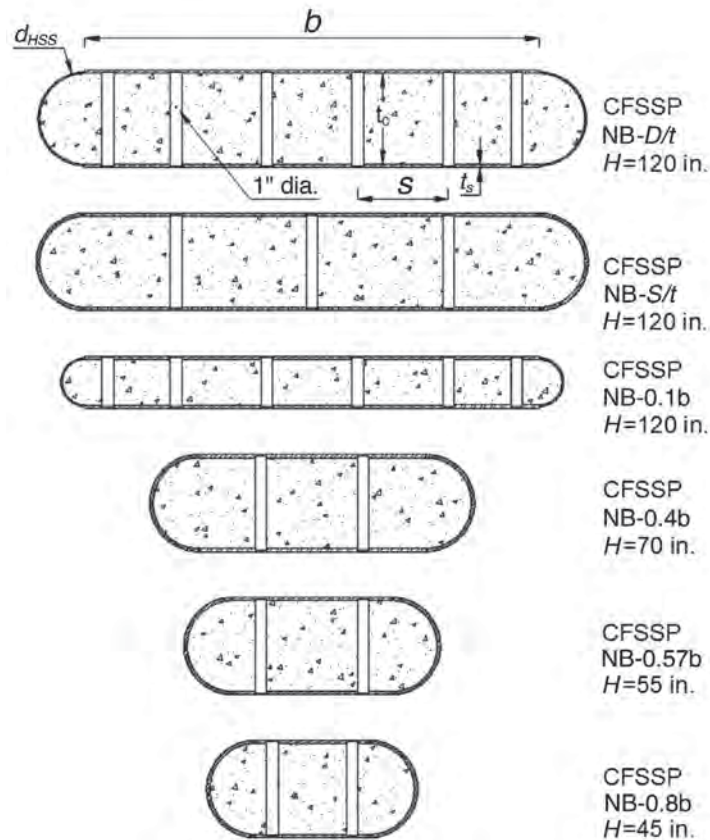
Fig. 8. Wall cross section used in the parametric study.

and concrete. Note that different Y-axes are used in Figure 9 to better show the hysteretic contributions of each parts of the wall and the comparison of total strength versus plastic flexural strength. The plastic flexural strength is shown in terms of base shear ($V_p = M_p/H$). As shown for all cases, the plastic flexural strength, calculated using simple plastic theory, was exceeded by the finite element model results.

Note that the steel material model does not have any damage properties; therefore, no strength degradation can be obtained from the numerical model due to steel plate fracture under low-cycle fatigue loading. One way to estimate low-cycle fatigue life of these walls is to use the cumulative plastic strain values at failure, obtained based on experimentally observed steel plate fracture location and drift

as described earlier. Therefore, to compare the low-cycle fatigue life of these walls, Figure 10 shows lateral load versus cumulative plastic strain histories of failure critical elements, which are typically located at the middle of the buckled wave formed at the wall boundaries. Based on Figure 10, model NB-S/t has the highest plastic strain accumulation at a given drift, which is attributed to the larger plate buckling amplitudes it develops compared to the other cross sections considered. Note that model NB-0.1b has a coarse mesh at the wall boundaries due to its small wall thickness, and its results may be correspondingly more approximate. In order to approximate the failure drift ratio for these walls, a cumulative plastic strain at fracture of 1.5 is assumed [a reasonable approximate value, based on the reported failure
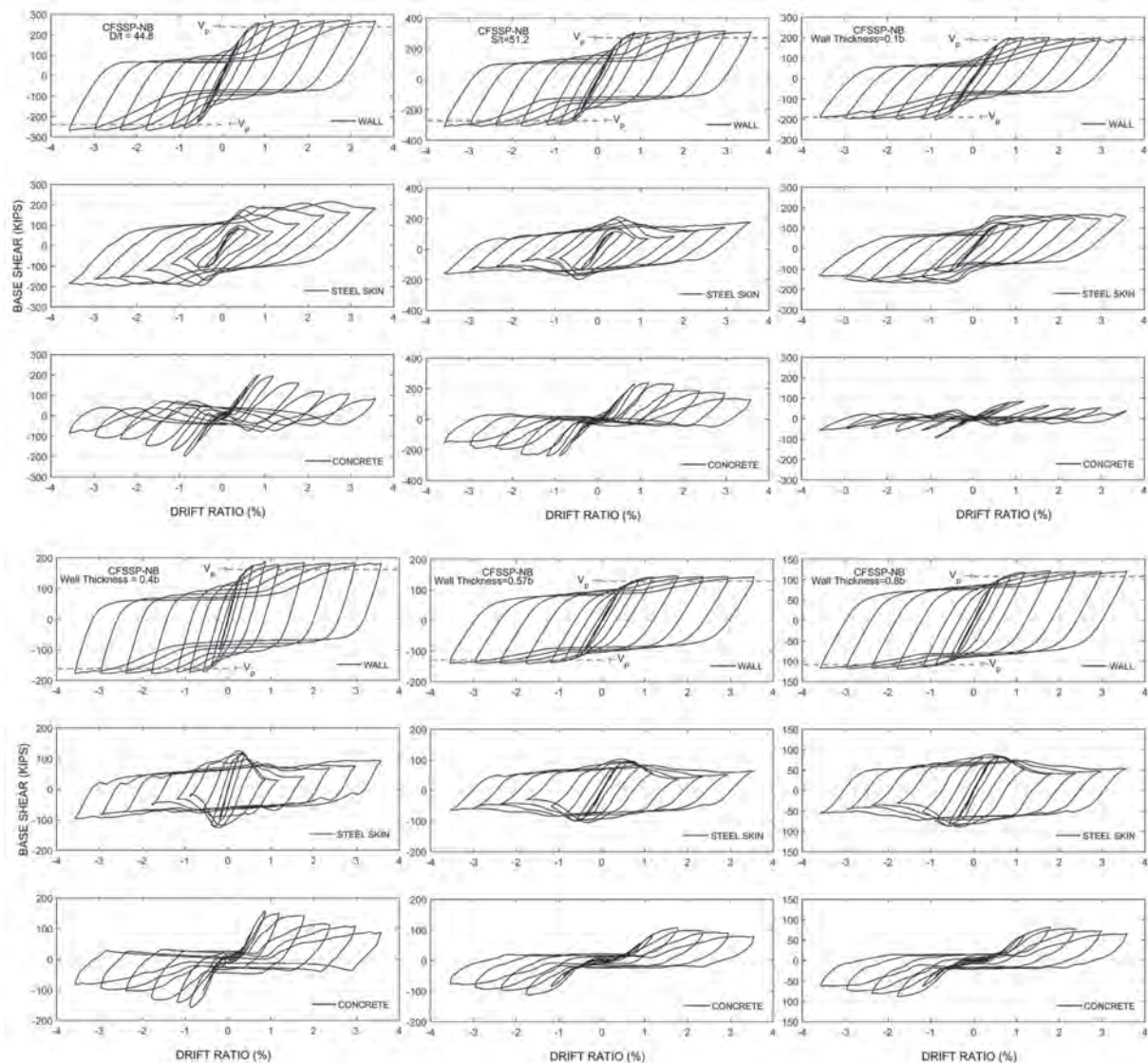
Fig. 9. Hysteresis loops of the of the walls with different cross sections.

cumulative plastic strain value of 1.40–1.45 obtained by Polat and Bruneau (2017) for the CFSSP-B2 wall model]. Based on this information, as shown in Figure 9, models NB D/t, S/t, 0.1b, and 0.4b could sustain their strength up to a 3% drift ratio, while models 0.57b and 0.8b could do so up to a 3.6% drift ratio.

T-SHAPED CFSSP-WALLS

The previously described finite element approach and techniques were then used to investigate the behavior of CFSSP-Walls having T-shaped cross sections. For this purpose, two different cross sections were considered: (1) a T-shaped wall tested by Eom et al. (2009), which was referred to as

DSCW3, and (2) an arbitrary cross section obtained by modifying the geometry of that DSCW3 wall. First, dimensions and properties of the materials used in those walls are presented. Then, to complement this, the plastic flexural strength of these walls are calculated using simple plastic theory and the same assumed uniform plastic stress distributions on steel and concrete sections used previously (Alzeni and Bruneau, 2014, 2017); closed-form equations are also provided for this purpose. Finally, experimentally reported lateral force versus drift and lateral force versus axial strain are compared with those obtained from the finite element analyses, and the numerical results are used to provide additional insights into behavior of T-shaped CFSSP-Walls.
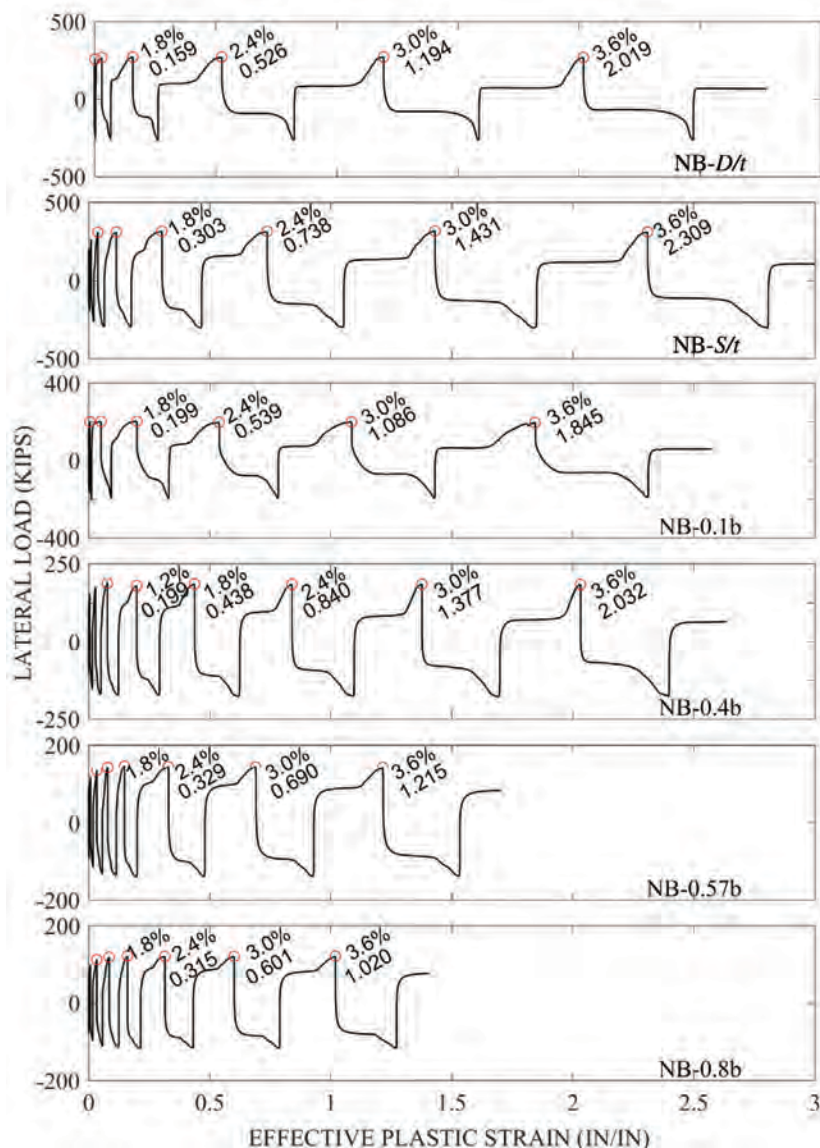
Fig. 10. Effective plastic strain histories of the fracture critical steel elements of the CFSSP-Walls.

Cross-Section Geometry, Material Properties, and Plastic Moment

Figure 11 illustrates the cross-section and dimensions of the DSCW3 wall, together with parameters used to develop closed-form equations to calculate plastic flexural strength under negative and positive drift. The DSCW3 section has a full depth, b, of 39.4 in. (1000 mm); a flange width, w, of 23.6 in. (600 mm); a uniform wall thickness (same for web and flange), t, of 4.7 in. (120 mm); a steel plate thickness, t_s, of 0.4 in. (10 mm); and a tie-bar spacing to steel plate thickness ratio, S/t_s, of 30. Figure 11 also illustrates the axial stress blocks for negative (Figure 7a) and positive (Figure 7b) wall drifts, and the corresponding tension and compression force vectors used to obtain the plastic neutral axis and plastic moment of the cross sections. Note that these two selected stress distributions assume that the plastic neutral axis is within the range 0 to $(b - t)$ for case a (negative drift) and within the range $(b - t)$ to $(b - t + t_s)$ for case b (positive drift). The closed-form equations for the plastic flexural strength [which assume uniform steel yield strength, F_y, and concrete compressive strength, f_c'] are derived subsequently. Table 5 presents the closed-form equations for C and M_p for these two cases, as well as all the other possible cases of plastic neutral axis locations, such as to cover any general cross-section dimensions (not illustrated). In Table 5 and Figure 11, C is the depth of the compression zone, which is calculated and derived from the axial force equilibrium in the cross section; other parameters are as defined previously. For the DSCW3 wall, the yield, F_y, and ultimate, F_u, strength of the steel plates are 55 ksi (383 MPa) and 79 ksi

(544 MPa), respectively, and the compressive strength, f_c', of the filled concrete is 5.8 ksi (39.7 MPa).

Using the equations in Table 5, the geometry shown in Figure 11, and the material properties reported earlier, the plastic neutral axis of the DSCW3 wall was calculated to be located at 24.0 in. (610 mm) (Figure 11a) and 4.7 in. (119 mm) (Figure 11b) from the outermost compression fiber of the wall under negative and positive drift, respectively, which correspondingly falls in the wall's web and in the bottom steel plate of the wall flange, respectively. The base shear force at plastic moment, given as M_p/H, is 272 kips and 230 kips under negative and positive wall drifts, respectively.

Note that for some locations of the plastic neutral axis (for different geometries), greater axial strain values may develop in the wall web or wall flange, which in turn may affect the buckling behavior of the steel plates and change the ultimate wall strength. To address these issues that may arise, and to investigate the effect of wall geometry on wall behavior, another wall with different cross-section geometry was considered here. This additional example has a wall flange width equal to about three times that of the DSCW3 wall, but with the same wall web and material properties, and is referred as DSCW3-3W. Table 6 presents the plastic neutral axis and plastic moment values of both the DSCW3 and DSCW3-3W walls under negative and positive drifts. Note that for the DSCW3-3W wall, the plastic neutral axis is located within the thickness of the steel flange bottom plate under negative drift and within the thickness of the infill concrete of wall flange under positive drift.
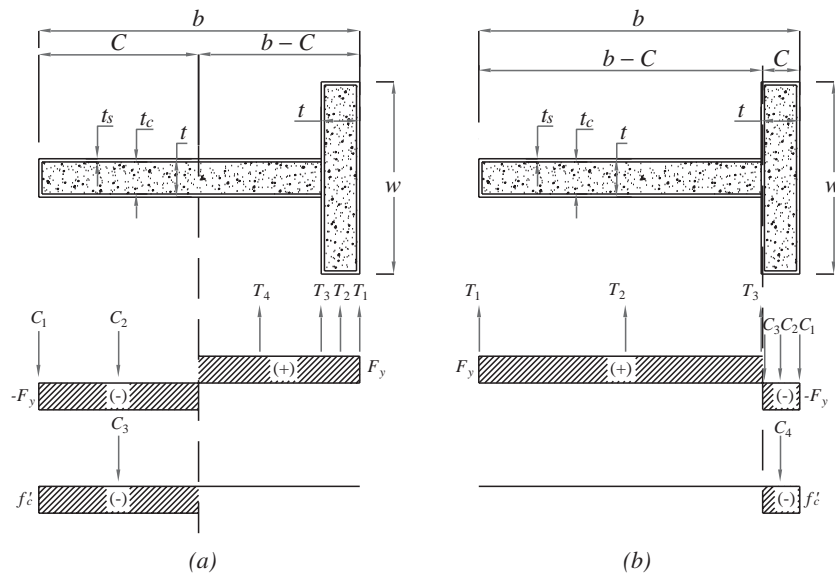

Fig. 11. Cross-sectional parameters of T-shaped walls and stress blocks used to calculate flexural strength of T-Walls: (a) T-Wall under negative drift; (b) T-Wall under positive drift.

Table 5. Plastic Flexural Strength of T-Walls	
Location of PNA	**Equations for M_p and C (positive drift)**
In flange concrete	$M_p = (0.5t_s^2 w - Ct_s w + 0.5C^2 w)f_c' + \{-2t_s^3 + (w - 2.5t_c)t_s^2 + [2C^2 + (-t - 2b)C + wt_c + b(b + t_c)]t_s\}F_y$
	$C = \dfrac{t_s(2F_y b + F_y t_c + f_c' w)}{4F_y t_s + f_c' w}$
In bottom plate of flange	$M_p = (-0.5t_c^2 w + wt_c C - 1t_s wt_c)f_c' + \{8t_s^3 + (3.5t_c - 4b - 2C + 2w)t_s^2 + [(-1b + C + 3w)t_c + b^2 - 2wC]t_s + wt_c^2 + wC^2 - 2wt_c C\}F_y$
	$C = \dfrac{\left[-4t_s^2 + (2b + 2w - 3t_c)t_s + 2wt_c\right]F_y - t_c wf_c'}{2wF_y}$
	Equations for M_p and C (negative drift)
In wall web	$M_p = (-0.5t_c Ct_s + 0.5t_c C^2)f_c' + \{4t_s^3 + (-2w + 4C - 4b + 1.5t_c)t_s^2 + [2C^2 + (-2w + t_c - 2b)C + b^2 + 2wb - 1wt_c]t_s\}F_y$
	$C = \dfrac{t_s F_y(2b - t_c - 4t_s + 2w)}{4F_y t_s + f_c' t_c}$
In bottom plate of flange	$M_p = \left[4.5t_s^2 t_c + (-3bt_c + 3t_c^2)t_s + 0.5b^2 t_c - bt_c^2 + 0.5t_c^3\right]f_c' + \{8t_s^3 + (2C + 2w + 3.5t_c - 6b)t_s^2[(-C + 3w)t_c + (-2b + 2C)w + b^2]t_s + t_c^2 w + (-2b + 2C)wt_c + (-2bC + C^2 + b^2)w\}F_y$
	$C = \dfrac{\left[(-2w + 3t_s)t_c + 4t_s^2 + (-2b - 2w)t_s + 2wb\right]F_y - t_c(b - 3t_s - t_c)f_c'}{2wF_y}$

PNA = plastic neutral axis
C = depth of the compression zone
M_p = plastic moment of the cross section

Table 6. Plastic Neutral Axis and Plastic Moment Values of the T-Walls				
	DSCW3		**DSCW3-3W**	
Wall Parameters	**(−) Drift**	**(+) Drift**	**(−) Drift**	**(+) Drift**
C (in.)	24.0	4.71	35.0	4.0
M_p (kip-in.)	39936	33768	50932	40683
V_p (kips)	272	230	347	277

Finite Element Modeling of T-Shaped Walls

Finite element models of the DSCW3 and DSCW3-3W walls were developed using LS-Dyna following the same modeling approaches described previously. Material properties for steel and concrete were defined using the values given previously. For the bi-linear steel material model definition, the elastic modulus was 29,000 ksi (200,000 MPa), and the post-yield tangent modulus was 234 ksi (1610 MPa).

The DSCW3 cantilever wall tested by Eom et al. (2009), with a height of 142 in. (3600 mm), was fixed at its base by welding the steel skin of the wall to an ~2-in. (50-mm)-thick base plate, itself bolted to a concrete foundation. The specimen was strengthened at the bottom by using cover plates with a thickness of 0.40 in. (10 mm) over a height of 11 in. (280 mm). In the finite element analyses, the base plate used in the experimental set-up was not modeled; instead, the wall model was perfectly fixed at the base. The finite element

models followed the experimental loading protocol (which terminated at −2.0% drift ratio), but applying only one cycle per drift amplitude as opposed to two during the experiment. Note that initial failure of the tested DSCW3 wall occurred when the web wall failed from the local buckling of the steel plate, crushing of the infill concrete, and tie-bar fracture at −2.0% drift ratio that resulted in strength degradation of the wall (Eom et al., 2009). After this wall failure first occurred during a cycle in one direction [deemed the negative direction by Eom et al. (2009)], testing continued by monotonic loading of the wall in the opposite (positive) direction until tensile fracture of the steel plate occurred at a 4.9% drift ratio (Eom et al., 2009).

Figure 12 shows the LS-Dyna model for the DSCW3 wall. To expedite the run-time of the simulation, only half of the wall was modeled using symmetry boundary conditions, and the numerical solution was executed using the nonlinear static implicit solution procedure of the program. Figure 13 shows the cyclic displacement history and the user-defined step size employed in the definition of displacement curves

in the program. The step size curve adjusts the time steps of the displacement history protocol over the analysis period and is useful to expedite the numerical simulation in the elastic range (by using larger step size) and improve numerical convergence in the inelastic range of the wall simulation (by using smaller step size).

Simulation Results of T-Shaped Walls

Figure 14 shows the lateral load versus drift ratio relationship of the DSCW3 and DSCW3-3W wall models, including individual contributions from the steel skin and the infill concrete. The numerical model developed for the DSCW3 wall exhibited stiffer behavior than measured in the test, but no attempt was made here to calibrate the model's stiffness because it would have required explicit modeling of the base plate and the stiffness of the bolts used to attach the base plate to the floor (which was beyond the scope of the current work and not of interest). As shown in the figure, the base shear strength of the wall that corresponds to the calculated
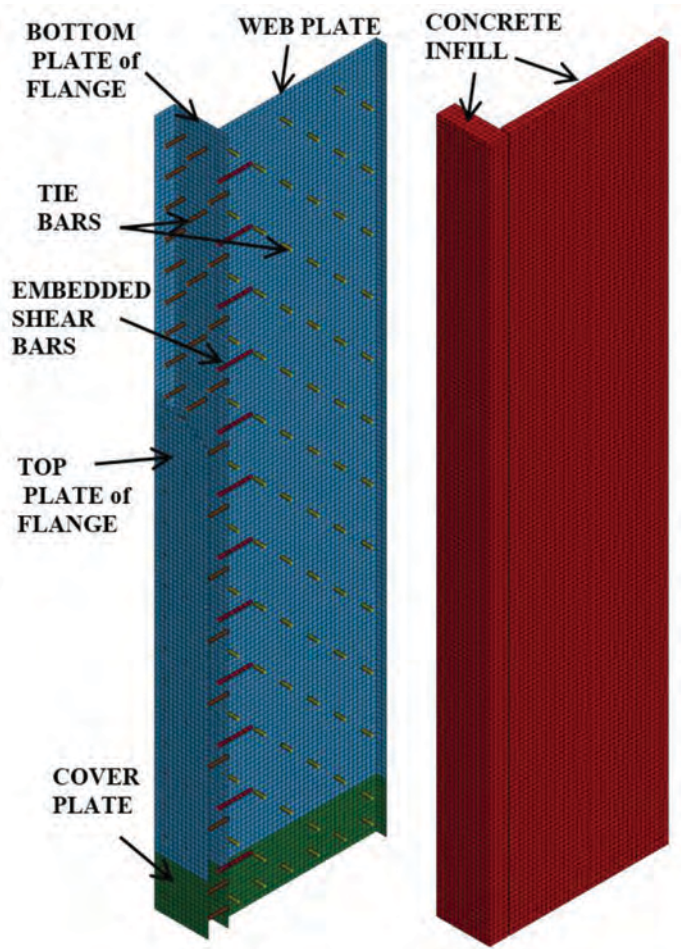

Fig. 12. LS-Dyna model of the half-symmetric T-Wall DSCW3.

plastic moment was exceeded, which indicates that the ultimate flexural capacity of the wall can be conservatively predicted by the simple plastic theory. For the DSCW3 model, the plastic moment was achieved at about +0.7% and −0.6% drift, whereas it was reached at +1.0% and −0.8% drift for the DSCW3-3W model. The ultimate moment capacity achieved by the finite element models (i.e., at ±2.0% drift) are greater than the calculated plastic moment capacity by a factor of 1.23 and 1.24 for the DSCW3 wall and 1.12 and 1.25 for the DSCW3-3W wall. The experimentally measured maximum strengths of the DSCW3 wall (in positive and negative drift) are shown in Figure 14a, by $V_{u(EXPR)}$, to be 290 kips and 273 kips under positive and negative drift, respectively. The ultimate wall strength under the positive drift was successfully captured by the numerical model, whereas in the negative direction, the ultimate wall strength was overestimated by an amount of 23%. The finite element model was able to capture the local buckling of the wall's web steel plate at −2.0% drift ratio and subsequent concrete crushing, which is also indicated by the strength degradation in the negative displacement direction, shown in Figure 14.
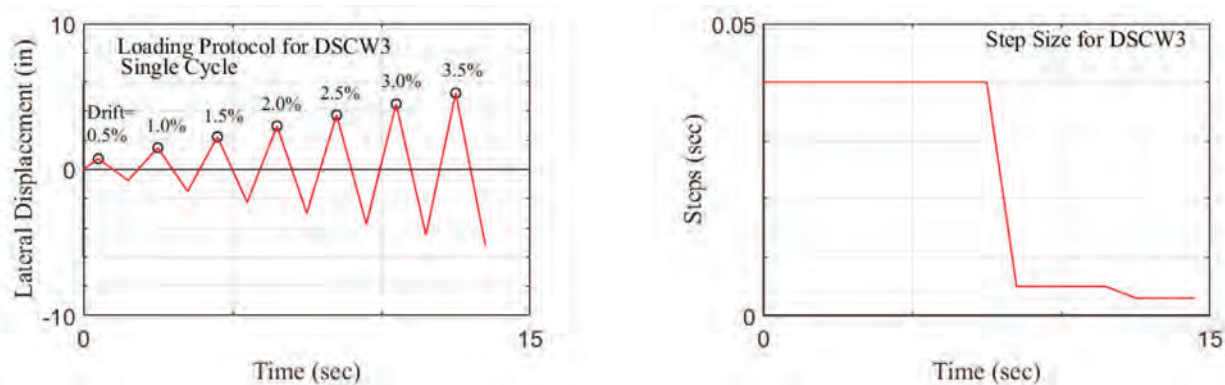
Fig. 13. Displacement loading history and time step size used in the finite element analyses of DSCW3 and DSCW-3W wall models.
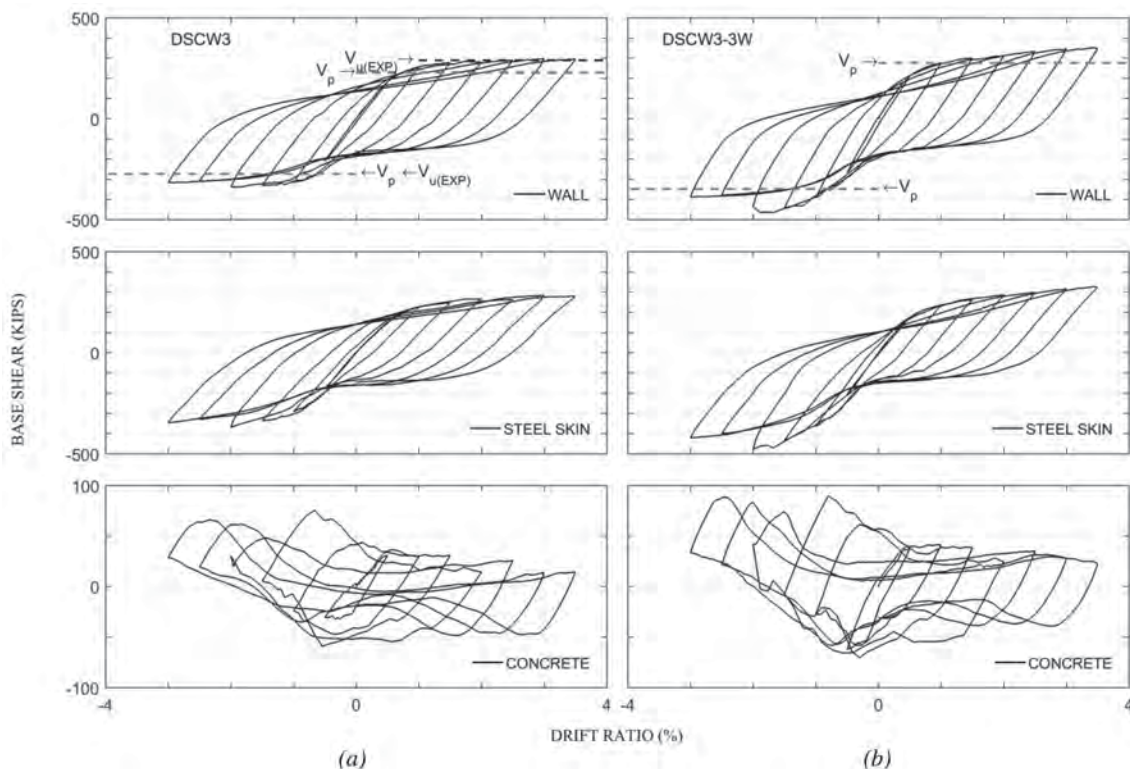

Fig. 14. Hysteresis curves of the LS-Dyna models of T-Walls: (a) DSCW3; (b) DSCW3-3W.

Note that the finite element simulation does not capture tie-bar fracture, which was one of the failure mechanisms of the Eom et al. (2009) specimen at a −2.0% drift ratio in addition to steel plate local buckling of web plate and concrete crushing. Simulation results of the DSCW3 model indicate that the bar located above the buckling wave (located at the outermost location of the first row of tie-bars above the cover plate) starts yielding at a 1.5% drift ratio. Because all the steel material model definitions (i.e., for steel plates and tie-bars) assumed bi-linear behavior with strain hardening, the possible strength degradation due to tie-bar fracture was not captured, which otherwise would have resulted in more severe strength degradation at −2.0% and beyond. Therefore, the wall response shown in Figure 14 is representative of the expected wall response if tie-bar failure can be prevented.

The axial strain values obtained from the finite element analyses results were found to be in agreement with those experimentally measured at the outermost wall depths and above the cover plates (i.e., at 12 in. from the base). Figure 15 shows the lateral force–axial strain histories obtained from the numerical model of DSCW3 model. The tensile axial strain at the end of the web wall, consistent with what was reported by Eom et al. (2009), was greater than that in the wall flange (attributed to the location of the neutral axis, which is close to the wall flange). The respective experimentally measured and finite element obtained axial strain values at the end of the wall web plate are 0.023 versus 0.026 at +1.0% drift and 0.041 versus 0.047 at +1.5% drift, and strain values for the steel plate at the wall flange are 0.021 versus 0.018 at −1.5% drift. Note that strains were obtained at regions away from the buckled zone of the plates to be representative of plane–strain values and avoid the regions of strain magnification due to local buckling; also note that for the wall flange, readings at the outermost location on the Y-axis are used here. Moreover, the reported tensile strain at failure is 0.041 mm/mm, whereas the numerically obtained value is 0.047 mm/mm.

The following sections present finite element analysis results for cyclic stress-strain history of the steel plates at the wall base, initiation and progression of steel plate buckling of the web and flange steel plates of the T-shaped walls, and the shear and normal stress distribution of the steel and concrete parts of the walls under increased cyclic wall drifts.

Stress-Strain History of Steel Plates in DSCW3 and DSCW3-3W

One of the purposes of analyzing wall DSCW3-3W (a modified geometry of DSCW3) was to investigate how behavior is affected by different neutral axis locations, which may increase or decrease axial strain and stress demands and affect the onset of steel plate buckling and ultimate wall strength. As shown in Table 6, changing the geometry from DSCW3 to DSCW3-3W reduces the compression depth under positive drift, increases it under negative drift, and modifies the force vectors (shown in Figure 11) used to calculate the plastic flexural strength of the section. Note that for DSCW3-3W under positive drift, the neutral axis is located within the thickness of the infill concrete of the wall flange.

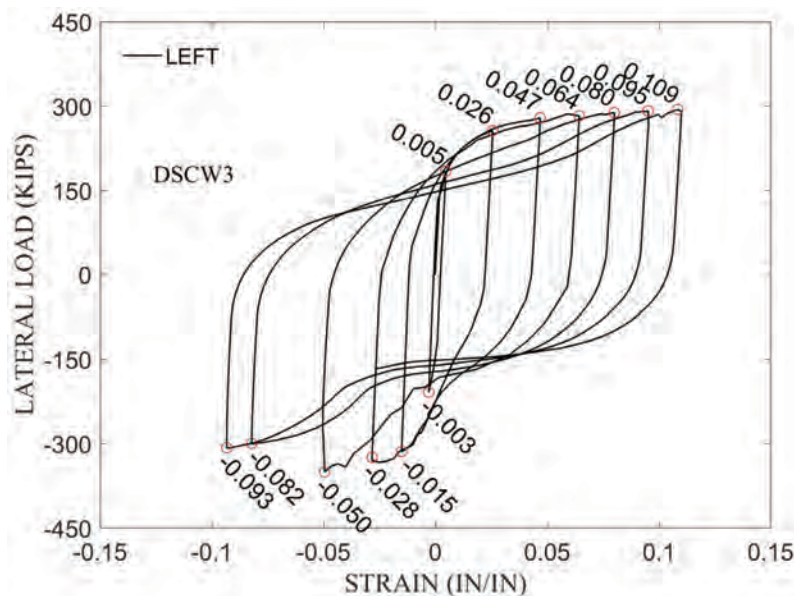Shell elements located just above the cover plate (at a 12-in. distance from the wall base) and evenly distributed

Fig. 15. Lateral load versus steel strain relationship obtained from the LS-Dyna model for DSCW3.

along the cross-sections of the models were used to plot vertical uniaxial stress-strain response of these elements under cyclic loading. Figure 16 shows the location of these selected elements on the half-symmetric cross section of the finite element models and the global coordinates used. Figures 17 and 18 show the vertical uniaxial stress-strain history of the selected shell elements shown in Figure 16 (the shell middle integration point values are plotted). Note that the X-axis is not the same in all plots in these figures to better show the various points in each plot. The points when peak positive drift amplitudes were reached are marked on each curve using numbers from 1 to 6, respectively corresponding to the first and sixth drift amplitude level (+0.5% and +3.5% drift ratio, respectively). Plastic neutral axis locations of the wall models can also be bracketed by observing the sign of the axial stresses in Figure 17 (defined as positive in tension) at each specific peak positive drift amplitudes; for example, from Figure 17a, it is seen to be within the range of 25.2 to

34.1 in. in the global X-axis direction (defined in Figure 12) for the DSCW3 wall model.

Figure 17 also shows that the stress-strain response of the web plate is approximately similar for both models except in regions close to wall plastic neutral axis. For both models, yielding of the wall web plate starts at about 0.5% drift at the outermost location.

Figure 18 shows that yielding in the wall flange steel top plate of the DSCW3 model initiates at about +1.0% drift and at about +2.0% drift for the DSCW3-3W model. On the other hand, yielding of the bottom plate of the DSCW3 model initiates at about +2.0% drift, whereas yielding never occurs for the bottom plate of the DSCW3-3W model. Moreover, the bottom plate of the DSCW3-3W model is in tension under peak positive drift, which indicates that the neutral axis is located somewhere between the bottom and top plates but close to the bottom plate. The stress-strain response of both the top and bottom steel plates of the wall flange of the
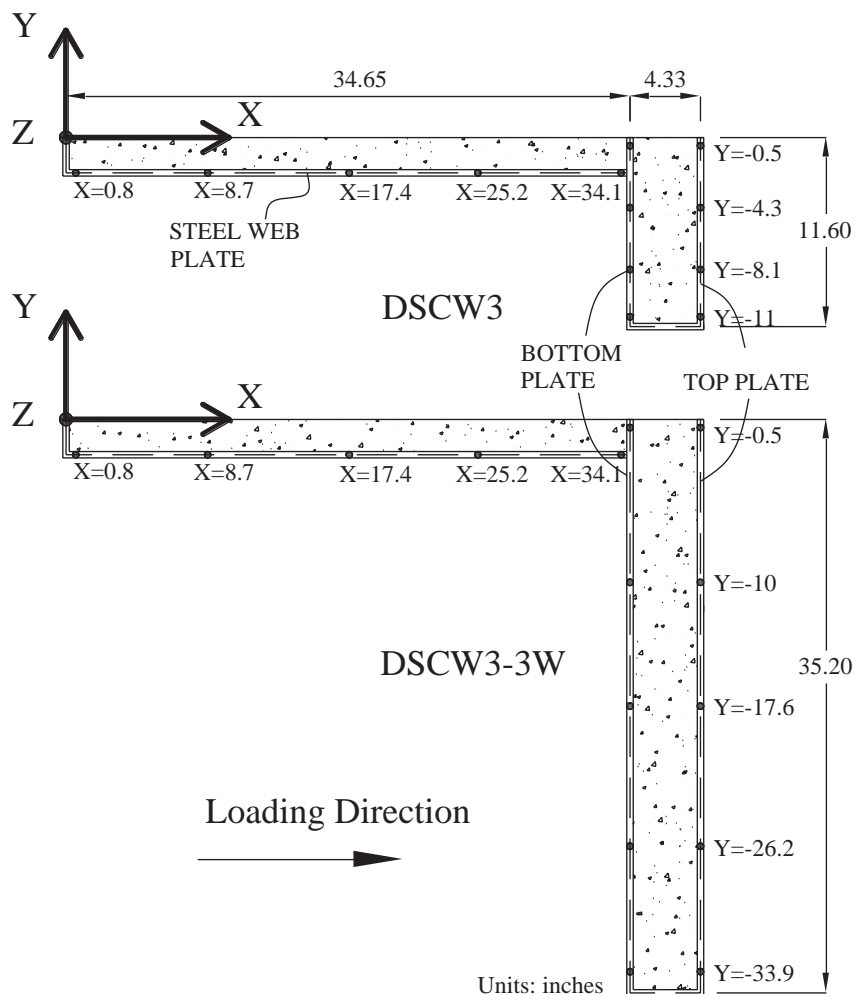

Fig. 16. Half-symmetric cross section of the DSCW3 and DSCW3-3W
wall model and selected steel element location in the global coordinate system.
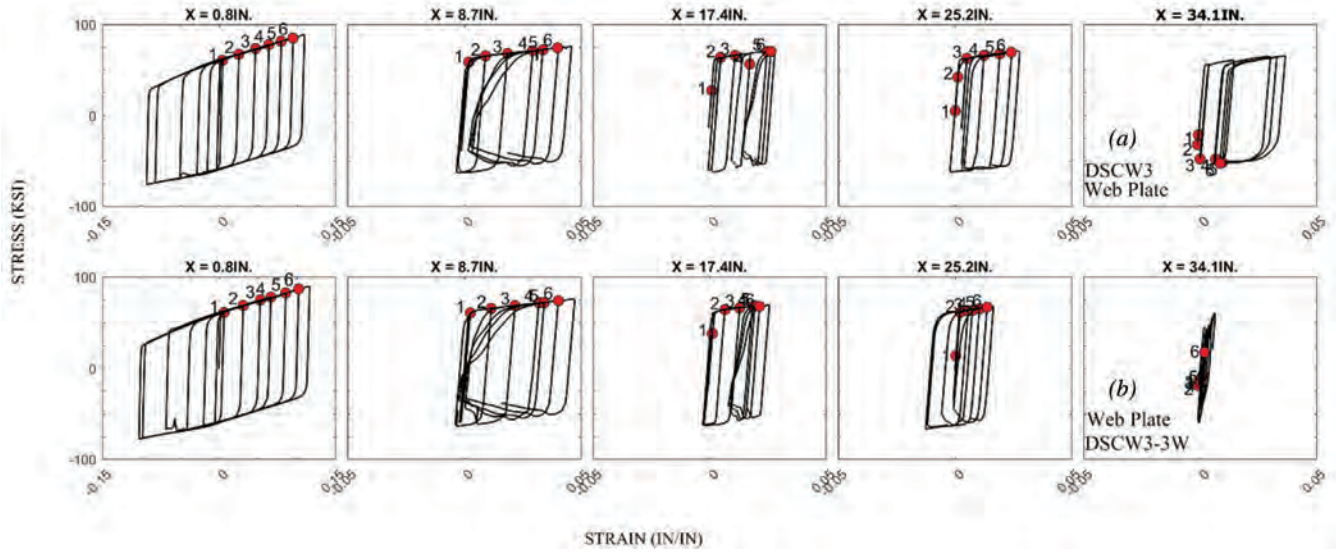
Fig. 17. Stress-strain relationship of steel web plate at 12-in. height: (a) DSCW3; (b) DSCW3-3W.
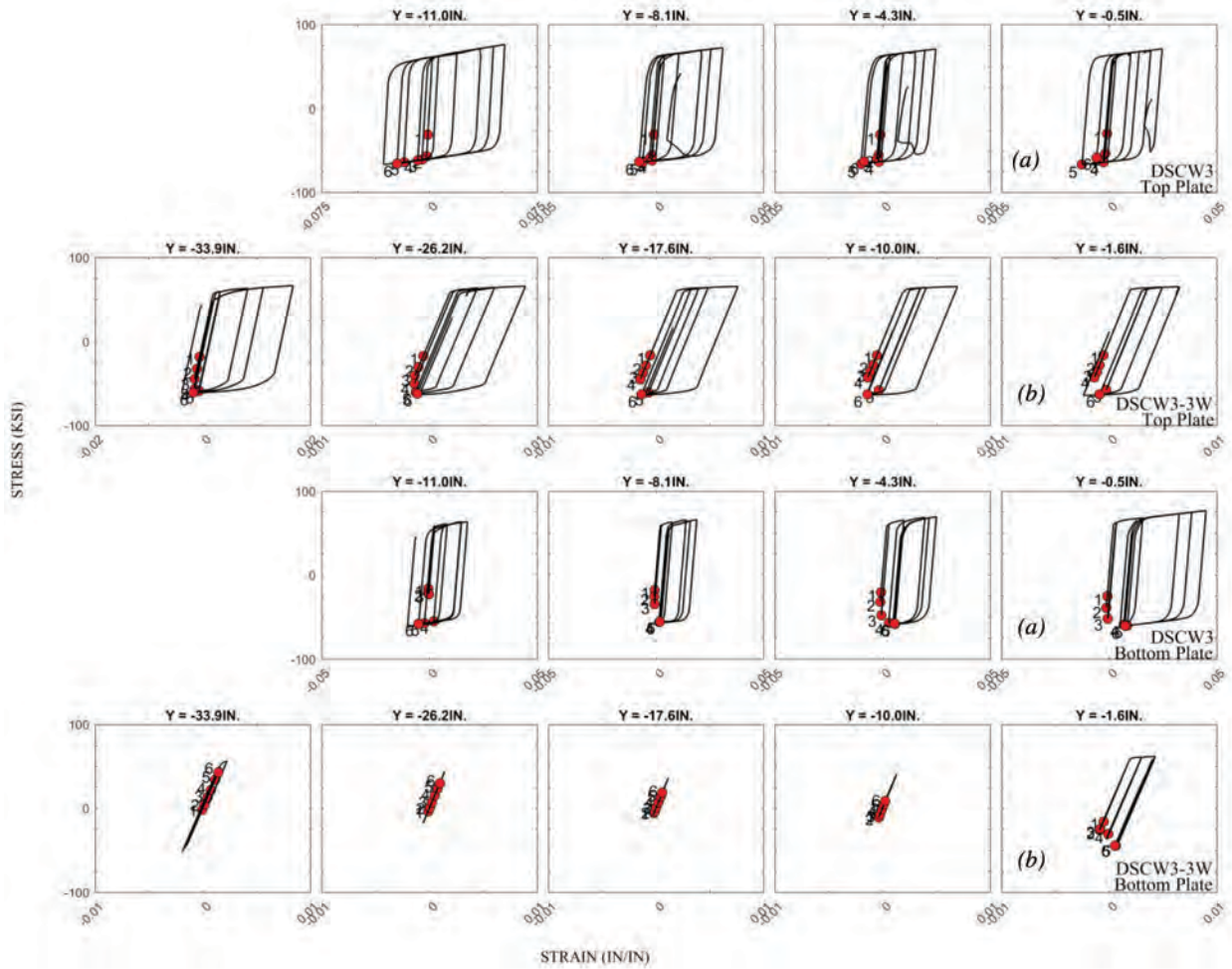

Fig. 18. Stress-strain relationship of steel flange top plate at 12-in. height: (a) DSCW3; (b) DSCW3-3W.

DSCW3-3W model at a 24-in. wall height (one tie spacing above the location considered in Figure 18) indicates total elastic response for all drift considered (not shown here).

Figure 18 reveals that shell elements located closer to the mid-flange width (closer to wall centerline) at this wall elevation (12 in.) attains lower vertical strain values than the ones located further away. This behavior (more significant for the DSCW3 wall model) was deemed to be a consequence of the flange top plate buckling pattern, which exhibited higher amplitude buckling waves toward the wall centerline (buckling wave amplitudes are presented in the following section). These higher strain values at the outermost elements are also a result of increased strain demands in this region due to the formation of compression diagonals following the plate buckling (not shown here but typically visible when plotting principal stress vectors). However, stress-strain histories obtained at higher wall elevations (i.e., at 24 in., where local steel plate buckling does not develop) than considered in Figure 18 show that the vertical strains are higher close to wall centerline.

Steel Plate Local Buckling

Experimental studies of CFSSP-Walls (Alzeni and Bruneau, 2014, 2017; Eom et al., 2009) showed that steel plate buckling eventually develops during their cyclic flexural response. Studying the individual strength contribution of these walls using the finite element methods (presented previously) revealed that steel plate buckling may or may not affect the global wall strength; however, it may modify the contributions of the individual wall parts to the total strength. As described earlier for the CFSSP-Walls tested by Alzeni and Bruneau (2014, 2017), steel plate buckling reduces the contribution of the steel plates to total strength, but the wall strength is not proportionally reduced because the force demand partially shifts to the concrete infill. However, for the T-shaped CFSSP-Wall tested by Eom et al. (2009), the concrete infill could not sustain the force demand itself following the steel plate buckling, which resulted in an early failure of the wall.

For both the DSCW3 and DSCW3-3W wall models, local buckling of the steel plates developed between the second and the third row of tie-bars, whereas buckling developed between the third and the fourth row of tie-bars in the actual DSCW3 specimen. Figure 19 shows the buckling wave amplitudes of the steel web plates (Figure 19a) and steel flange top plates (Figure 19b) of the DSCW3 and DSCW3-3W models along their horizontal lengths against increasing peak drift amplitudes (web plate buckling is shown under negative drift, whereas steel flange plate buckling is shown under positive drift). Note that for the DSCW3-3W model, steel flange plate buckling was not significant and is not shown in Figure 19b. The figure shows that for both models, web plate local buckling develops at −1.0% drift

and gradually increases in amplitude under larger drifts. The tensile axial strain (obtained from the outermost steel element of the web wall) at the onset of local buckling of the DSCW3 model ($S/t_s = 30$) is 0.026 in./in. (see Figure 15). This value is comparable to those obtained for the fixed-base CFSSP-Walls analyzed previously [i.e., 0.024 in./in. for CFSSP-NB1 ($S/t_s = 25.6$), seen in Figure 3]. Figure 19 shows that web plate buckling wave amplitudes are larger for the DSCW3-3W model than the DSCW3 model at any given drift. This is mainly due to the larger compression depth of the cross-section of the DSCW3-3W model (thus larger axial strains) than the DSCW3 model under negative drift.

Stress Analysis of Steel Skin and Infill Concrete of T-Shaped Walls

The previously developed simplified solutions to predict the wall neutral axis and plastic flexural strength of the T-shaped CFSSP-Walls assumed that uniform uniaxial yield strength of the steel skin and uniaxial compression strength of the concrete infill was attained on each side of the plastic neutral axis of the cross section of the wall. Although this approach is simple and practical to conservatively predict the ultimate wall strength, the actual stress distribution may vary due to steel plate buckling, stress amplitudes and distribution in the concrete compression zone, and von Mises interaction of stresses [for the planar CFSSP-Walls, hoop stresses increased the steel yield strength 15% on one side with vertical tensile stresses and reduced by the same amount on the other side of the wall's neutral axis with vertical compressive stresses, as shown by Polat and Bruneau (2017)]. Strain hardening of the steel skin (if steel plate buckling is avoided under high strains) may also have a noticeable effect for a T-shape wall that has a compression depth that varies significantly under different direction of wall drift as a consequence of the cross section being unsymmetrical. For planar CFSSP-Walls, Polat and Bruneau (2017) showed that assumption in the shape and amplitude of the concrete stresses has a major effect on the wall neutral axis location.

Finite element results were used to get shell (for steel sections) and solid (for concrete sections) element stress values to obtain stress distribution along the section depth at the prescribed wall elevation. These stress distributions, plotted for steel skin and concrete infill separately, are used also to quantify the normal and shear stress contributions on the steel plate yielding, the effect of confinement on the axial strength of the infill concrete.

The stresses are reported in the global coordinate system, such that assuming that in-plane loading lies in the X-Z plane, the vertical normal stress is given by σ_z, transverse normal stress is given by σ_x, and the shear stress is given by σ_{zx}. The origin of the global axes is as shown in Figure 16. Note that, the reported values of stresses in the concrete are actually an average of the through thickness solid elements.

Figures 20 and 21 show the stress distribution of the DSCW3 model, and Figures 22 and 23 show the stress distribution of the DSCW3-3W model at peak drift amplitudes along the depth of the cross sections of the walls (including flange depth). In these figures, shell element results are reported in panel a of each figure, and solid element results are reported in panel b of each figure. Note that, the wall depth (X-axis label of the figures) includes both the depth of the web and the thickness of the wall flange, The stress distributions of the steel skin were obtained from the web plate and flange side boundary plate that lie on the X-axis (see Figure 16). Also note that the stress distribution plots of the solid (concrete) elements (panel b of each figure) is discontinuous near the edge to denote that the infill flange and web concrete are physically separated (a steel plate is present in between the two, as shown in Figure 16).

The vertical stress (σ_z) distribution of the cross section reveals the location of the elastic and plastic neutral axis of the wall. For example, focusing on the results of the DSCW3 wall model shown in Figures 20 and 21, location of the plastic neutral axis falls into the wall web for both drift directions. For comparison with the theoretical prediction, for example, Figure 21 indicates a plastic neutral axis located at 9 in. under +3.0% drift, whereas theory predicted 4.7 in. (see Table 6). While, in this figure, the average concrete distribution and its strength is similar to that used in the simple plastic theory (i.e., uniform and $f_c' \sim 5.8$ ksi), the higher compression depth value obtained from the finite element analysis was deemed to be a result of wall flange top plate buckling. Similarly, the predicted compression depth was 24 in. under negative wall drift, which compares reasonably with the value indicated in Figure 20 (i.e., at −1.50% drift,
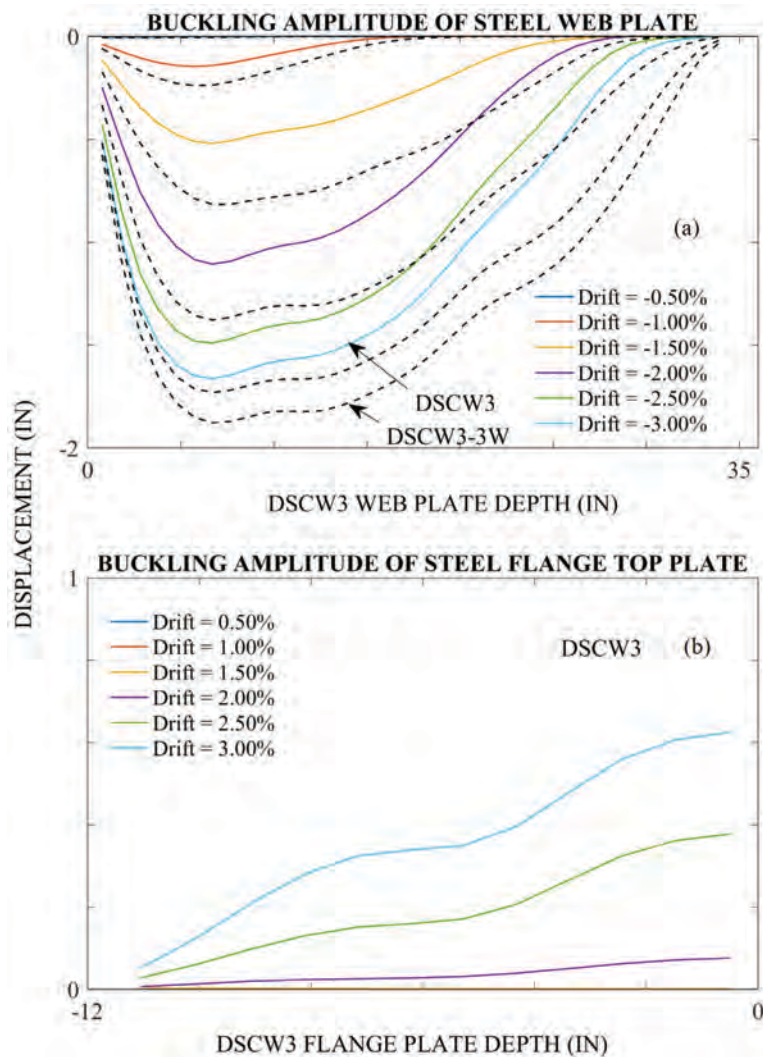

Fig. 19. Maximum local buckling amplitude of the LS-Dyna models of the T-Walls:
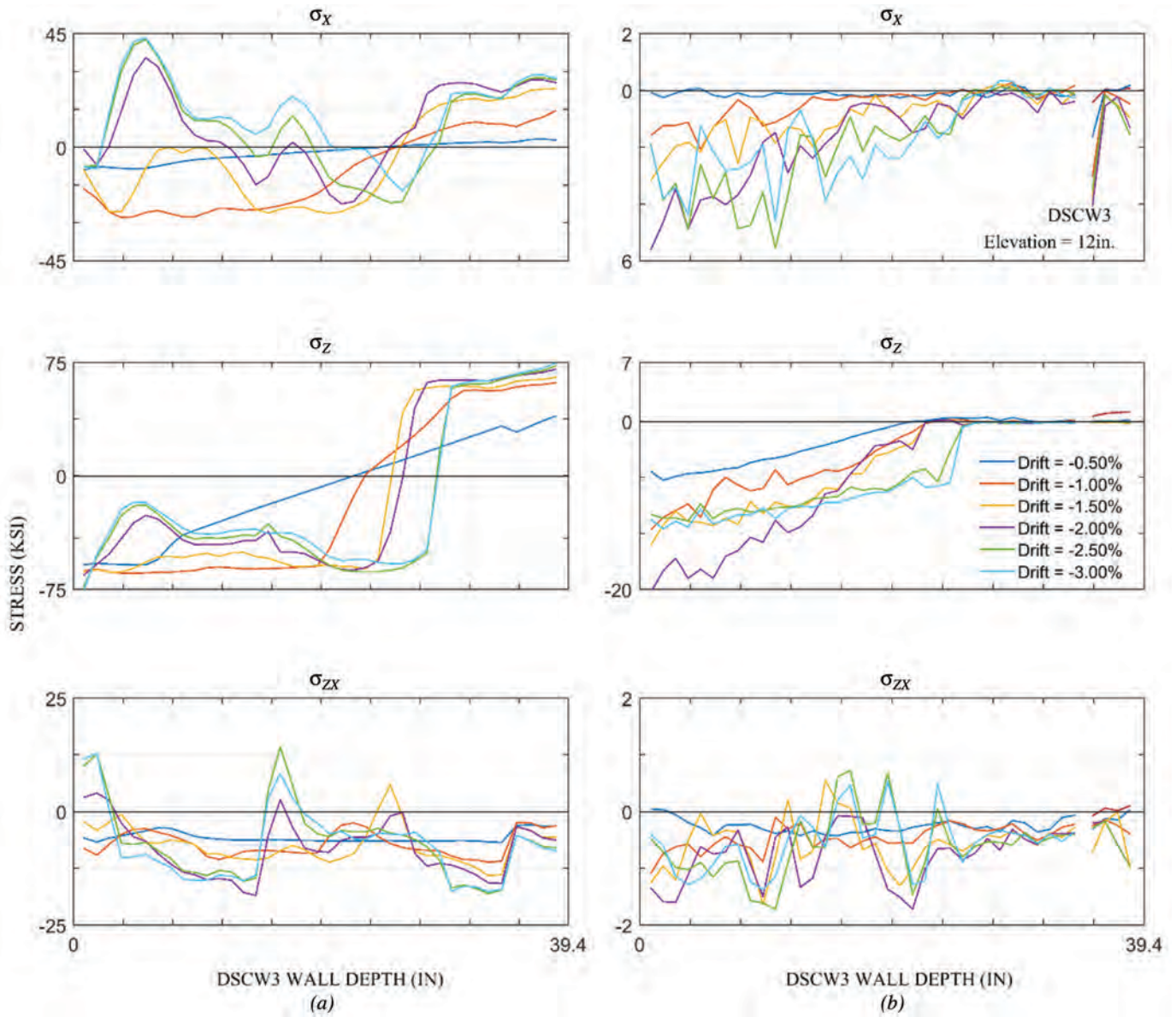*(a) steel web plate under peak positive drift; (b) steel flange top plate under peak negative drift.*

Fig. 20. Plane stress distribution of the cross section of the LS-Dyna model of DSCW3 located at 12-in. wall
height under negative drift: (a) shell stress distribution in steel skin; (b) average solid stress distribution in concrete.
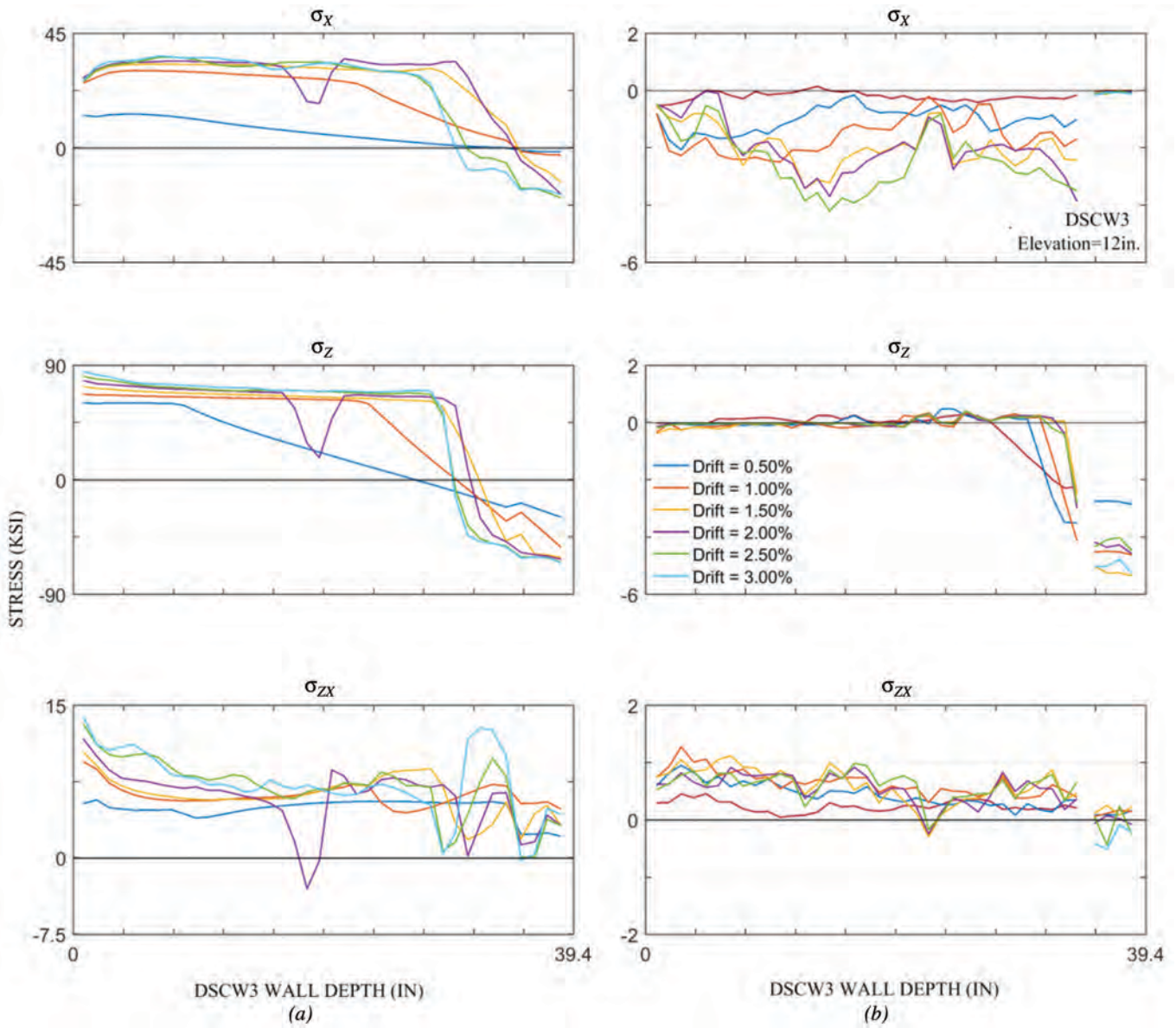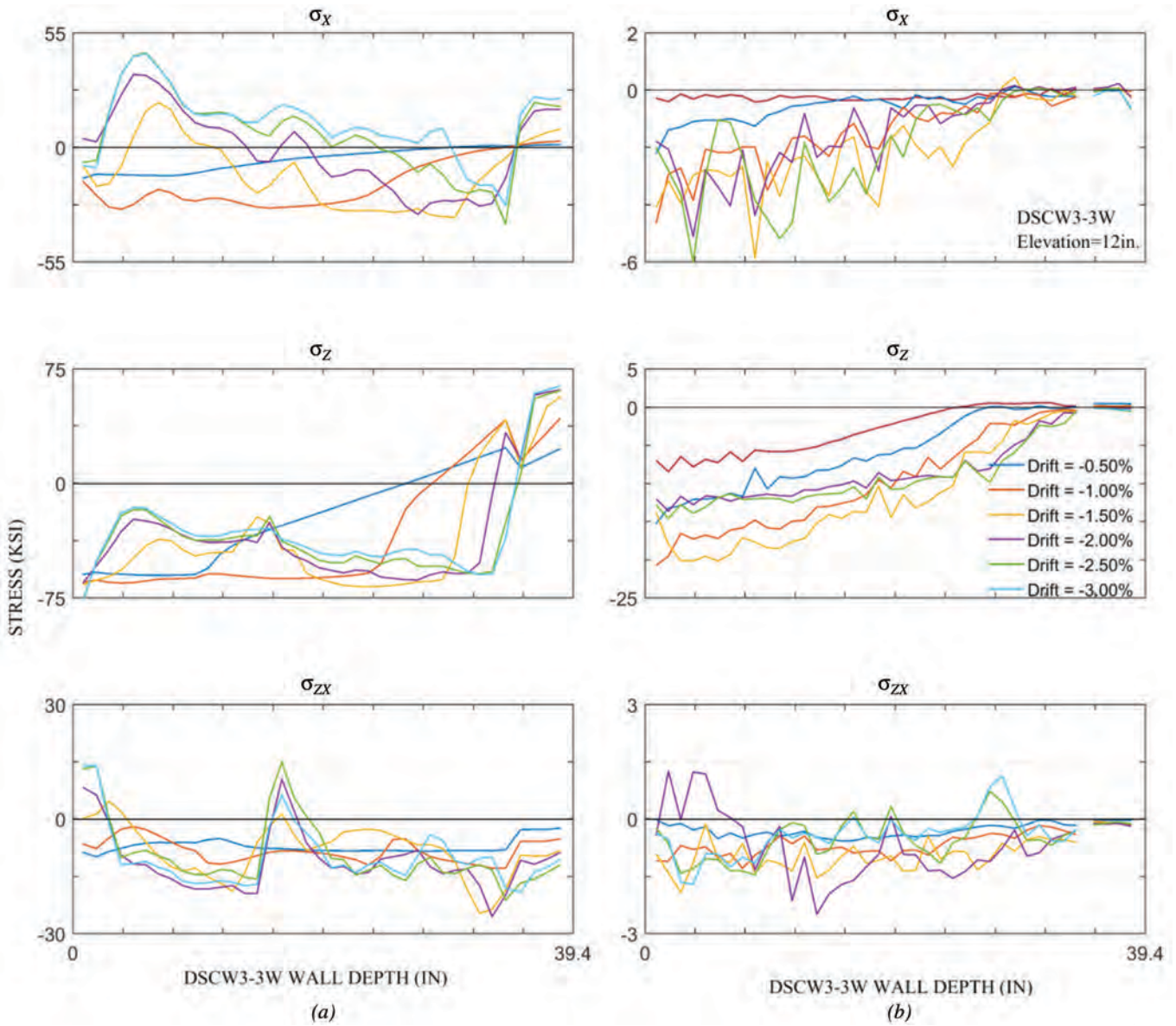
Fig. 21. Plane stress distribution of the cross section of the LS-Dyna model of DSCW3 located at 12-in. wall height under positive drift: (a) shell stress distribution in steel skin; (b) average solid stress distribution in concrete.
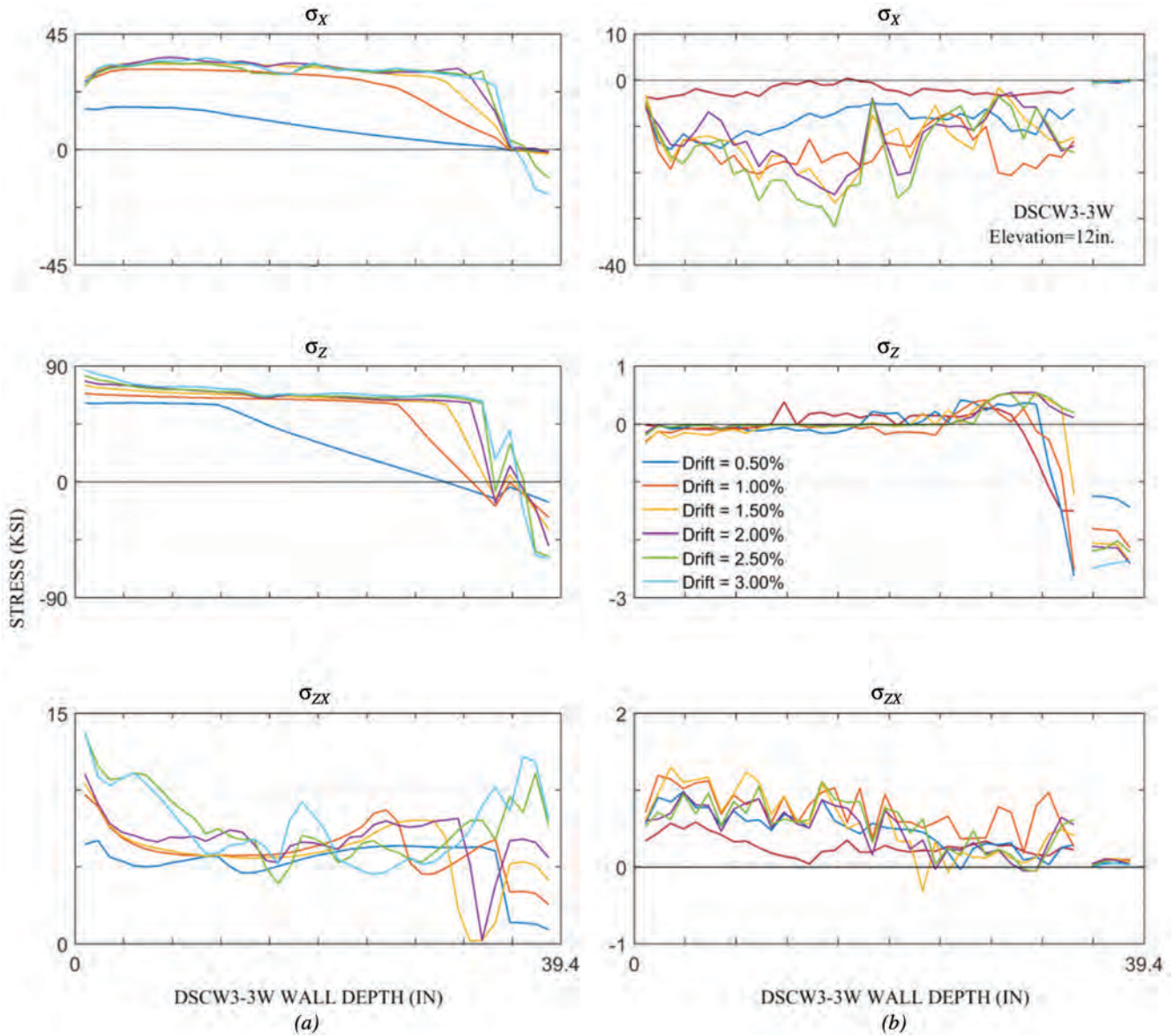
Fig. 22. Plane stress distribution of the cross section of the LS-Dyna model of DSCW3-3W located at 12-in. wall height under positive drift: (a) shell stress distribution in steel skin; (b) average solid stress distribution in concrete.

Fig. 23. Plane stress distribution of the cross section of the LS-Dyna model of DSCW3-3W located at 12-in. wall
height under negative drift: (a) shell stress distribution in steel skin; (b) average solid stress distribution in concrete.

before severe web plate buckling developed). Note that, although the stress blocks are not perfectly consistent with the ones assumed in this case (i.e., the concrete compression stress distribution is more triangular than rectangular in Figure 20 at −1.50% drift), the increase of concrete compressive strength under confinement (up to 12 ksi compared to the unconfined strength of 5.8 ksi) is the reason for the close match between the compression depth values obtained from simple plastic theory and finite element results that exhibits nonuniform concrete compression distribution.

Steel and average concrete vertical stress distribution under negative drift shown in Figures 20 (DSCW3) and 22 (DSCW3-3W) indicate that concrete crushing follows steel plate buckling. For example, in these figures, steel strength starts to decrease following the steel plate buckling developed at −1.0% drift and is substantially reduced by −2.0% drift to the point where, at −2.0% drift, concrete compressive stresses have increased up to four times the uniaxial compressive strength. However, at larger drifts beyond −2.0%, concrete strength drops significantly as an indication of concrete crushing.

The average concrete vertical stress distribution of DSCW3 under positive drift (Figure 21) shows that infill concrete of the wall flange was able to reach its uniaxial compressive strength of 5.8 ksi, whereas for the DSCW3-3W model, it reached only half of its strength (Figure 23). The confinement effect of the steel web plate on the concrete is more notable under negative drift, as the results indicate in Figures 20 and 22. Average concrete vertical stress results, in these figures, indicate that concrete can attain strength values up to 20 ksi before the development of steel plate buckling, which is four times its uniaxial capacity. This is possibly an artifact of the computer model and would need to be challenged experimentally.

Under positive drift (i.e., with outermost element of wall web under tensile stresses), the transverse normal stresses of the wall web plate attain values as high as half that of the axial stresses, while the steel shear stresses attain values one-tenth of that.

Yielding and Prediction of
Failure Drift Ratio of DSCW3

Polat and Bruneau (2017) established the cumulative strain value at fracture due to low-cycle fatigue upon repeated inelastic cycles for the CFSSP-B2 wall previously tested by Alzeni and Bruneau (2014). Assuming this value to be representative for composite walls of this type, the drift at which wall DSCW3 would have fractured can be estimated using the finite element model presented earlier. The DSCW3 T-shaped wall considered here was tested cyclically until buckling at −2% drift and monotonically after that up to fracture at 4.9% drift. Because the tensile strain at fracture for monotonically loaded steel differs from that obtained from a cyclic low-cycle fatigue test, the finite element model is used to estimate failure drift of the DSCW3 wall had it been tested continuously under cyclic loading. This analysis follows the same procedure described earlier in the paper for planar fixed-base CFSSP-Walls.

Figure 24 shows the bottom third of the T-shaped walls subjected to the most damage (i.e., steel plate local buckling, higher von Mises yield stress, and effective plastic strain), under cyclic loading, at 3% drift (assuming the original cyclic protocol had been followed up to that drift, but only with a single cycle at each peak drift value). Note that the higher effective plastic region is where, during the test, fracture occurred under monotonic loading in the positive direction (following the cyclic loading terminated at −2.0% drift). Cumulative plastic strain history obtained from the element having the most severe effective strain (indicated by the effective plastic strain contours) was used to predict the failure drift ratio of the fixed base DSCW3 wall model had it been tested cyclically per the original protocol up to failure.

Figure 25 shows the history of the effective plastic strain of that element from the finite element simulation of the DSCW3 wall. The figure illustrates the logarithmic increase of the effective plastic strain under increased drift amplitudes of the wall. Table 7 presents the effective plastic strain values at peak drift amplitudes corresponding to the preceding protocol, as well as the values corrected to correspond to two cycles per drift at all drift levels [i.e., the originally intended Eom et al. (2009) protocol]. The corrected values indicate that this specimen would have sustained a ductility up to a drift of −3.0% (i.e., when it reached a cumulative plastic strain of 2.8) had the experiment continued under cyclic displacement. The dashed red line on that figure provides the same results if the specimen was subjected to monotonic loading after −2.0% drift. Note that the effective plastic strain values do not increase significantly after the +2.5 drift ratio in that case.

VERTICAL SHEAR FORCES OF
THE WALL FLANGE TIE BARS

Finite element results of the DSCW3 and DSCW3-3W were used to obtain the shear forces on the tie-bars, to compare results between the two walls, and to investigate the relative contribution of the tie-bars in resisting shear for the two different T-wall flange depth considered. For demonstration purposes, tie-bars located at the third row from the wall bottom [located just above the cover plate in Eom et al.'s (2009) specimen] were used. This row has four tie-bars located 14.7 in. from the wall base in the DSCW3 model. Note that the half-symmetric finite element model has two tie-bars located at −4.8 in. and −9.5 in. on the global Y-axis from the symmetry plane of the wall, as shown in Figure 26. For the DSCW3-3W model, there are four bars in the
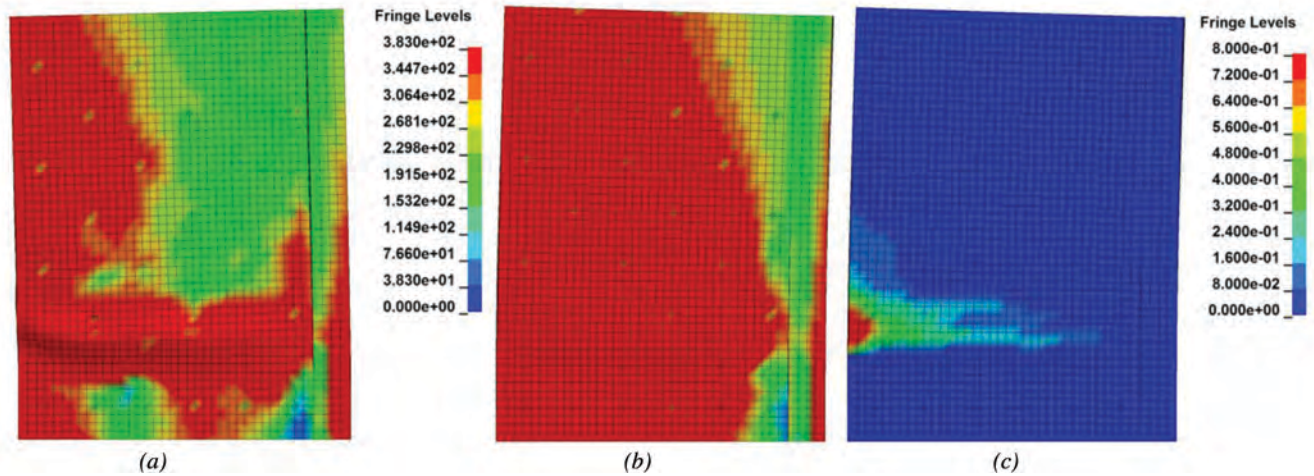
DSCW3
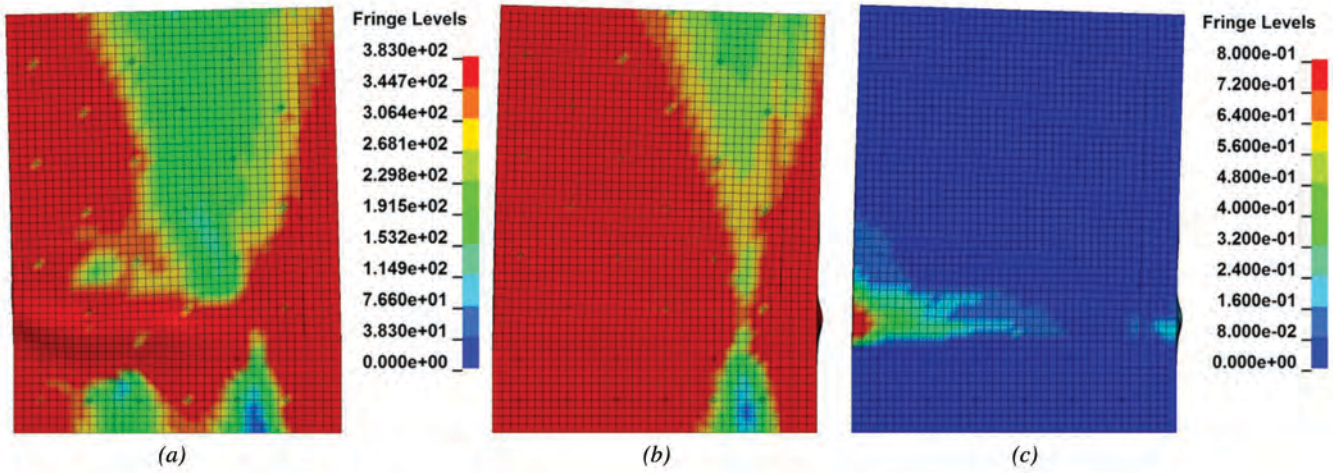
DSCW3-3W

Fig. 24. Stress and strain contours of the LS-Dyna model for DSCW3 (above) and DSCW3-3W (below): (a) von Mises stress at −3.0% drift; (b) von Mises stress at 3.0% drift; (c) effective plastic strain at 3.0% drift. (Note: Units shown are MPa; 1 MPa = 0.145 ksi.)

| Table 7. Effective Plastic Strain Values for the DSCW3 Wall Model at Peak Drift Amplitudes						
DSCW3						
Drift Ratio (%)	Cycle Order (i)	Cycle for Each Drift (n)	Plastic Strain (PS) LS-Dyna (single cycle)	$PS_{i+1} - PS_i$	$n \times$ $PS_{i+1} - PS_i$	$\sum n \times$ $(PS_{i+1} - PS_i)$ (corrected PS, double cycle)
0.5	1	2	0.003	0	0	0
−0.5	1	2	0.008	0.005	0.01	0.01
1.0	2	2	0.027	0.019	0.038	0.048
−1.0	2	2	0.067	0.04	0.08	0.128
1.5	3	2	0.124	0.057	0.114	0.242
−1.5	3	2	0.211	0.087	0.174	0.416
2.0	4	2	0.32	0.109	0.218	0.634
−2.0*	4	2	0.468	0.148	0.296	0.93
2.5	5	2	0.637	0.169	0.338	1.268
−2.5	5	2	0.87	0.233	0.466	1.734
3.0	6	2	1.117	0.247	0.494	2.228
−3.0	6	2	1.393	0.276	0.552	**2.78**
3.5	7	2	1.681	0.288	0.576	3.356
* Cyclic loading stopped in actual test due to web plate buckling and concrete crushing.						
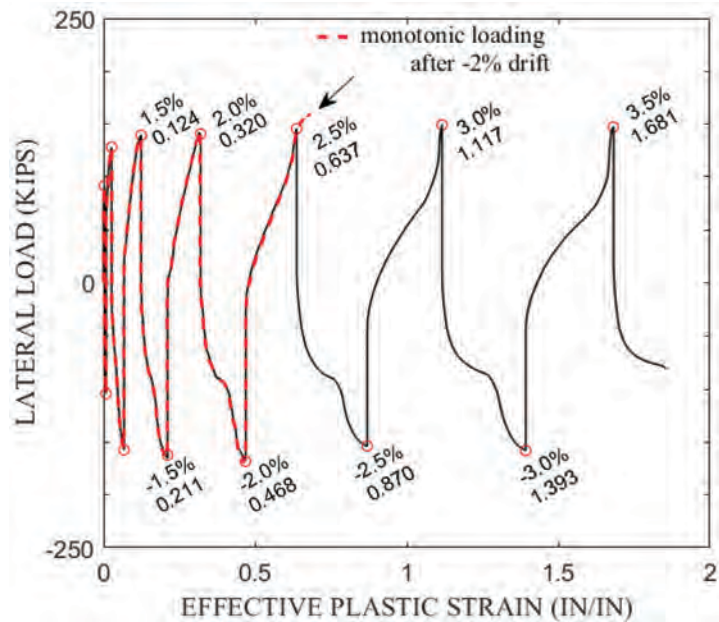
Fig. 25. *Effective plastic strain history of the fracture critical element of the web steel plate.*

half-symmetric finite element model in each row (eight bars in the actual wall), and they are located at −4.8, −14.3, −23.8 and −32.3 in. on the Y-axis from the axis of symmetry of the finite element model. as shown in Figure 26. Note that the tie-bars were modeled with beam elements that were located through the thickness of the infill concrete, and the end nodes of the beams were coupled with the solid nodes of the infill concrete. Figure 20 shows the history of the vertical shear forces at peak drift amplitudes of the wall models. The shear forces were reported at the centroid of each beam element (shown by the solid circles in the figure). Results indicate that interior and exterior beam elements are subjected to opposite shear forces. Another important observation is that vertical shear demands for the ties of the DSCW3-3W model are higher than for DSCW3 model. For the DSCW3-3W model, shear demand on the tie-bars is diminished at

regions away from the axis of wall symmetry. These beam forces are below the assumed shear yield strength of the tie-bars, which is roughly 9.3 kips (tie-bars have a 0.63-in. diameter and 50-ksi yield strength).

CONCLUSION

A finite element model previously developed by Polat and Bruneau (2017) and calibrated against experimental results was used here to analyze CFSSP-Walls having different cross-sections and properties in order to investigate more broadly the cyclic inelastic behavior of such composite walls.

Results from re-analyses of previously tested walls with fixed-base boundary conditions (to eliminate any complexity and uncertainty that may arise when including foundation flexibility) were used to obtain tensile axial strain values at
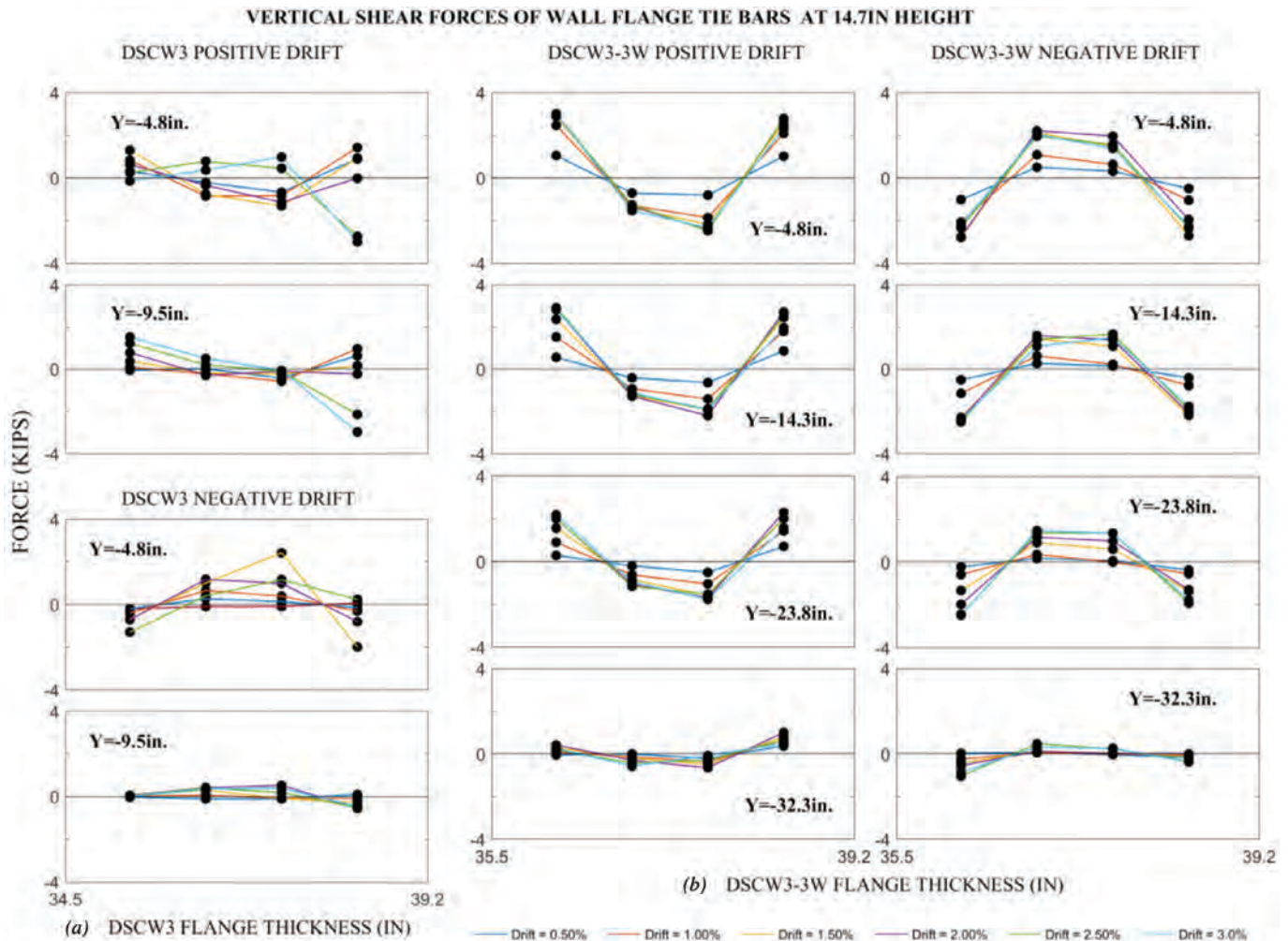

Fig. 26. Vertical shear forces of the wall flange tie-bars at peak drift amplitudes: (a) beam forces of the DSCW3 model; (b) beam forces of the DSCW3-3W model, under positive and negative drift.

the onset of steel plate buckling, to obtain C_3 values of the concrete, and to estimate the ultimate wall drift that the wall can be sustained under low-cycle fatigue loading without due effect of foundation flexibility.

A parametric study conducted considering different parameters that define CFSSP-Walls, such as D/t, S/t_s and t_c/b, showed that for all cases considered, simple approaches adopted to predict wall plastic flexural strength gives conservative results.

CFSSP-Walls having T-shaped sections were also investigated using the finite element modeling approaches considered throughout. Analyses were performed for a wall tested by Eom et al. (2009), and for a modified configuration having a much greater flange width. Plastic flexural strength of these walls (obtained through simple plastic theory) were shown to be conservative. The modified (increased) flange width of the T-shaped section resulted in the change of the wall compression depths, affected the axial strain demands on the steel web and flange plates, changed the buckling behavior of the steel plates, and reduced the moment contribution of the infill concrete of the wall flange and flange steel plates as a result of reduced axial stress demands. On the contrary, vertical shear forces of the tie-bars located through the thickness of the wall flanges were found to be increased.

ACKNOWLEDGMENTS

REFERENCES

AISC (2016), *Seismic Provisions for Structural Steel Buildings*, ANSI/AISC 341-16, American Institute of Steel Construction, Chicago, IL.

Alzeni, Y. and Bruneau, M. (2014), "Cyclic Inelastic Behavior of Concrete Filled Sandwich Panel Walls Subjected to In-Plane Flexure," Technical Report MCEER-14-0009, Multidisciplinary Center for Earthquake Engineering Research, State University of New York at Buffalo, Buffalo, NY.

Alzeni, Y. and Bruneau, M. (2017), "In-Plane Cyclic Testing of Concrete Filled Sandwich Steel Panel Walls with and without Boundary Elements," *Journal of Structural Engineering*, under review.

Booth, P.N., Varma, A.H., Sener, K.C. and Malushte, S.R. (2015), "Flexural Behavior and Design of Steel-Plate Composite (SC) Walls for Accident Thermal Loading," *Nuclear Engineering and Design*, Vol. 295, pp. 817–828.

Bowerman, H., Gough, M. and King, C. (1999), *Bi-Steel Design and Construction Guide*, British Steel Ltd., Scunthorpe, London.

Epackachi, S., Nguyen, N.H., Kurt, E.G., Whittaker, A.S. and Varma, A.H. (2014), "In-Plane Seismic Behavior of Rectangular Steel-Plate Composite Wall Piers," *Journal of Structural Engineering*, Vol. 141, No. 7, pp. 1–9.

Epackachi, S., Whittaker, A.S., Varma, A.H., and Kurt, E.G. (2015), "Finite Element Modeling of Steel-Plate Concrete Composite Wall Piers," *Engineering Structures*, Vol. 100, pp. 369–384.

Eom, T.-S., Park, H.-G., Lee, C.-H., Kim, J.-H. and Chang, I.-H. (2009), "Behavior of Double Skin Composite Wall Subjected to In-Plane Cyclic Loading," *Journal of Structural Engineering*, Vol. 135, No. 10, pp. 1,239–1,249.

Goto, Y., Kumar, G.P., and Kawanishi, N. (2010), "Nonlinear Finite-Element Analysis for Hysteretic Behavior of Thin-Walled Circular Steel Columns with In-Filled Concrete," *Journal of Structural Engineering*, Vol. 136, No. 11, pp. 1,413–1,422.

Hallquist, J.O. (2006), "LS-DYNA Theory Manual," Livermore Software Technology Corporation, Livermore, CA.

Hibbett, Karlsson and Sorensen Inc. (1998), *ABAQUS/ Standard: User's Manual*, Vol. 1.

Imani, R. and Bruneau, M. (2014), "Post-Earthquake Fire Resistance of Ductile Concrete-Filled Double-Skin Tube Columns," Technical Report MCEER-14-0008, Multidisciplinary Center for Earthquake Engineering Research, State University of New York at Buffalo, Buffalo, NY.

Krieg, R. and S. Key (1976), "Implementation of a Time Independent Plasticity Theory into Structural Computer Programs," *Constitutive Equations in Viscoplasticity: Computational and Engineering Aspects*, pp. 125–137.

Kurt, E.G., Varma, A.H., Booth, P. and Whittaker, A.S. (2016), "In-Plane Behavior and Design of Rectangular SC Wall Piers without Boundary Elements," *Journal of Structural Engineering*, Vol. 142, No. 6.

LSTC (Livermore Software Technology Corporation) (2015), "LS-Dyna, Keyword Users Manual," Vols. 1 and 2, Version 971.

Oduyemi, T. and Wright, H. (1989), "An Experimental Investigation into the Behaviour of Double-Skin Sandwich Beams," *Journal of Constructional Steel Research*, Vol. 14, No. 3, pp. 197–220.

Polat, E. and Bruneau, M. (2017), "Modeling Cyclic Inelastic In-Plane Flexural Behavior of Concrete Filled Sandwich Steel Panel Walls," *Engineering Structures*, under review.

Ramesh, S. (2013), "Behavior and Design of Earthquake-Resistant Dual-Plate Composite Shear Wall Systems," Purdue University, West Lafayette, IN.

Schwer, L. (2011), "The Winfrith Concrete Model: Beauty or Beast? Insights into the Winfrith Concrete Model," *Proceedings of the 8th European LS-DYNA Users Conference*, pp. 23–24.

Sener, K. and Varma, A.H. (2014), "Steel-Plate Composite SC Walls: Experimental Database and Design for Out-of-Plane Shear," *Journal of Constructional Steel Research*, Vol. 100, pp. 197–210.

Sener, K., Varma, A.H. and Ayhan, D. (2015), "Steel-Plate Composite SC Walls: Experimental Database and Design for Out-of-Plane Flexure," *Journal of Constructional Steel Research*, Vol. 108, pp. 46–59.

Seo, J., Varma, A.H., Sener, K. and Ayhan, D. (2016), "Steel-Plate Composite (SC) Walls: In-Plane Shear Behavior, Database, and Design," *Journal of Constructional Steel Research*, Vol. 119, pp. 202–215.

SIMULIA (2012), "Abaqus Documentation," Dassault Systemes Simulia Corporation.

Varma, A.H., Malushte, S.R., Sener, K.C. and Lai, Z. (2014), "Steel-Plate Composite (SC) Walls for Safety Related Nuclear Facilities: Design for In-Plane Forces and Out-of-Plane Moments," *Nuclear Engineering and Design*, Vol. 269, pp. 240–249.

Wittmann, F., Rokugo, K., Brühwiler, E., Mihashi, H. and Simonin, P. (1988), "Fracture Energy and Strain Softening of Concrete as Determined by Means of Compact Tension Specimens," *Materials and Structures*, Vol. 21, No. 1, pp. 21–32.

Wright, H.D., Oduyemi, T.O.S. and Evans, H.R. (1991a), "The Design of Double Skin Composite Elements," *Journal of Constructional Steel Research*, Vol. 19, No. 2, pp. 111–132.

Wright, H.D., Oduyemi, T.O.S. and Evans, H.R. (1991b), "The Experimental Behaviour of Double Skin Composite Elements," *Journal of Constructional Steel Research*, Vol. 19, No. 2, pp. 97–110.

Xie, M. and Chapman, J. (2006), "Developments in Sandwich Construction," *Journal of Constructional Steel Research*, Vol. 62, No. 11, pp. 1,123–1,133.

Zhang, K., Varma, A.H., Malushte, S.R. and Gallocher, S. (2014), "Effect of Shear Connectors on Local Buckling and Composite Action in Steel Concrete Composite Walls," *Nuclear Engineering and Design*, Vol. 269, pp. 231–239.

Guide for Authors

Scope   *Engineering Journal* is dedicated to the improvement and advancement of steel construction. Its pages are open to all who wish to report on new developments or techniques in steel design, research, the design and/or construction of new projects, steel fabrication methods, or new products of significance to the uses of steel in construction. Only original papers should be submitted.

General   Papers intended for publication should be submitted by email Margaret Matthew, Editor, at matthew@aisc.org.

The articles published in the *Engineering Journal* undergo peer review before publication for (1) originality of contribution; (2) technical value to the steel construction community; (3) proper credit to others working in the same area; (4) prior publication of the material; and (5) justification of the conclusion based on the report.

All papers within the scope outlined above will be reviewed by engineers selected from among AISC, industry, design firms, and universities. The standard review process includes outside review by an average of three reviewers, who are experts in their respective technical area, and volunteers in the program. Papers not accepted will not be returned to the author. Published papers become the property of the American Institute of Steel Construction and are protected by appropriate copyrights. No proofs will be sent to authors. Each author receives three copies of the issue in which his contribution appears.

Manuscripts   Manuscripts must be provided in Microsoft Word format. Include a PDF with your submittal so we may verify fonts, equations and figures. View our complete author guidelines at **www.aisc.org/ej**.